Doctoral Dissertation

Development of antisense oligonucleotides for suppressing breast cancer cell proliferation and the system for evaluating drug response of cardiomyocytes

（乳がん細胞の増殖抑制を目指したアンチセンスと、心筋細胞に対する薬剤応答評価システムの開発）

Sho Okumura

Laboratory of Biomolecular Adaptation Science
Graduate School of Life Science, Hokkaido University
Sapporo, Hokkaido, Japan

September 2021

CONTENTS

List of abbreviations

2'F	2'-fluoro
2'MOE	2'-*O*-methoxyethyl
2'OMe	2'-*O*-methyl
3'-UTR	3'-untranslated region
AFM	atomic force microscopy
Ago	Argonaute
ALCAM	activated leukocyte cell adhesion molecule
AMO	anti-microRNA oligonucleotide
aoNao	*N*,*N*'-(naphthalene-1,5-diyl)*bis*[2-(aminooxy)acetamide]
AP site	apurinic/apyrimidinic site
ATP	adenosine triphosphate
BC	breast cancer
BIM	Bcl-2-like protein 11
CADM1	cell adhesion molecule 1
CDK	cyclin dependent kinase
CL-AMO	cross-linked duplexes modified AMO
CLD	cross-linked duplexes
CPEB4	cytoplasmic polyadenylation element-binding protein 4
CTSK	cathepsin K
DGCR8	DiGeorge syndrome critical region 8
DIG	digoxigenin
DMSO	dimethyl sulfoxide
ER	estrogen receptor
FSH	follicle-stimulating hormone
GnRH	gonadotropin-releasing hormon
HER2	human epithelial growth factor receptor type 2
HMGA1	high mobility group A1
HR	hormone receptor
IP	immunoprecipitation
Jab1	Jun activation domain-binding protein 1
LAMA4	laminin subunit alpha 4
LH	luteinizing hormone
LNA	locked nucleic acids
LZTFL1	leucine zipper transcription factor-like 1
MeRNA	2'-*O*-methyl RNA
miR-X	microRNA-X, X=148a, 148b, 155, 21, 214, 24, 421, 433, and 99a
miRISC	miRNA-induced silencing complex
miRNA	microRNA
MMP13	matrix metallopeptidase 13

MP	micropipette
mRNA	messenger RNA
mTOR	mechanistic target of rapamycin
NFATc1	nuclear factor of activated T-cells, cytoplasmic 1
PACE	phosphonoacetate
PBS(-)	phosphate buffered saline
PCR	polymerase chain reaction
PDCD4	programed cell death protein 4
PI3K	phosphatidylinositol 3-kinase
PMO	phosphorodiamidate morpholino oligomers
PNA	peptide nucleic acid
PR	progesterone receptor
Pre-miRNA	precursor microRNA
Pri-miRNA	primary microRNA
PS	phosphorothioate
PTEN	phosphatase and tensin homolog deleted from chromosome 10
qPCR	quantitative polymerase chain reaction
RanGTP	guanosine triphosphate-bound form of ras-related nuclear protein
RANK	receptor activator of nuclear factor-kappaB
RANKL	receptor activator of nuclear factor-kappaB ligand
RISC	RNA-induced silencing complex
RNase	ribonuclease
ROCK1	Rho-associated, coiled-coil containing protein kinase 1
RP-HPLC	high-performance liquid chromatography
SD	standard deviation
SECM	scanning electrochemical microscopy
SLC7A11	solute carrier family 7 member 11
SLC7A5	solute carrier family 7 member 5
TPM1	tropomyosin 1
TRX	thioredoxin
TuD	tough decoy
TXNIP	thioredoxin-interacting protein
UDG	uracil DNA glycosylase
UNA	unlocked nucleic acid
USP32	ubiquitin specific peptidase 32
USP4	ubiquitin specific Peptidase 4
VEGF	vascular endothelial growth factor
WNT-1	wingless-type MMTV integration site family, member 1

Chapter 1: Introduction

Cancer was the leading cause of death in Japan, followed by cardiovascular disease in 2019[1] (Fig. 1.1A). The mortality rate of these two major causes of death continue to increase while that of cerebrovascular disease is declining[1] (Fig.1.1B). Therefore, elucidation of the causes of cancers and cardiovascular diseases with the aim of developing treatments are important research topics. In cell experiments, it is important to decide not only which target genes to study, but also which reagents, materials, and analysis methods should be used. In this doctoral research, I challenged to develop advanced tools for analyzing cancer cells and cardiomyocytes and applied the technologies to investigation of cell proliferation or cell motion.

In **Chapter 2**, among various cancers, I selected breast cancer (BC) as my research target. I focused on the function of microRNAs (miRNAs) in BC cell proliferation and investigated the inhibition effect of miRNAs. First, I verified whether miRNA inhibitor, anti-miRNA oligonucleotides (AMOs) could inhibit endogenous miRNA functions and suppress the proliferation of BC cells targeting oncogenic miRNA, microRNA-21 that is overexpressed in various cancer cells. Next, I tried to knockdown a low-expressing miRNA and studied its effect on the proliferation of BC cells.

In **Chapter 3**, I focused on cardiomyocytes because the conventional methods for evaluating the function of cardiomyocytes were insufficient in analyzing beating motion. Therefore, I developed a scanning electrochemical microscopy (SECM)-based system for evaluating beating of cardiomyocyte. I constructed the system that could analyze beating changes in response to drug stimulations with maintaining the culture environment of cardiomyocytes.

Finally, in **Chapter 4**, the conclusion and contributions of this research are summarized.

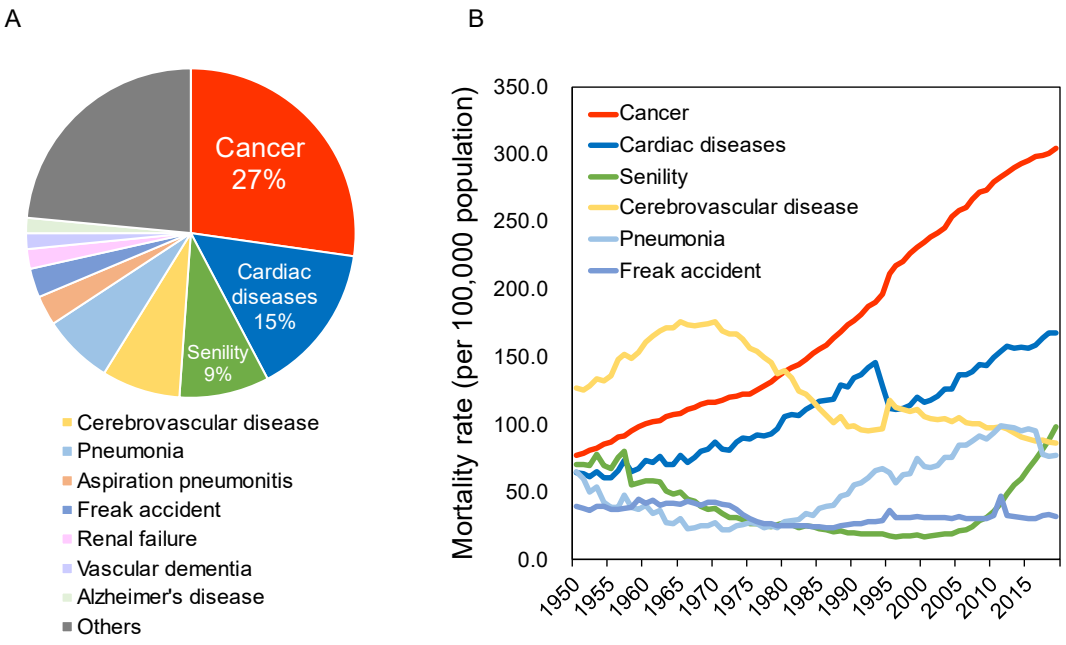

Figure 1.1
Statistical data on causes of death in Japan. (**A**)Top 10 causes of death in Japan, 2019. (**B**) Annual transition of mortality rate (per 100,000 population) from 1950 to 2019. Data was obtained from Ministry of Health, Labour and Welfare, Japan.

Chapter 2: Development of antisense oligonucleotides for suppressing breast cancer cell proliferation

2.1 Abstract

Anti-microRNA oligonucleotides (AMOs) are one of the most potent agents in oligonucleotide therapy. Although single stranded AMOs have been widely used, the inhibition activity of an AMO can be increased by flanking an antisense sequence with interstrand cross-linked duplexes (CLDs). An extrastable CLD improves nuclease resistance of the antisense region and stabilizes hybridization with a target microRNA (miRNA). Previously, AMO modified with CLDs (CL-AMOs) could knockdown miRNA efficiently in using the dual-luciferase assay. In this study, I prepared CL-AMO targeting microRNA-21 (miR-21) that is overexpressed in various cancers, and examined the effects of CL-AMOs on breast cancer (BC) cell proliferation. The CL-AMO targeting miR-21 suppressed BC cell proliferation for a long duration compared to other types of AMOs. In addition, it expectedly up-regulated the miR-21-controlled expression of tumor suppressor tensin homolog deleted from chromosome 10 (*PTEN*) gene. On the other hand, in BC, microRNA-148a (miR-148a) is expressed at low levels, and little attention has been paid to sequestering of miR-148a. I also investigated the effect of knockdown of miR-148a on BC cell proliferation. Although other type of AMOs did not induce any cellular responses, CL-AMO could significantly inhibit BC cell proliferation by binding with miR-148a. Importantly, the CL-AMO-mediated downregulation of miR-148a showed a greater and longer-lasting inhibition of BC cell proliferation than targeting miR-21. I identified thioredoxin-interacting protein (*TXNIP*), a tumor suppressor gene, to be under the control of miR-148a, and confirmed an increase in *TXNIP* mRNA expression by CL-AMO. Therefore, I revealed that low-expressed miRNAs such as miR-148a could be a promising target for cancer treatment, and CL-AMO with high affinity to a target miRNA could be a more effective tool in sequestering these miRNAs.

2.2 Background

2.2.1 Breast cancer and miRNA functions

Breast cancer overview

Breast cancer (BC) is a cancer that occurs from breast tissue and sometimes metastasize to different organs, such as bone, lungs, brain, and liver. In men, the most frequently diagnosed cancer is different according to each country or region. On the other hand, in women, BC is the most commonly diagnosed cancer across countries[2,3] (Fig. 2.1). In the era from the 1980s to the 1990s, BC incident rates increased in westernized countries but in early 2000s, incidence has decreased or remained almost unchanged in many of these countries. In contrast, BC incidence rates have been increasing rapidly in Latin America, Africa, and Asia[4]. In Japan, BC remains relatively rarer than westernized countries, however, the incident and mortality rates have been increasing rapidly[5–7] (Fig. 2.2). The

incident rate of BC was third highest among various cancers in 1975, but it was the highest in 1990s and continues to today in Japan[8,9]. This trend reflects not only increases in BC screening and awareness, but also shift to western pattern diet, delayed childbearing, and shorter duration of breastfeeding in accordance with women's social progress[6,10]. Thus, this trend is predicted to continue in the future.

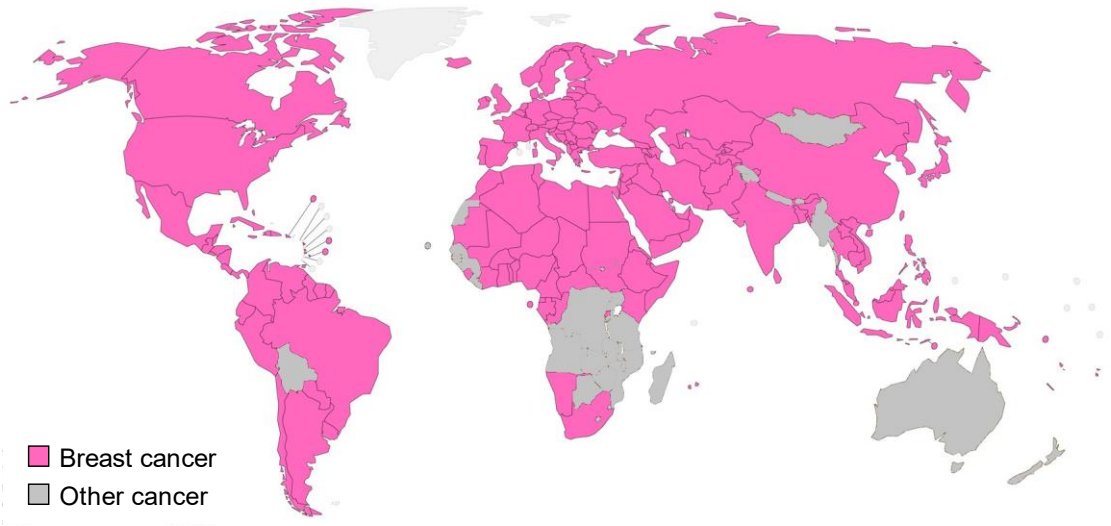

Figure 2.1
The highest incidence rates of cancers per countries in 2020 (females, all ages). Data was obtained from International Agency for Research on Cancer (http://gco.iarc.fr/today) World Health Organization and partially modified. Breast cancer is shown in pink while other cancers are shown in gray.

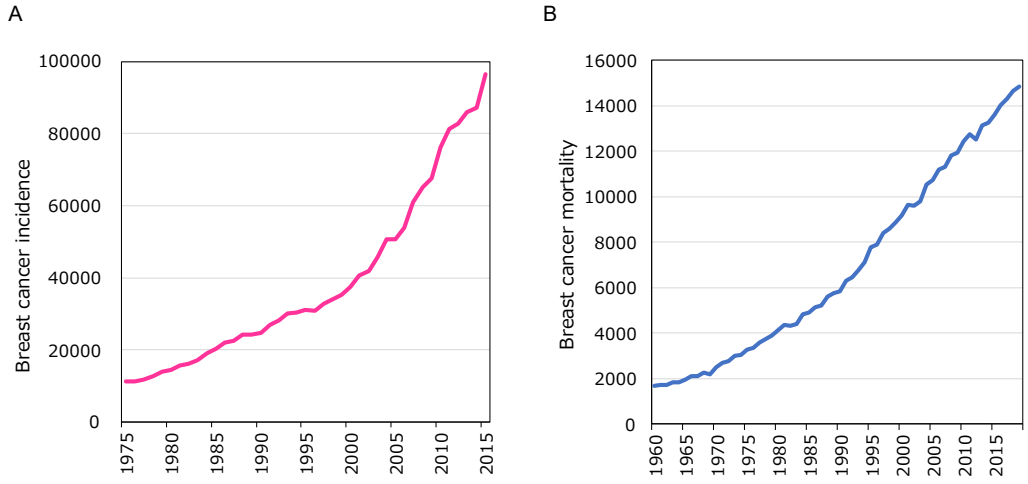

Figure 2.2
Incidence (**A**) and mortality (**B**) number of breast cancers in Japan. Data was obtained from Cancer Statistics. Cancer Information Service, National Cancer Center, Japan (Monitoring of Cancer Incidence in Japan (MCIJ)) (**A**) and Cancer Statistics. Cancer Information Service, National Cancer Center, Japan (Vital Statistics of Japan, Ministry of Health, Labour and Welfare) (**B**).

Classification of breast cancer

Clinically, BCs are classified into different subtypes according to their gene expression profiles[11,12] (Table. 2.1). Luminal A breast cancer is hormone-receptor (HR) positive (estrogen-receptor (ER) and/or progesterone-receptor (PR) positive), human epithelial growth factor receptor type 2 (HER2) negative and has low level of Ki-67 protein that is a cellular marker for proliferation. It accounts for ~40% of all BCs and tends to grow slowly and have the best prognosis among all subtypes. Luminal B BC is HR positive, either HER2 positive or negative and high level of Ki-67 protein. It accounts for ~20% of all BCs and generally grow faster than luminal A and prognosis is slightly worse than luminal A. HER2-enriched BC is HR negative and HER2 positive. It accounts for 15-20% of all BCs and generally grow faster than luminal types that results in a worse prognosis. Triple-negative or basal-like BC is HR negative and HER2 negative. It accounts for 10-15% of all BCs and is considered the most aggressive and have the poorest prognosis than other types of BCs[13,14].

Table 2.1
Summary of the breast cancer molecular subtypes. ER; estrogen receptor, PR; progesterone receptor

Subtype	ER		PR	HER2	Ki-67
Luminal A	+	and/or	+	-	<14%
Luminal B	+	and/or	+	-	≥14%
Luminal B	+	and/or	+	+	any
HER2	-		-	+	any
Triple-negative	-		-	-	any

Treatment strategy of breast cancer

The receptor expression status determines treatment strategy of BC. Because luminal types that express HR require hormone to grow, endocrine therapies that block the effect of hormone are effective for treatment[15,16] (Fig. 2.3). For example, tamoxifen is an antagonist of ER and blocks activation of ER by estrogen[17]. Aromatase inhibitors such as exemestane, anastrozole and letrozole prevent biosynthesis of estrogen resulting in depletion of estrogen[18]. Furthermore, gonadotropin-releasing hormone (GnRH) agonist such as goserelin and leuprolide inhibit release of follicle-stimulating hormone (FSH) from anterior pituitary subsequent to release of estrogen and progesterone from ovary[18].

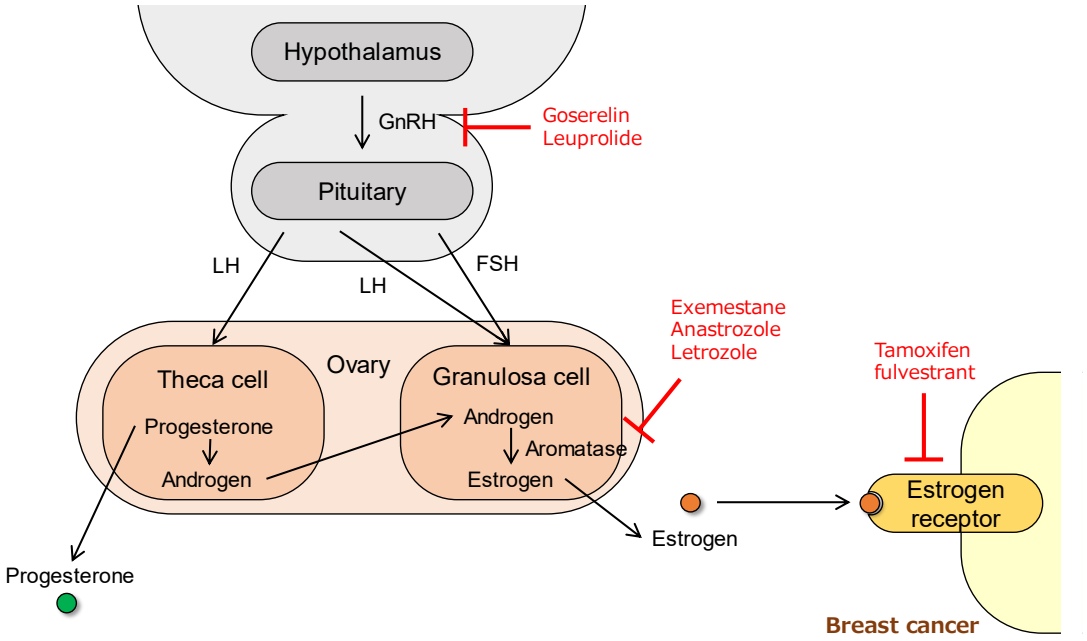

Figure 2.3
Estrogen biogenesis in hypothalamic-pituitary-ovarian axis. Hypothalamic gonadotropin-releasing hormone (GnRH) is released from the hypothalamus and stimulates anterior pituitary gland to release luteinizing hormone (LH) and follicle-stimulating hormone (FSH). LH acts on the theca cells in the ovarian stroma to increase the production of androgens. FSH matures the granulosa cells, and the androgen produced in theca cells is converted to estrogen by aromatase in the granulosa cells. Inhibitors for GnRH, aromatase, and estrogen receptor are shown in red.

Targeted therapy in breast cancer

Targeted therapies target and inhibit specific gene and/or protein which contribute BC growth (Fig. 2.4). HER2 is a tyrosine kinase and associates with BC proliferation, migration, inversion, metastasis, and angiogenesis, so it is established a target protein for BC treatment[19]. The monoclonal antibody trastuzumab (Herceptin) targets HER2 and is the first antibody drug approved by (FDA) for the treatment of HER2 positive BCs[20,21]. Lapatinib (Tykerb) and neratinib (Nerlynx) are not antibody but chemical compound that work as kinase inhibitor inhibit HER2 function[22]. The conjugated antibody trastuzumab emtansine (T-DM1; Kadcyla) and trastuzumab-deruxtecan (Enhertu) are also used for HER2 positive BC[23,24]. These drugs have dual mechanism of function; selective delivery of anti-cancer drug (emtansine or deruxtecan) to the HER2 positive BC cell and inhibition of HER2-mediated signal transduction.

Other proteins such as cyclin dependent kinase 4/6 (CDK4/6), mechanistic target of rapamycin (mTOR) and phosphatidylinositol 3-kinase (PI3K) that have important function for cell growth are also target of HER2 negative BC treatment[25]. Because breast and other cancers need oxygen and nutrients to grow, they induce the growth of new blood vessels into the tumor (angiogenesis). Bevacizumab (Avastin) is a targeted therapy that block the angiogenesis by inhibiting vascular endothelial growth factor (VEGF)[25]. Denosumab is a monoclonal antibody targeted for the receptor activator of nuclear factor-kappaB ligand (RANKL) and used for treatment of osteoporosis. In bone metastasis, BC cells directly secrete RANKL or stimulate RANKL-producing osteoblast to activate osteoclast[26]. Thus, denosumab is effective for treatment of bone metastasis of BC.

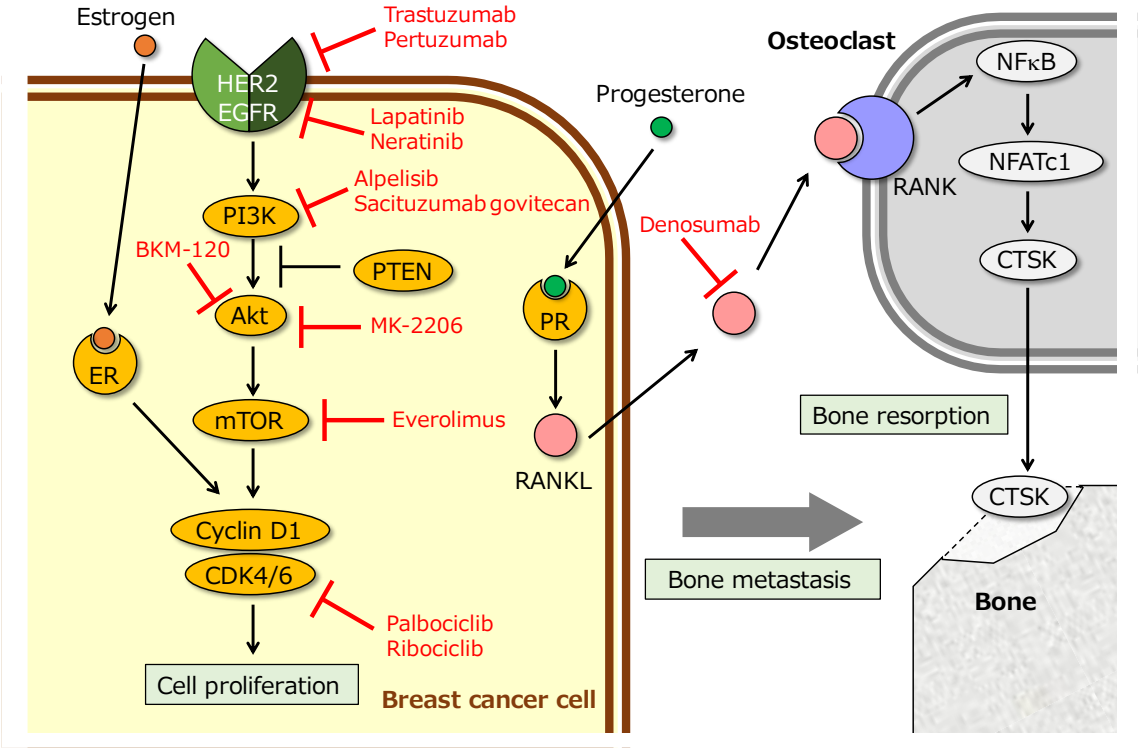

Figure 2.4
Signaling pathway of breast cancer proliferation and bone metastasis. HER2 is a member of epidermal growth factor receptor (EGFR) family located on the cell membrane and forms heterodimer with another EGFR member. HER2 has kinase activity and activate the phosphatidylinositol 3-kinase (PI3K)/protein kinase B (Akt) pathway that result in cell growth and inhibition of apoptosis. Estrogen binds to estrogen receptor (ER) that activate transcription of target genes and contributes to subsequent cell proliferation. Progesterone receptor (PR) is stimulated by progesterone and induces receptor activator of nuclear factor kappa-B ligand (*RANKL*) expression. Secreted RANKL binds to its receptor RANK on the osteoclast precursor cells and induces osteoclast differentiation. Disrupted bone by osteoclast release these growth factors that accelerate breast cancer grow and metastasis. The molecular-targeted drugs for each factor are indicated in red. NFATc1; nuclear factor of activated T-cells, cytoplasmic 1, CTSK; cathepsin K

Tumor heterogeneity and treatment-resistance in breast cancer

In addition to the targeted therapeutic methods, general chemotherapy and radiation therapy are used alone or with other therapies[15]. However, despite of these various therapeutic methods, recurrence represents the most common cause of death from BC[27]. Most BC recurrences are caused by the acquisition of drug resistance in cancer cells, one of which is due to BC heterogeneity[28]. Cancer had been thought as a homogeneous population of cells, however in recent years it has become clear that various subclones with different genetic backgrounds are mixed in it[29,30]. Different genetic backgrounds lead to different susceptibility to drugs and contribute to the acquisition of drug resistance in cancer cells. Drug resistance to BC has also been reported in some targeted therapies[21,31]. Therefore, development of new strategy of BC therapy is necessary.

Function of miRNAs

MicroRNAs (miRNAs) are endogenous small noncoding RNAs comprising 18–23 nucleotides that are universally expressed in many organisms, from animals to plants and posttranscriptionally regulates the expression of various genes[32] (Fig. 2.5A). Biogenesis of miRNA begin with transcription of miRNA precursor (primary microRNA; pri-miRNA) from genome by RNA polymerase II/III[33]. Pri-miRNA is long and has stem-loop structure that contains mature miRNA sequences. Following transcription, Drosha, a ribonuclease (RNase) III enzyme, crops stem-loop region and produces hairpin-shaped RNA (pre-miRNA) in nucleus. Drosha forms a part of protein complex called Microprocessor with DGCR8 that is the double-strand RNA binding protein. The pre-miRNA is then exported into cytosol by exportin 5 that forms the transport complex with GTP-binding protein RanGTP. In the cytosol, pre-miRNA is cleaved by Dicer, an RNase III nuclease, releasing a small RNA duplex. Following Dicer processing, the RNA duplex is loaded onto Argonaute (Ago) protein that is an essential component in the RNA-induced silencing complex (RISC). The pre-RISC containing double-stranded RNA quickly unwind the duplex and remove unnecessary strand (passenger strand). The remained strand (guide strand or mature miRNA) that has partially complementary sequence to its target messenger RNA (mRNA) forms the miRNA-RISC (miRISC) where the miRNA interacts with the target mRNA[34].

miRNAs regulate target mRNA expression through base pairing with complementary sequences at the 3'-untranslated region (3'-UTR) of target mRNAs[35]. For recognition of targets, nucleotides 2-7 of the miRNA that is called the seed region must be perfectly complementary to the target [35,36] (Fig. 2.5B). Conversely, miRNA can bind to the target even though it contains mismatches in non-seed region. Thereby, one miRNA can bind to many mRNAs and various miRNAs can bind to one mRNA[37] (Fig. 2.6). The miRNA binding to the target mRNA leads gene silencing by inhibition of translation and stimulation of mRNA decay[38] (Fig. 2.5A). On the contrary, miRNAs also contribute to translational activation[39]. Through these regulation of target genes, miRNAs contribute diverse cellular function

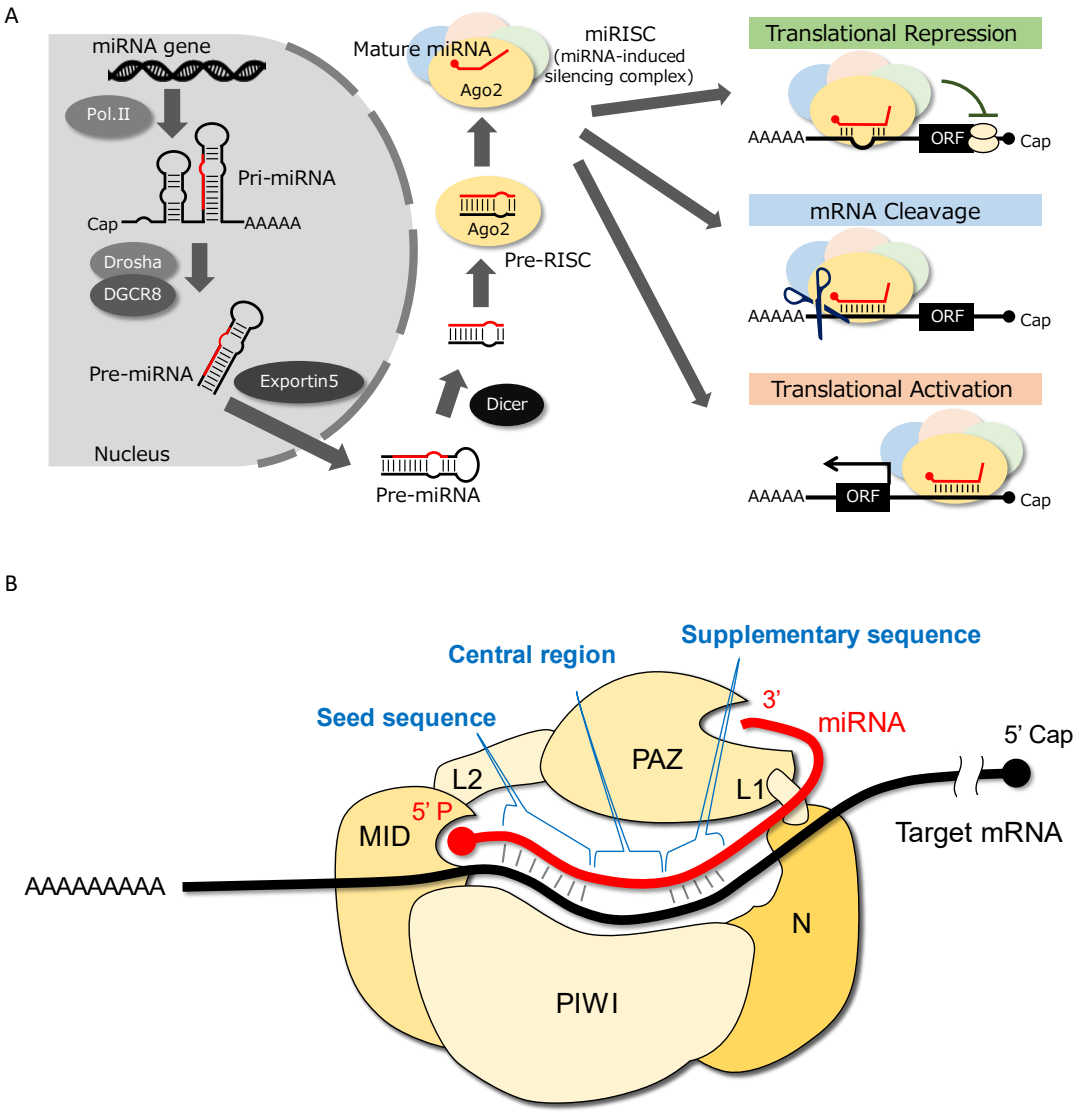

Figure 2.5

MicroRNA biogenesis and interaction to mRNA. (**A**) A primary miRNA (pri-miRNA) is transcripted by polymerase II. Pri-miRNA is cleaved by Drosha resulting in pre-miRNA. Pre-miRNA is then exported to cytoplasm by Exportin 5 complex and cleaved by Dicer to form duplex miRNA. The duplex miRNA is loaded into Argonaute-2 (Ago2) protein and processed to a mature single-stranded miRNA forming miRNA-induced silencing complex (miRISC). The RISC complex is guided by miRNA and binds to target mRNAs, causing translation repression, mRNA cleavage, or translational activation. (**B**) Ago2 protein consists with 4 domains (N, PAZ, MID, and PIWI) and 2 linkers (L1 and L2). The 5′-phosphate of miRNA is anchored in the pocket between MID and PIWI domains. The 3′ end of miRNA bind to PAZ domain. The seed sequence that consists of nucleotides 2-7 at the 5′ region in miRNA has a primary role in target recognition. The supplementary sequence that situated at position 13-16 also implicate in miRNA targeting.

such as cell proliferation, intracellular signaling, cellular metabolism and immunity[40–46]. Therefore, dysregulation of miRNA expression causes various diseases and many kinds of miRNAs are associated with development and progression of cancer, cardiovascular disease, inflammatory disease, neurodevelopmental disease, and autoimmune disease[47–49]. In cancer, various miRNAs have been reported to promote cell proliferation, suppressing apoptosis, or conversely suppressing cell proliferation[50,51]. Therefore, investigating the relationship between these diseases and miRNAs not only elucidates the function of miRNAs, but also contributes to the development of new therapeutic methods.

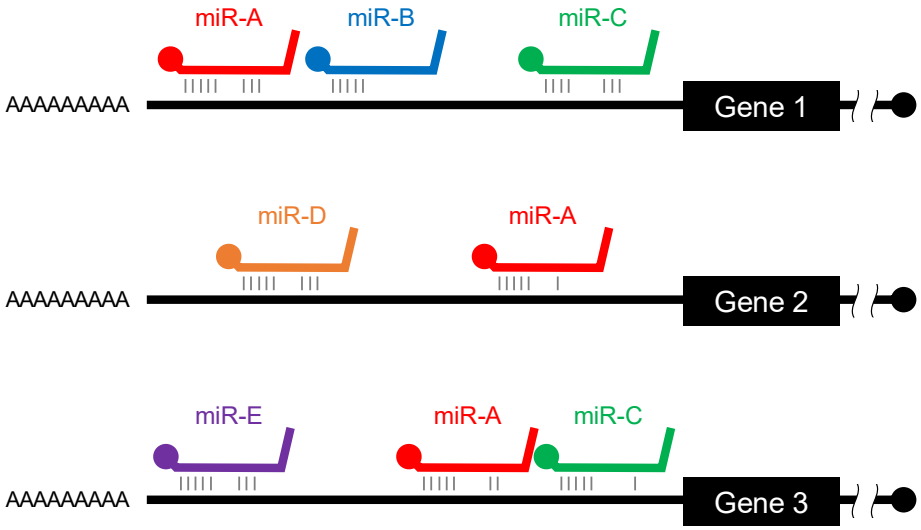

Figure 2.6
Relationship of various miRNA and target genes. One miRNA (miR-A) can target many mRNAs (Gene 1-3). On the contrary, one mRNA (Gene 1) is targeted by many miRNAs (miR-A, miR-B, and miR-C).

miRNAs in breast cancer

Up-regulation or down-regulation of various miRNAs are reported in BCs[52,53]. Up-regulated miRNA is called oncomiR and usually inhibit expression of tumor-suppressive genes. miR-21 (hsa-miR-21-5p) is the most typical oncomiR and associate with tumorigenesis targeting phosphatase and tensin homolog deleted from chromosome 10 (*PTEN*), leucine zipper transcription factor-like 1 (*LZTFL1*) and programed cell death protein 4 (*PDCD4*) in BC[54–57] (Fig. 2.7). miR-214 and miR-421 also targets *PTEN* and *PDCD4*, respectively[58–60]. miR-155 (hsa-miR-155-3p) is up-regulated in BC and promote cell proliferation by inhibiting cell adhesion molecule 1 (*CADM1*), a tumor suppressor gene[61]. Furthermore, miR-24 is also reported as an oncomiR in BC that down-regulates *p27* gene[62] (Fig. 2.7). On the other hand, down-regulated miRNA is called anti-oncomiR and generally oncogenes are its target. Let-7 families are one of the earliest discovered miRNAs. They have tumor-suppressive function by down-regulating high mobility group A1 (*HMGA1*), ubiquitin specific peptidase 32

(*USP32*) and Jun activation domain-binding protein 1 (*Jab1*) in BC[63–65]. miR-145 also impairs BC cell proliferation targeting ERα[66]. Therefore, various miRNAs and its target genes forms a complex network in BC progression (Fig. 2.7). Targeting miRNAs would be superior to traditional protein-targeted therapies because it can collectively correct many pathogenic factors caused by miRNA alterations.

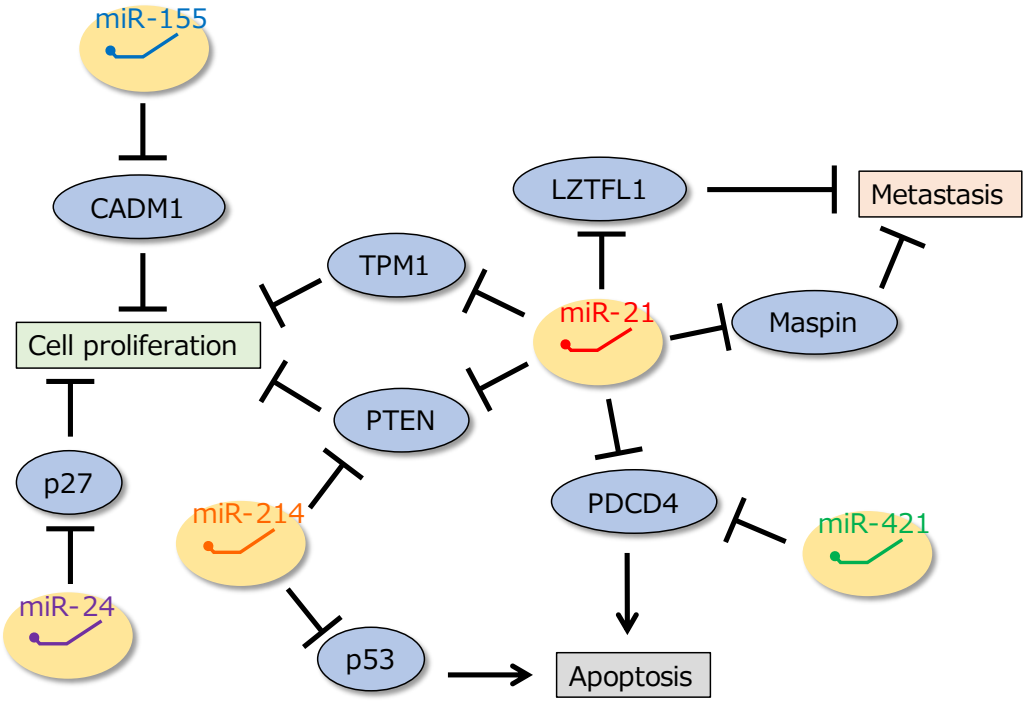

Figure 2.7
Regulation network of various miRNA and target genes. Arrows mean activation while T-bars represent inhibition. The ellipses indicate the target genes, and the squares represent the resulting cellular responses.

2.2.2 anti-miRNA oligonucleotides

Function of AMOs

Anti-microRNA oligonucleotides (AMOs) are synthetic oligonucleotides that contain complementary sequences to their target miRNAs that can inhibit miRNA function (Fig. 2.8). The miRNAs captured by the AMO can then remain sequestered or degraded. Some AMOs are undergoing clinical trials as drug candidates[67]. Miravirsen, an anti-miR-122 oligonucleotide, has undergone phase-2 clinical trial for the treatment of hepatitis C[68]. RG-12 is anti-miR-21 oligonucleotide and in phase-2 clinical trial for treatment of Alport syndrome[69]. AMOs directly bind to the mature miRNA in miRISC but the binding affinity between miRNA and AMO is relatively week because miRNAs are short and

have low Tm value. Furthermore, expression level of miRNA is lower than other RNAs and miRNAs have very similar sequence to each other. In addition, RNases exist abundantly in serum and cells. Therefore, effective AMOs should have high affinity and high specificity to the target miRNA, and high stability in the cells.

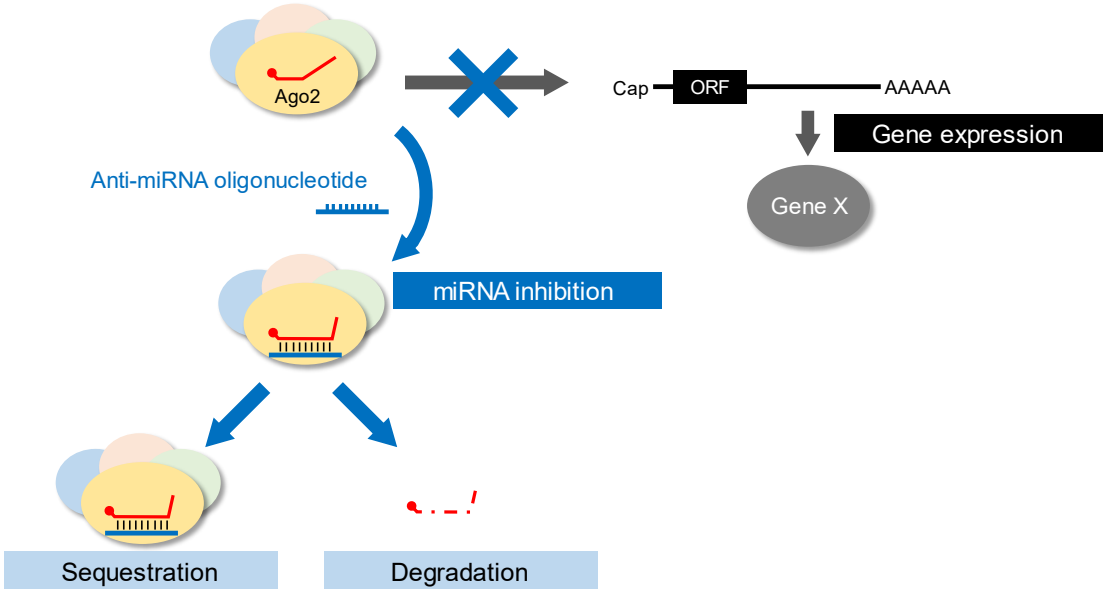

Figure 2.8
miRNA inhibition by anti-miRNA oligonucleotide (AMO). AMO binds to miRNA in miRISC and inhibits the interaction between miRNA and mRNA. miRNA is then degraded or undegraded sequestering by the AMO.

Chemical modifications of AMOs

Various chemical modifications enhance AMO performance (Fig. 2.9). Chemical modifications are mainly introduced in the 2' carbon of the ribose and/or in the phosphate backbone of the oligonucleotide structure. In the case of the ribose modification, 2' hydroxyl is replaced with methoxy group (2'OMe), fluorine (2'F) or *O*-methoxyethyl group (2'MOE), and they are reported to increase binding affinity of AMOs[70,71]. The locked nucleic acids (LNA) that has an extra bridge connecting 2' carbon and 4' carbon is also often used for AMOs to improve the stabilization[72]. Unlocked nucleic acid (UNA) is another analogue of RNA that has the cleaved 2' carbon-3' carbon bond and has high flexibility[73]. UNA insertion into oligonucleotides decrease duplex stability and can increase discrimination of mismatches improving hybridization specificity. Chemical modifications are also introduced into the phosphate backbone. Phosphorothioate (PS) modification is widely used to enhance antisense oligonucleotide performance[70,71]. In PS modification, one of the non-bridging oxygen of phosphate is substituted by a sulfur in the phosphodiester (PO) bonds that are natural inter-nucleotide linkage. Phosphonoacetate (PACE) modification has an acetate group substitution of non-

bridging oxygen in the inter-nucleotide phosphate linkage[74]. Phosphorodiamidate morpholino oligomers (PMOs) are uncharged nucleic acid analogue that are composed with the morpholine rings linked through phosphorodiamidate groups. Due to their neutral charge, PMO oligonucleotides have high RNase-resistance and improved binding affinity for target miRNAs[75]. Peptide nucleic acid (PNA) is also an uncharged synthetic nucleic acid analogue that has the backbone composed of *N*-(2-aminoethyl)-glycine linked by peptide bonds[76]. Because PNA contains no charged phosphate group, it has high binding affinity to the target DNA or RNA.

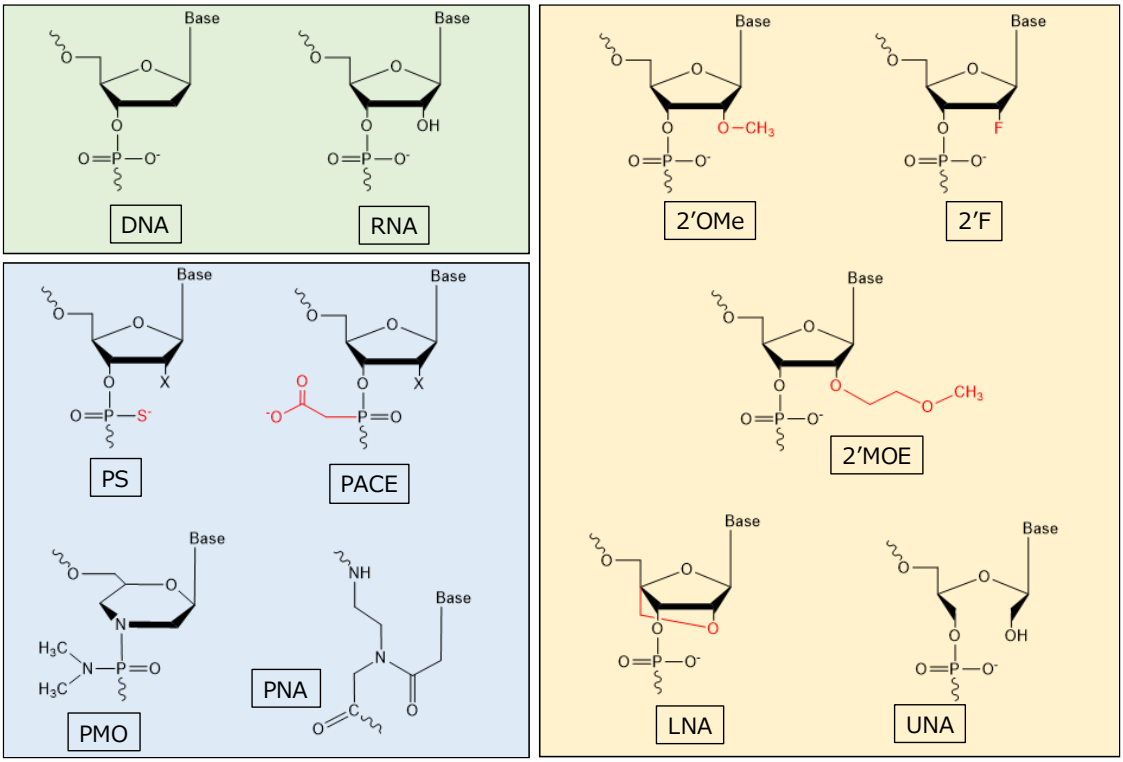

Figure 2.9
Various chemical modification of nucleic acid in the AMO. Unmodified nucleotide: deoxyribonucleic acid (DNA), and ribonucleic acid (RNA). Sugar modifications: 2′-*O*-methyl (2′OMe), 2′-fluoro-RNA (2′F), Locked Nucleic Acid (LNA), Unlocked Nucleic Acid (UNA), and 2′-*O*-methoxyethyl (2′MOE). Backbone modifications: phosphorothioate (PS), phosphonoacetate (PACE), Phosphorodiamidate Morpholino Oligomers (PMO), and Peptide Nucleic Acid (PNA).

AMOs of different secondary structures

The unique secondary structures also improve the performance of AMOs (Fig. 2.10). A single-stranded AMO with flanked sequences at both 5' and 3' termini has better miRNA inhibitory activity than an AMO with only complementary sequence to the target miRNA. Moreover, an AMO with double-stranded structures at both 5' and 3' termini has even higher binding affinity and stability through the base stacking interactions[77]. However, since double strands are easily dissociated, AMOs

with various structures have been developed to stabilize the double strand structure. Hairpin AMOs have stem-loop structures at both 5' and 3' termini of the complementary sequence to the target miRNA and exhibits high miRNA inhibitory activity[77]. The tough decoy (TuD) RNAs are constructed with 2'OMe RNAs and have a complex secondary structure composed of two miRNA-binding sites flanked by two stem structures[78]. The TuD modified AMOs indicated higher inhibition activity than single-stranded AMOs and have been already used for the basic research.

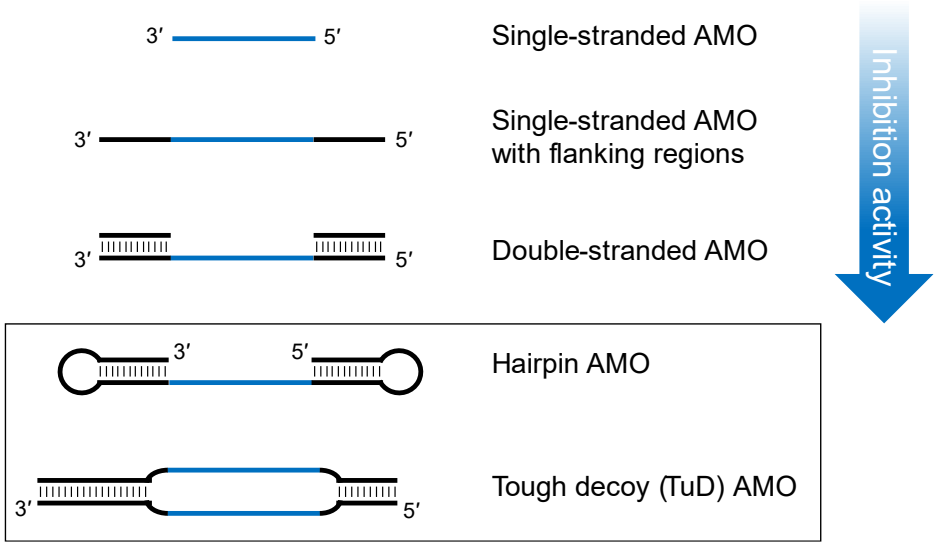

Figure 2.10
Unique secondary structures and its inhibitory activity of AMOs. Single-stranded AMOs increase inhibitory activity by having flanking regions, and flanking double-stranded regions further increase its activity. A hairpin AMO has stem loop structures at 5' and 3' termini of antisense sequence, and Tough decoy AMO has a stabilized stem structure with two miRNA binding domains.

Interstrand cross-linked AMO

The stability of duplexes at the termini of AMOs largely depends on the surrounding environment. In addition, a long sequence is required for double-stranded stabilization, which increases the molecular weight of AMO. For stabilization of short double-stranded sequences, Ichikawa *et al.* previously reported a sequence-specific cross-link reaction that connects a pair of apurinic/apyrimidinic sites (AP sites) on complementary oligodeoxynucleotides using a short bifunctional cross-linker containing bis-aminooxy groups[79]. The cross-linked structure provides rigid duplex as DNA scaffolds for immobilized enzyme reaction[80]. To improve the activity of AMO by stabilizing the terminal double-strand structure, Mie *et al.* have developed an advanced AMOs that have interstrand cross-linked duplexes (CLDs) at both ends of their antisense sequence[81] (Fig. 2.11). CLD-modified AMOs (CL-AMO) exhibit significantly higher inhibition activity in luciferase reporter assay compared to other commercially available AMOs with various modifications. Furthermore, CL-

AMOs also do not induce an immune response in HeLa cells. Therefore, CL-AMO would be a promising therapeutic drug candidate for miRNA-related cancers and a powerful tool for miRNA research, but the inhibition of endogenous miRNAs and their cellular effects have not been verified yet.

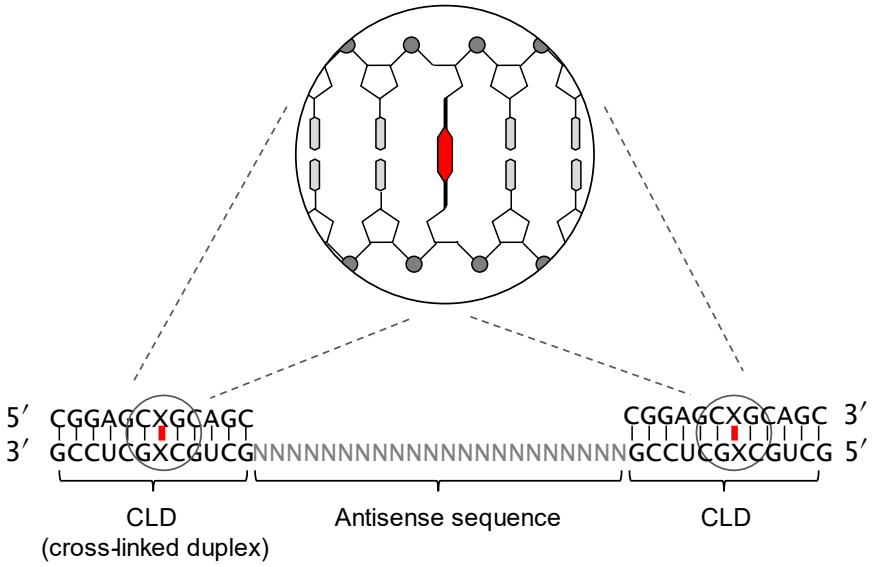

Figure 2.11
Schematic image of CL-AMO. Antisense sequence to target miRNA is indicated in gray. Vertical cold lines and Xs indicate the cross-linker and cross-linked sites.

miR-21 and miR-148a

MiR-21 highly expressed in many tumors[82,83]. It is also upregulated in BC tissues and cell lines and inhibition of miR-21 decreases BC cell proliferation[56]. Therefore, regulation of miR-21 expression is one of the most promising strategies for cancer therapy and miR-21 will be the best first validation target of CL-AMOs.

Compared with overexpressing miRNA such as miR-21, inhibition of low-expressing miRNA by AMO may be difficult. Because AMO rarely encounters and binds to the low-expressing miRNA in the cell, once bounded AMO should hardly dissociate from the target for sufficient inhibition. In addition, because it will be slight expression change after AMO treatment to the low-expression miRNA, AMO is required to inhibit the target miRNA completely. Furthermore, especially in cancer treatment study, AMO is usually used for down-regulation of over-expressing miRNA, so down-regulation of low-expressing miRNA tend to be disregarded. However, it was suggested that miRNA activity is not only determined by its expression level[84] and there is a possibility that miRNA has important role in cellular process even if its expression level is low.

A member of the miR-148/152 family, microRNA-148a (miR-148a; hsa-miR-148a-3p), is a known tumor suppressor (anti-oncomiR) (Fig. 2.12A and B). Overexpression of miR-148a inhibits cancer cell

proliferation and induces apoptosis in colorectal[85], gastric[86], and hepatocellular cancers[87]. Similarly, in BC, miR-148a inhibits cell proliferation and migration[88]. The role of miR-148a has been evaluated exclusively by overexpression experiments in BC cells. The effect of the knockdown of miR-148a has not been fully clarified most likely because miR-148a is expressed at a low level in the cell[89–92].

Another member of the miR-148/152 family, microRNA-148b (miR-148b; hsa-miR-148b-3p), has the same seed sequence as that of miR-148a, except for two nucleotides at the 9‑10 positions from each 5'-terminus[93] (Fig. 2.12A and C). It is also an anti-oncomiR in various cancers, including BC[94–97]. However, contradictory results have shown that miR-148b is upregulated in BC patients and is a potential BC biomarker[98,99].

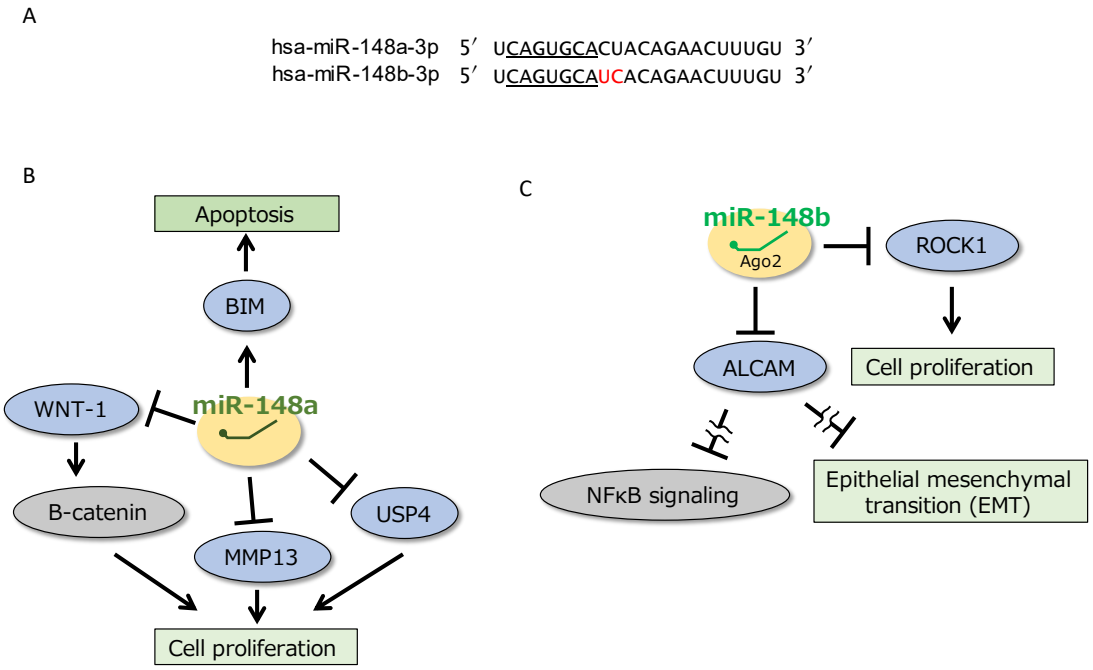

Figure 2.12
miR-148a and miR-148b in breast cancer. (**A**) Sequence of miR-148a and miR-148b. (**B**) miR-148a and (**C**) miR-148b target genes in breast cancer.

In this chapter, I investigated whether the CL-AMOs regulate miRNA function and the BC cell proliferation to determine the potential of CL-AMOs for BC treatment. CL-AMO performance was compared with other types of AMOs (LNA-modified AMO or tough decoy) and reported the potential of CL-AMO for BC treatment. I also use CL-AMOs in evaluation of low-expressing miR-148a. The CL-AMO effect on BC cell proliferation was analyzed using mRNA microarray and online database analyses. These results clarified not only the unknown functions of miR-148a in BC, but also the advantages of CL-AMO in miRNA inhibition.

2.3. Result

2.3.1. Preparation of CL-AMO

All CL-AMOs were synthesized from 2'-*O*-methyl RNA (MeRNA). CL-AMO targeting miR-21 (CL-miR21) was prepared in previous study[81] (Fig. 2.13A). CL-AMO for negative control that has no complementarity to any miRNAs (CL-NC)[100] (Fig. 2.13A) was constructed from cross-linking between 12- and 46-mer-containing scramble sequences. Briefly, 6 nmol of 12-mer MeRNA and 2 nmol of 46-mer MeRNA were annealed in 197.5 μl uracil DNA glycosylase (UDG) reaction solution. Next, 2.5 μL of 5 units/μl of UDG was added to the solution and incubated for 2.5 h at 37°C. The reaction solution was then cooled at 4°C and mixed with 20 μl of 2 mM *N*,*N*'-(naphthalene-1,5-diyl)*bis*[2-(aminooxy)acetamide]; aoNao) (Fig. 2.13B) as a cross-linker. Cross-linking was performed overnight at 17°C, and the reaction product was purified using reverse-phase high-performance liquid chromatography (RP-HPLC). After desalting using NAP-5 column, CL-NC concentration was adjusted to 20 μM and was used for cell transfection experiments.

2.3.2. Inhibition of breast cancer cell proliferation with CL-miR21

CL-miR21 was transfected at 5 or 10 nM into the human BC cell lines MCF-7 that expresses higher levels of miR-21 compared to normal breast cells[56]. After 3, 6 and 9 days, the number of cells was measured and the inhibitory activity for endogenous miR-21 was compared to Locked nucleic acids (LNA)-modified AMO (LNA-miR21) and tough decoy (TuD-miR21). After 3 days of transfection, both CL-miR21 and TuD-miR21 slightly suppressed cell growth at concentrations of 5 and 10 nM (Fig. 2.14A and C). After 6 and 9 days of transfection, only CL-miR21 could maintain the inhibitory effect (Fig. 2.14A-C). Since the culture medium was changed after 3 days, these results suggested that CL-miR21 can remain stably active in BC cells for 9 days.

2.3.3 Target specificity of CL-miR21

To confirm that cell inhibition was not caused by cytotoxicity of CL-AMO, CL-NC was also used for transfection. Unlike CL-miR21, CL-NC did not inhibit cell proliferation, even at a concentration of 20 nM (Fig. 2.14D). In addition, previously studies have shown that CL-AMOs themselves do not exhibit cytotoxicity[81]. These results indicated that CL-miR21 activity is derived from binding with miR-21.

2.3.4 CL-miR21 effect in another breast cancer cell

I also investigated the inhibitory activity of CL-miR21 in another BC cell line ZR-75-1, which is classified as a luminal subtype of BC, such as MCF-7[101]. ZR-75-1 cell proliferation was significantly

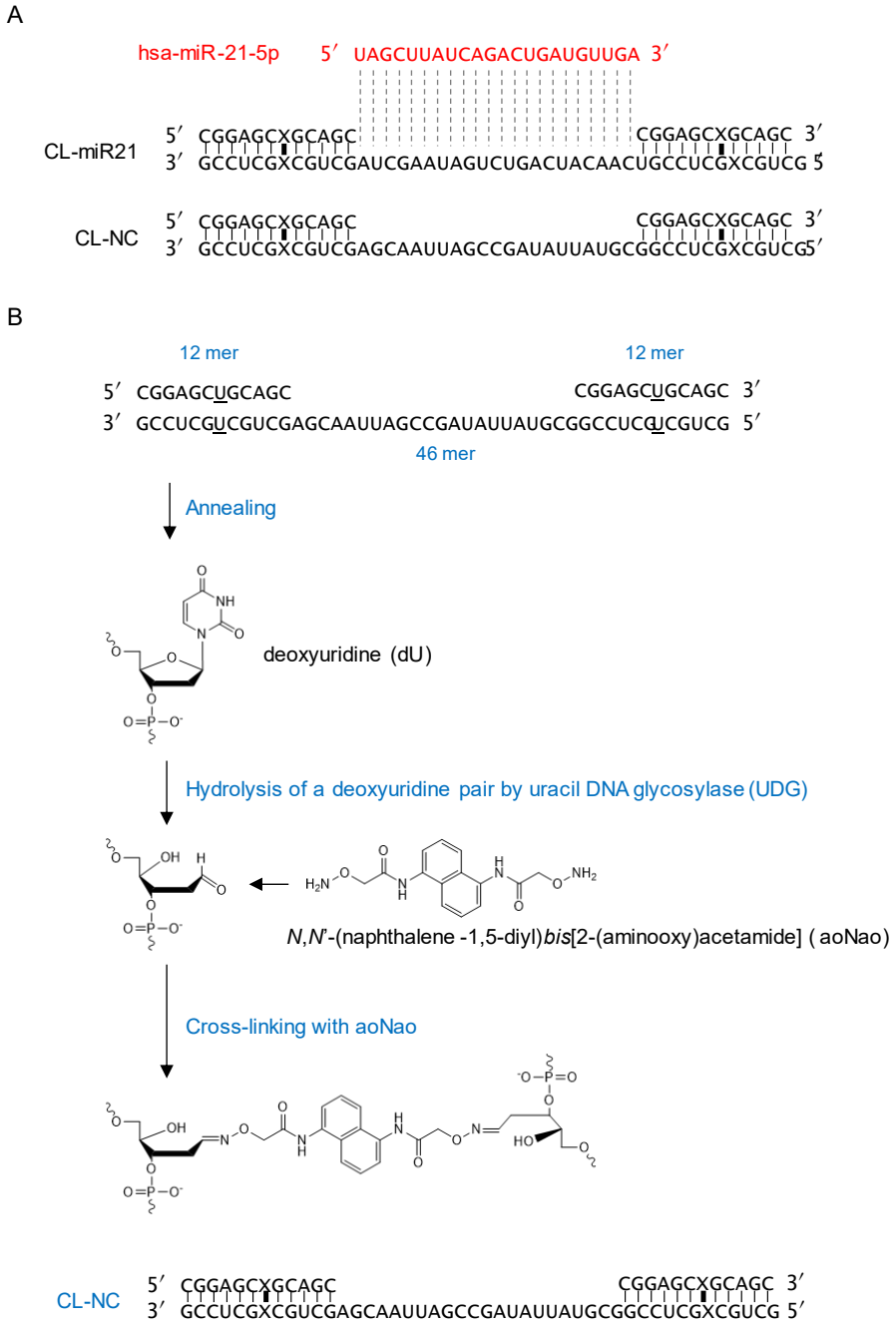

Figure 2.13
Overview of CL-AMO preparation. (**A**) Sequence of miR-21, CL-miR21, and CL-NC. (**B**) Schematic image of CL-AMO preparation. 46-mer containing antisense sequence to the target miRNA and 12-mer oligonucleotide that are synthesized from 2′-*O*-methyl RNA including deoxyuridine in part are annealed. Then, uracil DNA glycosylase eliminates uracil from deoxyuridine and forms apurinic/apyrimidinic sites (AP sites). *N*,*N*'-(naphthalene-1,5-diyl)*bis*[2-(aminooxy)acetamide] (aoNao) connects facing AP sites to form a stable cross-link structure.

low compared to MCF-7[102]. Also, ZR-75-1 showed a lower expression level of endogenous miR-21 compared to MCF-7 (Fig. 2.15A). CL-miR21 significantly inhibited ZR-75-1 cell proliferation compared to other AMOs in a dose-dependent manner (Fig. 2.15B-D), confirming that CL-miR21 can be effective against other cell lines of BC, too.

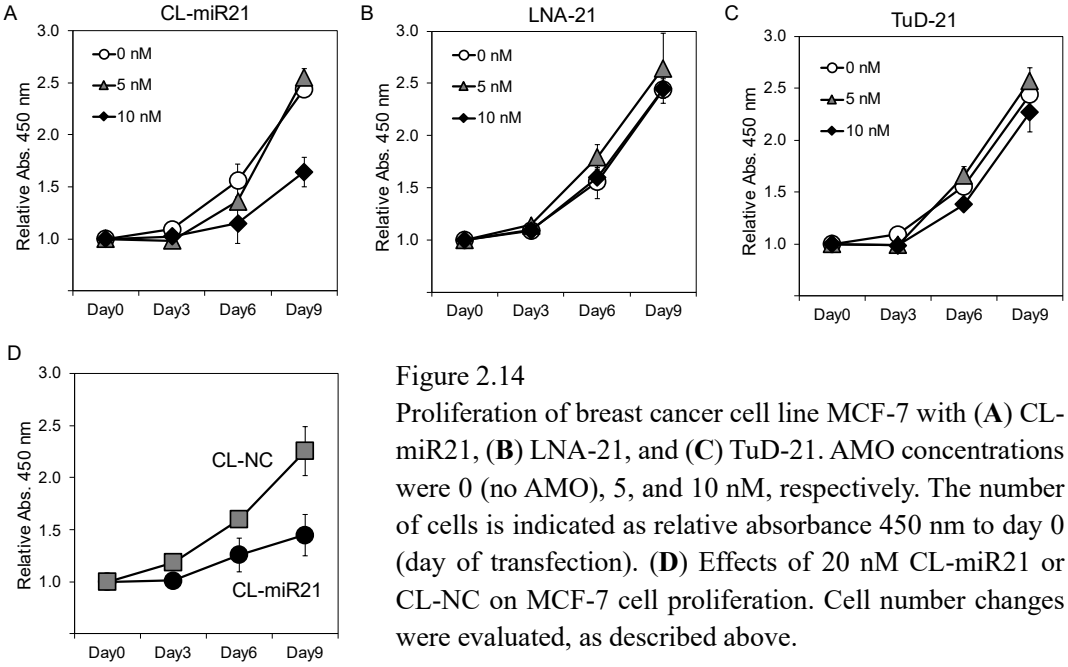

Figure 2.14
Proliferation of breast cancer cell line MCF-7 with (**A**) CL-miR21, (**B**) LNA-21, and (**C**) TuD-21. AMO concentrations were 0 (no AMO), 5, and 10 nM, respectively. The number of cells is indicated as relative absorbance 450 nm to day 0 (day of transfection). (**D**) Effects of 20 nM CL-miR21 or CL-NC on MCF-7 cell proliferation. Cell number changes were evaluated, as described above.

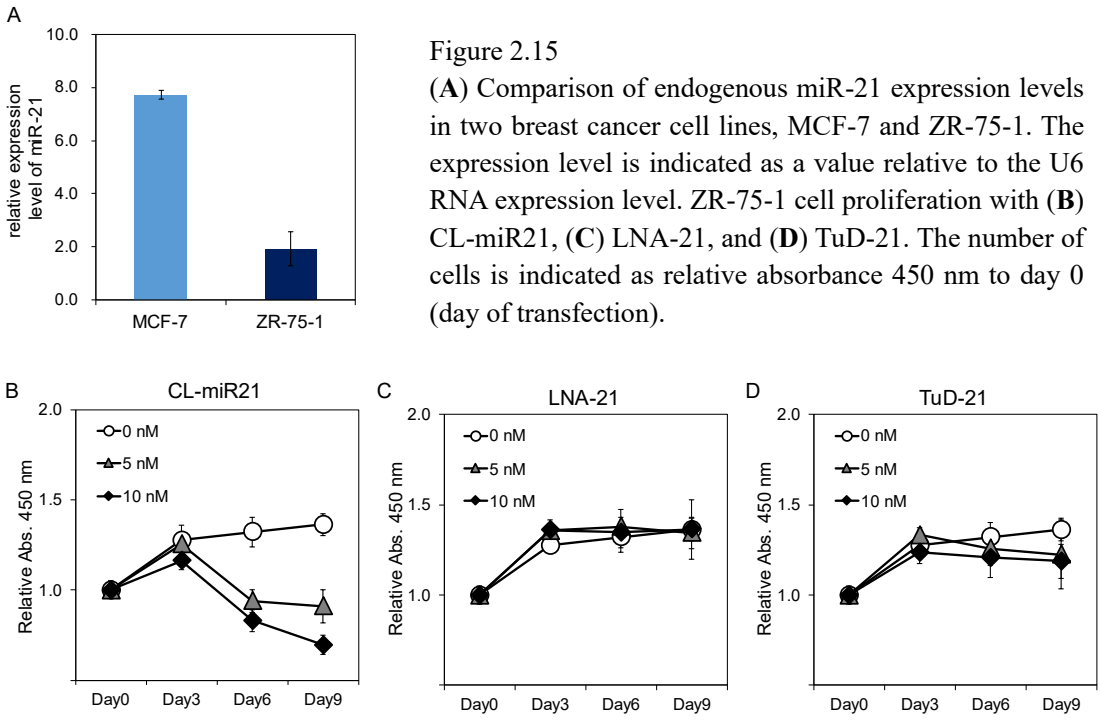

Figure 2.15
(**A**) Comparison of endogenous miR-21 expression levels in two breast cancer cell lines, MCF-7 and ZR-75-1. The expression level is indicated as a value relative to the U6 RNA expression level. ZR-75-1 cell proliferation with (**B**) CL-miR21, (**C**) LNA-21, and (**D**) TuD-21. The number of cells is indicated as relative absorbance 450 nm to day 0 (day of transfection).

2.3.5. *PTEN* mRNA expression after CL-miR21 transfection

PTEN is a tumor suppressor gene[103]. miR-21 suppresses *PTEN* expression and promotes cell proliferation in colorectal[104], kidney[105], prostate[106], and lung cancers[107]. To verify that MCF-7 inhibition by CL-miR21 involves *PTEN* regulation, *PTEN* mRNA expression after transfection was determined with quantitative PCR (qPCR). CL-miR21 increased *PTEN* mRNA expression (Fig. 2.16), while CL-NC did not. Notably, these mRNA samples were harvested at 6 days post-transfection, when no AMOs existed in the culture medium, reconfirming the high stability of CL-miR21. This result indicated that miR-21 binds with CL-miR21, resulting in sequestration from *PTEN* mRNA. Then, up-regulated *PTEN* inhibits the MCF-7 cell cycle. Therefore, CL-AMOs inhibit BC cell proliferation in a molecular target–specific manner and could provide a promising strategy for BC treatment.

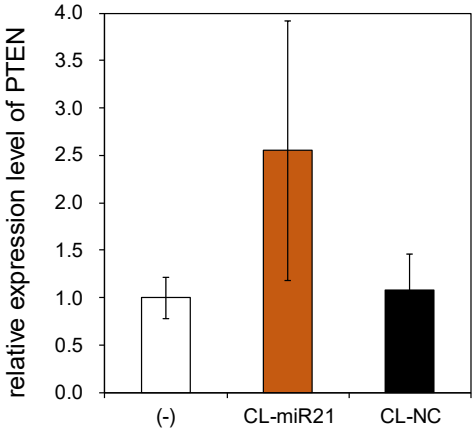

Figure 2.16
Expression level of *PTEN* mRNA in MCF-7 cells. (–) indicates no AMO control. The expression level is indicated as a relative value based on the value of the (–) sample.

2.3.6 Inhibition of low-expressing miR-148a

For further investigation of CL-AMO potential, effect on another miRNA was analyzed. I focused on miR-148a and first measured miR-148a expression in MCF-7 cells. The expression of miR-148a was quite low (<1/1000) (Fig. 2.17) compared with miR-21 suggesting difficulty of knockdown of miR-148a by AMO. I tried to knockdown miR-148a using a single-stranded AMO synthesized from MeRNA (ssAMO-148a) (Fig. 2.18) and commercially available AMOs. MCF-7 cells were transfected

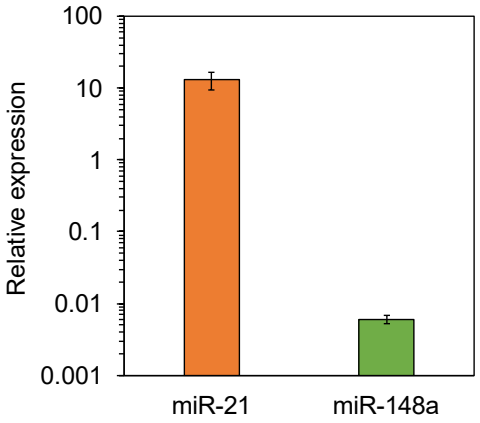

Figure 2.17
qPCR analysis of miR-21 and miR-148a expression in MCF-7 cells. The expression level is indicated as a value relative to the U6 RNA expression. Error bars represent SD. Notice that the vertical axis is logarithmic.

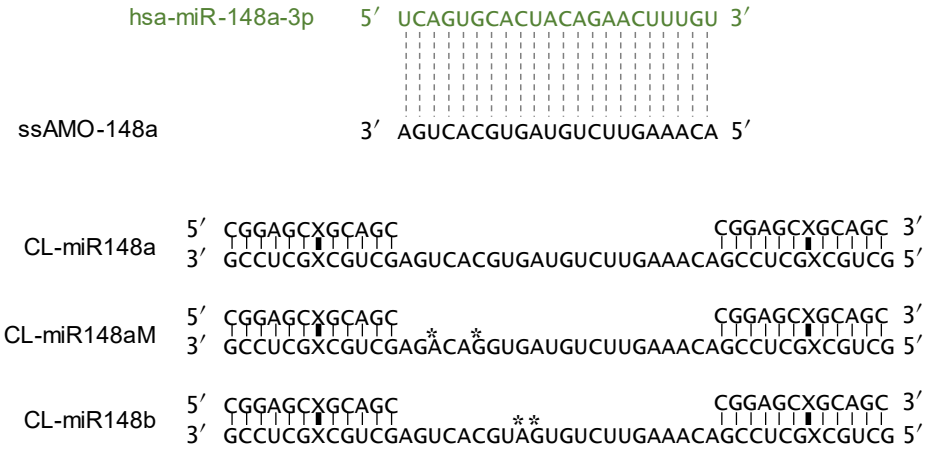

Figure 2.18
Sequences of miR-148a, ssAMO-148a, and CL-AMOs. CL-miR148a holds CLDs at both 5′- and 3′-termini of the antisense sequence complementary to miR-148a. CL-miR148aM is similar to the antisense, except that it contains two mismatched bases identified by asterisks. CL-miR148b is designed to hybridize with miR-148b. The vertical bold lines and Xs indicate cross-linker and cross-linked sites, respectively.

with each AMO independently, and the number of MCF-7 cells was counted after culture. The ssAMO-148a, which only has a complementary sequence for miR-148a, did not affect MCF-7 cell proliferation (Fig. 2.19A and B). The TuD-AMO targeting miR-148a showed a slight inhibitory effect at 20 nM (Fig. 2.19C), but higher concentrations did not provide further inhibition (Fig. 2.19D).

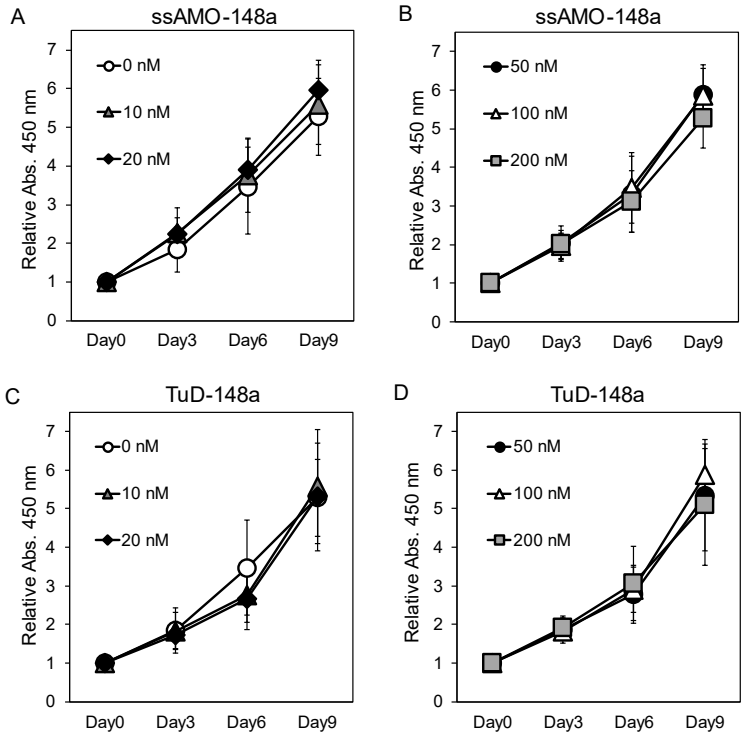

Figure 2.19
Analysis of cell proliferation after transfection with AMOs. Plots of relative numbers of cells versus days after transfection. (**A**, **B**) ssAMO-148a and (**C**, **D**) TuD-148a were used at a concentration of 0 (open circles), 10 (gray solid triangles), 20 (black solid diamonds), 50 (black solid circles), 100 (open triangles), or 200 nM (gray solid squares). Error bars represent SD.

2.3.7 Inhibition of miR-148a by CL-AMO

Next, I used a CL-AMO targeting anti-miR-148a (CL-miR148a) (Fig. 2.18). CL-miR148a was prepared to have cross-linked 12-mer duplexes at both the 5'- and 3'-termini of the 22-mer antisense for miR-148a according to the method of CL-NC (Fig. 2.13B). In addition to CL-miR148a, I constructed a mismatch AMO (CL-miR148aM) (Fig. 2.18), having two mismatched base pairs in the seed region, which is essential for miRNA-target mRNA binding[35,36]. Surprisingly, CL-miR148a showed a dose-dependent activity (Fig. 2.20A) and transfection with 20 nM CL-miR148a completely inhibited MCF-7 cell proliferation after 6 days. Transfection of CL-NC and CL-miR148aM had no significant effect (Fig. 2.20B and C) which confirmed that CL-miR148a antiproliferative action was

mediated by its binding to miR-148a. Moreover, I performed the inhibition of miR-148a in ZR-75-1 BC cell line and confirmed the antiproliferative effect of CL-miR148a in another cell line (Fig. 2.21A and B).

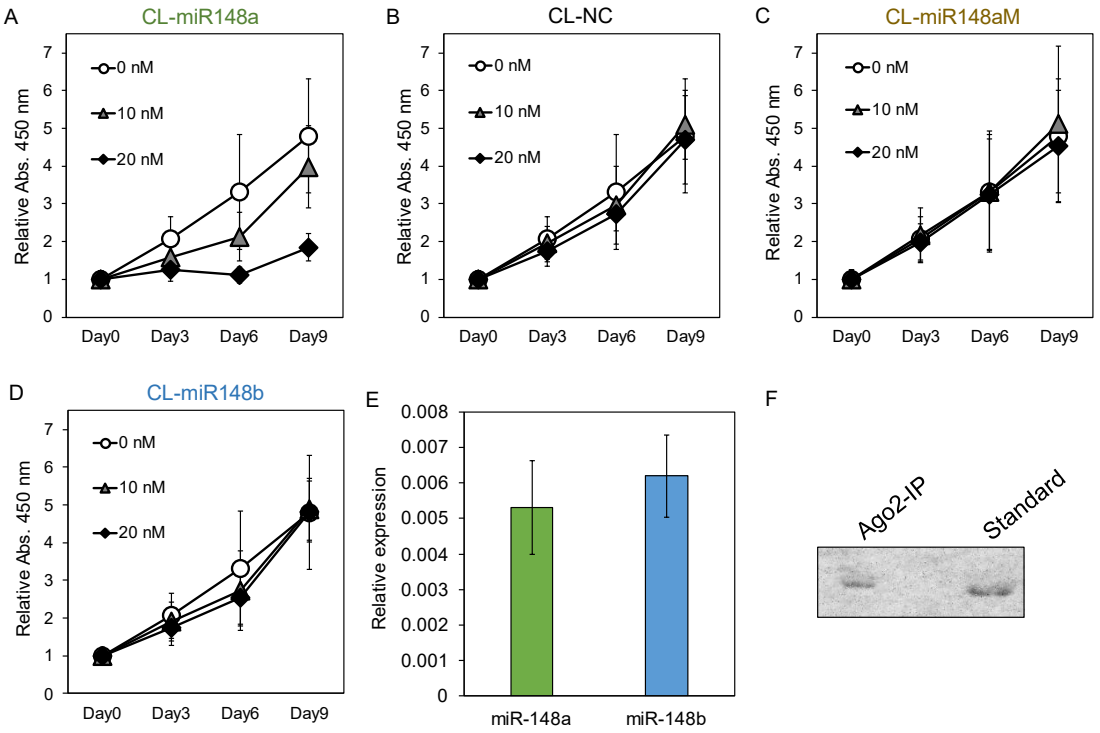

Figure 2.20

Analysis of MCF-7 cell proliferation after transfection with CL-AMOs. Plots of relative numbers of cells versus days after transfection with (**A**) CL-miR148a, (**B**) CL-NC, (**C**) CL-miR148aM, and (**D**) CL-miR148b at a concentration of 0 (open circles), 10 (gray solid triangles), or 20 nM (black solid diamonds). Error bars represent SD. (**E**) Comparison of endogenous miR-148a and miR-148b expression in MCF-7 cells. The expression level is indicated relative to U6 RNA expression. Error bars represent SD. (**F**) Northern blot analysis of CL-miR148a coimmunoprecipitated with Ago2 (Ago2-IP) after transfection. "Standard" indicates CL-miR148a used for transfection.

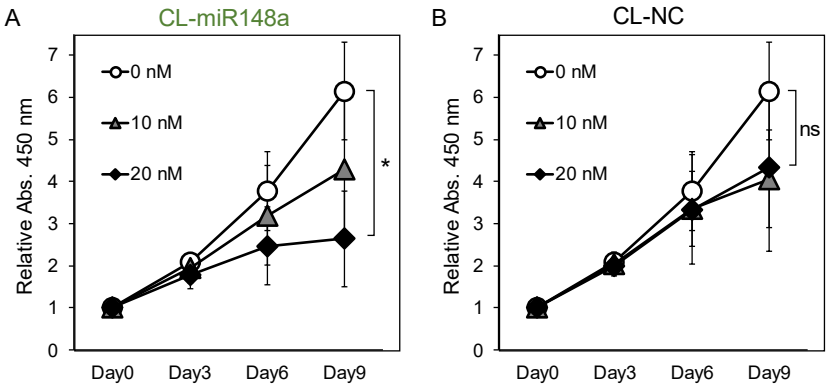

Figure 2.21
Analysis of ZR-75-1 cell proliferation after transfection with AMOs. Plots of relative numbers of cells versus days after transfection with (**A**) CL-miR148a and (**B**) CL-NC at a concentration of 0 (open circles), 10 (gray solid triangles), or 20 nM (black solid diamonds). Error bars represent SD. "ns" indicates insignificant; *$p < 0.05$.

I also investigated the effects of miR-148b in MCF-7 cell. The transfection of CL-AMO-targeting miR-148b (CL-miR148b) (Fig. 2.18) induced a very weak inhibition at 3 and 6 days after transfection, but the effect was lost after 9 days (Fig. 2.20D). The difference between CL-miR148a and CL-miR148b activities did not result from different target amounts as both miRNAs were expressed to similar extent in MCF-7 cells (Fig. 2.20E). It also indicates that the inhibitory effect of CL-miR148a was not mediated by miR-148b downregulation.

I performed immunoprecipitation (IP) using anti-Ago2 antibodies after CL-miR148a transfection to investigate whether CL-miR148a binds to miRISC. CL-miR148a was recovered in the IP samples, confirming that CL-miR148a binds to miRISC (Fig. 2.20F).

2.3.8 Comparison of CL-miR148a and CL-miR21

Both CL-miR21 and CL-miR148a indicated inhibition of MCF-7 cell proliferation, so I compared the inhibition activity of them. Interestingly, the antiproliferative activity of CL-miR148a was greater than the CL-miR21 effect at all concentrations tested (Fig. 2.22). The biggest significant difference was observed for the 20 nM samples. These results suggested that miR-148a is a hopeful therapeutic target surpassing miR-21.

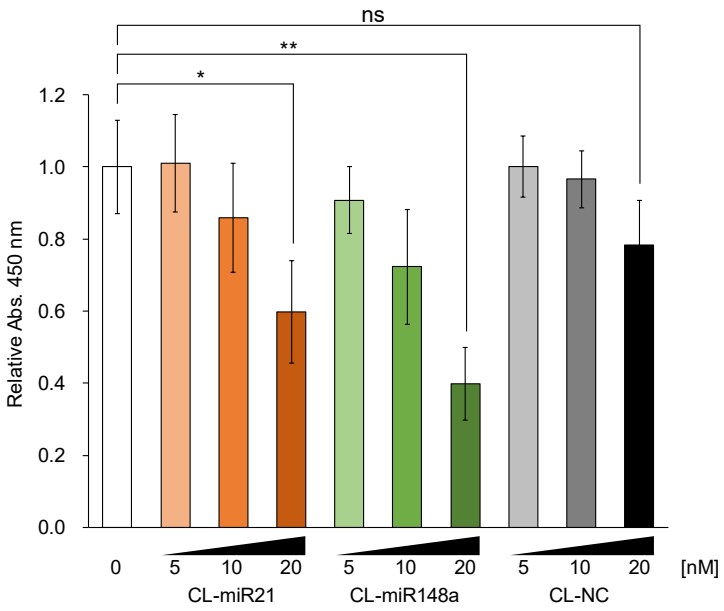

Figure 2.22
Relative number of MCF-7 cells transfected with CL-AMOs (CL-miR21, CL-miR148a, or CL-NC) 6 days after transfection. AMO concentrations varied from 0 to 20 nM, as labeled below the x-axis. Error bars represent SD. "ns" indicates insignificant; *$p < 0.05$; **$p < 0.01$.

2.3.9 miR-148a expression level after CL-AMO transfection

I performed qPCR to measure miRNA expression level after CL-AMO transfection but did not obtain reproducible results (data not shown). This is consistent with previous results reporting that high-affinity AMOs do not mediate the degradation of miRNAs[81,108] and sometimes directly prevent qPCR reaction[109]. Therefore, quantification of miRNA by qPCR would not be suitable for evaluation of AMO activity.

2.3.10 Investigation of target genes regulated by CL-miR148a

In this study, only CL-AMO found oncogenic function of miR-148a in BC. To discuss the difference between CL-AMO and commercially available AMOs, I investigated the molecular mechanisms under CL-AMO treatment. I analyzed the gene expression profile by mRNA microarrays to identify the genes controlled by miR-148a. Genes were considered differentially expressed when more than 1.5-fold changes were measured upon CL-miR148a addition. I found 461 genes that were upregulated (Fig. 2.23A) and could constitute direct targets of miR-148a, and 462 genes were downregulated (Fig. 2.23B). An online database search using TargetScan 7.2 identified 802 genes predicted to contain binding sequences to miR-148a in the 3'-UTR of their mRNAs. Using microarray and online database analysis, I selected five candidates as direct miR-148a target: solute carrier family 7 member 11 (*SLC7A11*), thioredoxin-interacting protein (*TXNIP*), cytoplasmic polyadenylation element-binding

protein 4 (*CPEB4*), solute carrier family 7 member 5 (*SLC7A5*), and laminin subunit alpha 4 (*LAMA4*) (Fig. 2.23C, Fig. 2.24 and Table 2.2).

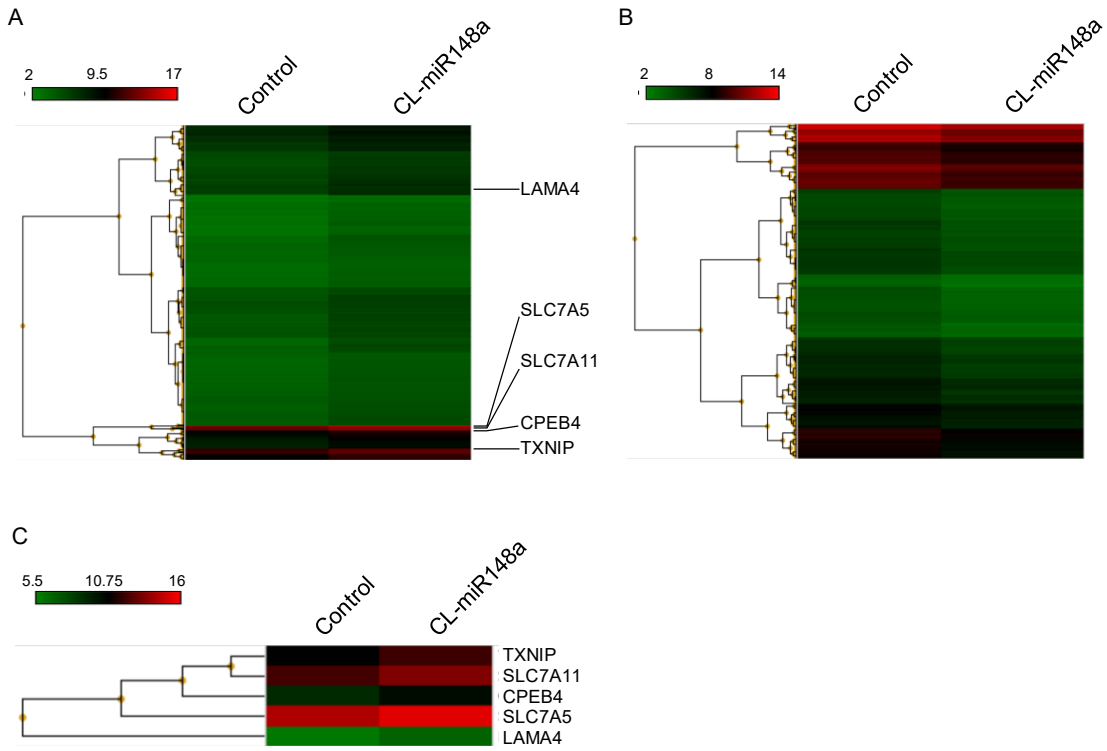

Figure 2.23
Heatmaps of the differential expression of mRNAs in no AMO (control) or CL-miR148a-transfected MCF-7 cells. High expression levels are in red, and low expression levels are in green. Compared with the control, 461 genes were upregulated by CL-miR148a transfection (**A**), whereas 462 genes were downregulated (**B**). After performing an online database analysis, five candidate genes were selected. The five candidate genes (*TXNIP*, *SLC7A11*, *CPEB4*, *SLC7A5*, and *LAMA4*) are marked on the heatmap in (**A**), which is enlarged in (**C**).

Table 2.2
Expression changes of 5 genes detected by the mRNA assay analysis.

Gene_Symbol	mRNA Accession	Expression change	Expression volume
SLC7A11	NM_014331	-1.682842	9.652411
TXNIP	NM_006472	-1.629286	8.898856
CPEB4	NM_001308189	-1.601274	7.841699
SLC7A5	NM_003486	-1.593446	10.882297
LAMA4	NM_001105206	-1.534480	7.329410

TXNIP 3'UTR	Position 702-708	5′ ...AUUUUUGGAGCCUAUUGCACUGU... 3′ miR-148a 3′ UGUUUCAAGACAUCACGUGACU 5′
	Position 1220-1226	5′ ...CUGUCCUGUGUCAGAGCACUGAG... 3′ 3′ UGUUUCAAGACAUCACGUGACU 5′
SLC7A11 3'UTR	Position 6673-6679	5′ ...AUUACAUGGUAGUGAUGCACUGG... 3′ 3′ UGUUUCAAGACAUCACGUGACU 5′
	Position 7467-7473	5′ ... UUCUUAGGGUUCCUA---GCACUGAU... 3′ 3′ UGUUUCAAGACAUCACGUGACU 5′
CPEB4 3'UTR	Position 1214-1220	5′ ...AGUUGCAAAGUGUUU---UGCACUGU... 3′ 3′ UGUUUCAAGACAUCACGUGACU 5′
	Position 2384-2390	5′ ...AAAUUAUGAAUGUCGUGCACUGG... 3′ 3′ UGUUUCAAGACAUCACGUGACU 5′
SLC7A5 3'UTR	Position 446-453	5′ ...UUGCUACCACAGACUUGCACUGA... 3′ 3′ UGUUUCAAGACAUCACGUGACU 5′
LAMA4 3'UTR	Position 41-47	5′ ... ACAAAGUUCUUUAGAGCACUGAA... 3′ 3′ UGUUUCAAGACAUCACGUGACU 5′

Figure 2.24
Targets prediction of miR-148a binding sites in the 3′UTR of the five candidate genes. The miR-148a sequence is indicated in bold characters and vertical lines of each complex show Watson–Crick base pairs. Two binding sites are predicted for *TXNIP*, *SLC7A11*, and *CPEB4* and a single binding site for *SLC7A5* and *LAMA4*.

2.3.11 Quantitative analysis of the target gene after CL-miR148a transfection

To confirm the association of five candidate genes in CL-AMO treatment, qPCR analysis of *SLC7A11*, *TXNIP*, *CPEB4*, *SLC7A5*, and *LAMA4* was performed after CL-miR148a transfection into MCF-7 cells. The mRNA expression levels of *TXNIP*, *CPEB4*, and *SLC7A5* significantly increased, whereas *SLC7A11* and *LAMA4* mRNA were only slightly increased (Fig. 2.25). These results indicate that *TXNIP*, *CPEB4*, and *SLC7A5* were plausible candidate genes involved in the inhibition of MCF-7 cell proliferation. CL-AMOs that have no complementary sequences to miR-148a (CL-miR148aM, CL-miR148b, and CL-NC) did not affect the mRNA expression level of these genes (Fig. 2.25). I considered that *TXNIP* was the most promising miR-148a target gene in MCF-7 cells as it was shown to contribute to a better prognosis of BC[110] and inhibits BC cell proliferation[111]. Recently, direct binding between miR-148a and the 3'-UTR of *TXNIP* was reported in noncancerous cells. Moreover, an anti-miR-148a oligonucleotide was shown to upregulate TXNIP protein in hepatocytes[112] and cardiomyocytes[113]. I also investigated whether ssAMO or TuD-AMO-targeting miR-148a upregulated

TXNIP expression. As shown in (Fig. 2.26), ssAMO had no effect, whereas TuD elicited only a slight effect on *TXNIP* expression. Therefore, *TXNIP* expression might be closely associated with BC cell proliferation regulated by CL-miR148a, as discussed below.

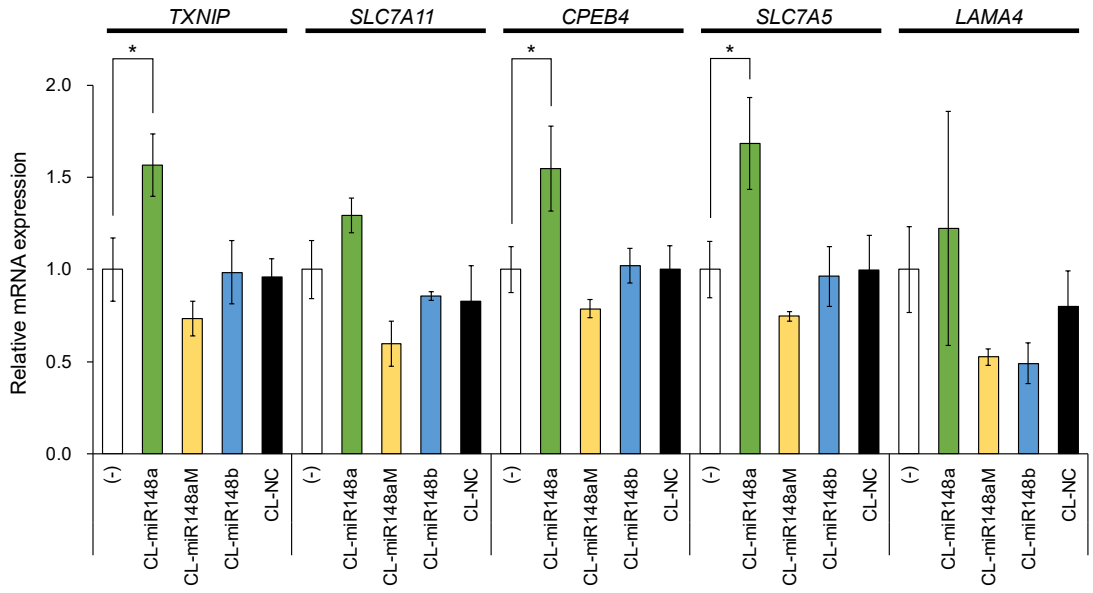

Figure 2.25
Changes in mRNA expression induced by CL-AMO transfection. The expression of the mRNA, relative to the control without AMO, was plotted against CL-AMOs. The name of each gene appears at the top of the graph, and the CL-AMO, including the control, is shown below the horizontal x-axis. Error bars represent SD; *$p < 0.05$.

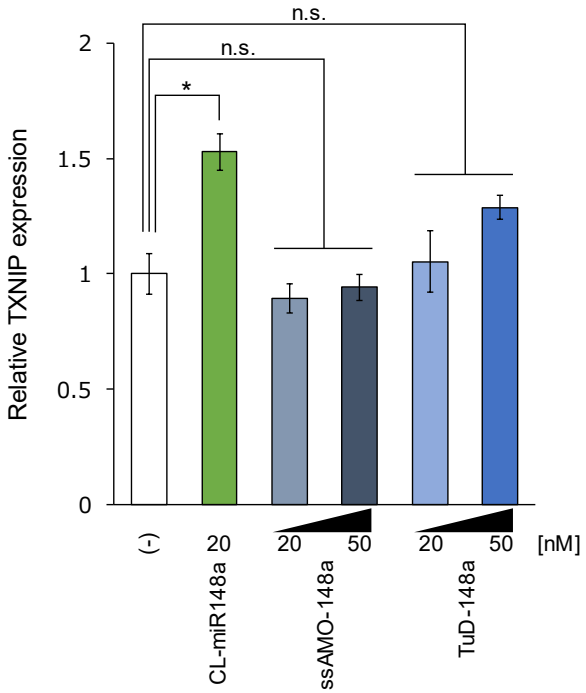

Figure 2.26
Changes in *TXNIP* mRNA expression induced by various AMO transfections. The mRNA expression values relative to the control without AMO were plotted against AMOs. CL-miR148a was transfected at 20 nM, whereas ssAMO-148a and TuD-148a were 20 nM and 50 nM, as shown below the horizontal x-axis. Error bars represent SD. “ns” indicates insignificant; *$p < 0.05$.

2.5 Discussion

Aberrant expression of miRNAs can cause various cancers, which attracted attention on miRNAs as potential therapeutic targets and biomarkers of cancer[114,115]. Inhibition of miR-21, one of the earliest identified oncomiRs[53], represents a potential therapeutic target[83]. Mie *et al.* reported that CL-AMO exhibit significantly higher inhibition activity compared to other AMOs and do not induce an immune response in HeLa cells[81]. Therefore, CL-AMO targeting miR-21 will be promising oligonucleotide therapeutic strategy of cancer, however, cytostatic function of CL-AMO has not been analyzed. In this study, I first indicated CL-miR21 suppress BC cell proliferation with higher efficiency compared to other types of AMOs (Fig. 2.14 and Fig. 2.15). CL-miR21 shows effective suppression at relatively low concentrations, such as 10 nM, while commercially available AMOs are frequently used at concentrations of 50–100 nM for miRNA inhibition[56,116,117]. Importantly, CL-miR21 stably inhibits cancer cell proliferation for a long time, even after it is removed from the culture medium. These results suggest that CL-AMOs might avoid unexpected cytotoxicity or off-target effects that may be caused by high AMO concentration. CL-miR21 functions are target specific, and the expression level of *PTEN* mRNA, which is one of the targets of miR-21, is up-regulated by CL-miR21 (Fig. 2.16). These findings demonstrate that CL-AMOs are significantly effective in regulating miRNAs and could be a promising strategy for BC treatment.

In BC, miR-148a overexpression inhibits BC cell proliferation and migration[88–90,92]. As miR-148a has an antioncogenic function, knockdown experiments of miR-148a in BC were not considered. In this study, I examined the effects of miR-148a knockdown. As the expression of miR-148a is low, I took advantage of CL-AMOs, which have high binding affinity for target miRNAs and a durable action in cells, to sequester miR-148a. CL-miR148a clearly inhibited BC cell proliferation in a dose-dependent manner (Fig. 2.20A and Fig. 2.21A), and the effect lasted for 9 days after transfection. Conversely, ssAMO-148a or TuD AMOs had no significant effect even at a concentration 10-fold higher than that of CL-miR-148a (Fig. 2.19). These differences were caused by difference of AMO performance; the CLD structure is able to stabilize the hybridization of adjacent single-stranded RNA. Mie *et al*. previously reported that CL-AMOs had a much higher melting temperature when bound to target RNAs than standard single-stranded antisense RNAs had[81]. Thus, I speculate that CL-AMOs tightly bind to their targets irreversibly, resulting in the complete sequestration or degradation of the target miRNA (Fig. 2.27, top).

The mismatched CL-AMO (CL-miR148aM) did not inhibit BC cell proliferation (Fig. 2.20C). CL-miR148a was found to be bound to the Ago2–miRNA complex by IP (Fig. 2.20F), which confirmed that CL-miR148a functioned by binding between CL-AMO and miR-148a. MCF-7 cell proliferation was not affected by CL-miR148b, which was specific for miR-148b that has only two base pair differences from miR-148a (Fig. 2.20D). This excluded a possible cross-reaction between CL-miR148a and miR-148b.

Notably, even though miR-148a has a much lower expression level than miR-21 in MCF-7 cells[118] (Fig. 2.17), the downregulation of miR-148a inhibited cell growth more efficiently than the decrease of miR-21 did (Fig. 2.22). This result suggests that miRNAs with low expression levels are also involved in cancer cell proliferation.

To identify the CL-miR148a target genes associated with the inhibition of MCF-7 cell proliferation, I conducted mRNA microarray analysis after CL-miR148a transfection. I considered upregulated genes as direct targets of miR-148a (Fig. 2.23A) and narrowed them down to five genes by referring to an online database for miR-148a target prediction (Fig. 2.23C, Fig. 2.24 and Table 2.2). Importantly, three of the five genes were upregulated upon the addition of CL-miR148a (Fig. 2.25). I specifically focused on *TXNIP*, which was first identified as a 1,25-dihydroxyvitamin D_3-inducible gene[119], because recent studies have reported the direct binding of miR-148a to the 3'-UTR of *TXNIP* in hepatocytes[112] and cardiomyocytes[113]. In contrast to CL-miR148a, ssAMO-148a did not affect *TXNIP*, whereas TuD-148a induced a slight dose-dependent upregulation of *TXNIP*, consistent with its effect on cell proliferation (Fig. 2.26). These results suggest that inhibition of BC cell proliferation is caused by changes in the *TXNIP* expression level.

TXNIP directly binds to the reduced form of thioredoxin (TRX)[120] (Fig. 2.27, middle). TRX is an antioxidant protein that reduces oxidized proteins and protects cells from oxidative stress-induced apoptosis. It was also shown to contribute to cancer progression (TRX system; Fig. 2.27, bottom)[121,122]. *TRX* is overexpressed in BC[123,124], and *TRX*-transfected MCF-7 cells display a higher proliferation rate[125]. Therefore, the TRX system is closely related to MCF-7 cell growth[126]. The binding of TXNIP to TRX decreases the amounts of the TRX reduced form, resulting in the inhibition of BC tumorigenesis[110,111]. CL-miR148a transfection upregulated *TXNIP* mRNA expression (Fig. 2.25) but caused no change in *TRX* expression level (Fig. 2.28). TXNIP inhibits TRX activity by protein–protein interaction[120] but does not regulate *TRX* mRNA expression[127]. Therefore, it is plausible that CL-miR148a caused the inhibition of BC cell proliferation through the TXNIP and TRX system.

This is the first study reporting that miR-148a downregulation inhibits BC cell proliferation. I showed that *TXNIP* gene expression is under the control of miR-148a in MCF-7 cells (Fig. 2.25). CL-miR148a could reduce miR-148a to even a lower concentration in cells, resulting in the inhibition of BC cell proliferation via *TXNIP* upregulation (Fig. 2.27, top). These results indicate that complete inhibition of miRNA unveils unknown cellular responses, which might lead to the discovery of unknown functions of miRNAs.

These findings provided new knowledge regarding miR-148a function in BC, and they may contribute to the development of promising strategies for BC treatment. Additionally, it showed the importance of miRNAs with low expression levels. Finally, AMO-mediated knockdown of miRNAs can provide important insights into the functions of these miRNAs.

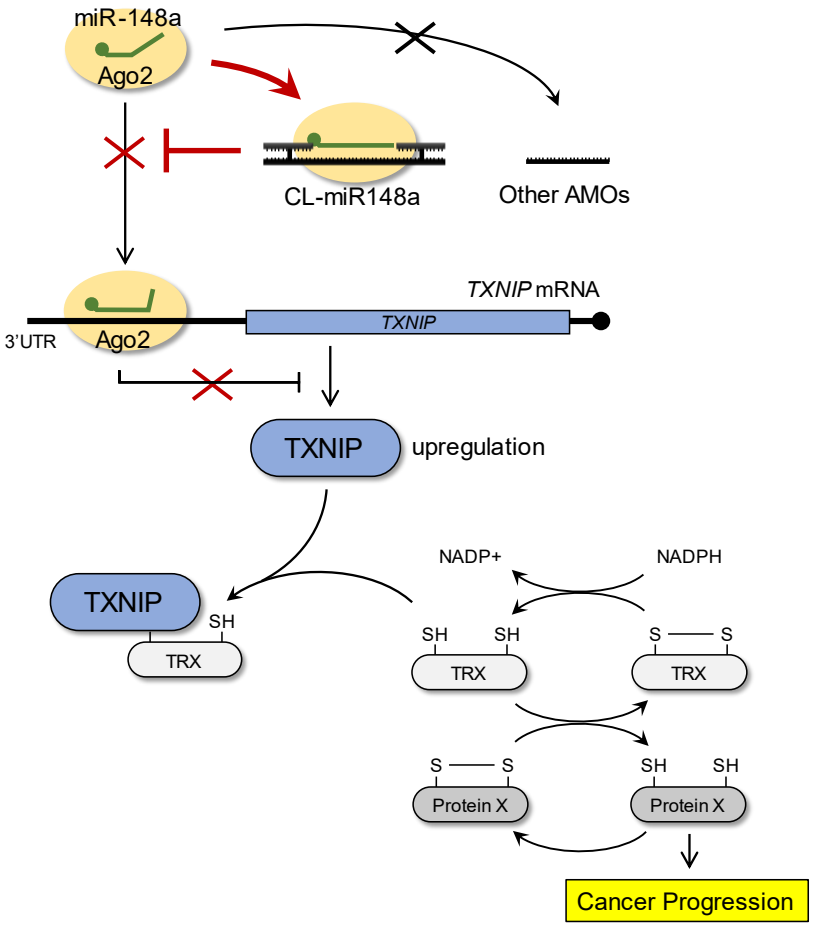

Figure 2.27

Schematic diagram of CL-miR148a-mediated inhibition of BC cell proliferation. The reduced form of TRX (thioredoxin) displays an antioxidant activity by reducing the oxidized protein X. This antioxidant function is associated with cancer progression. TXNIP binds to reduced TRX and prevents protein X reduction, resulting in the inhibition of tumorigenesis in BC. *TXNIP* expression is regulated by miR-148a binding to the 3′-UTR of the mRNA. CL-miR148a antagonizes miR-148a binding to *TXNIP* mRNA, resulting in the upregulation of *TXNIP* expression. By contrast, other AMOs could not stably sequester miR-148a. The red X marks the steps inhibited by the addition of AMO.

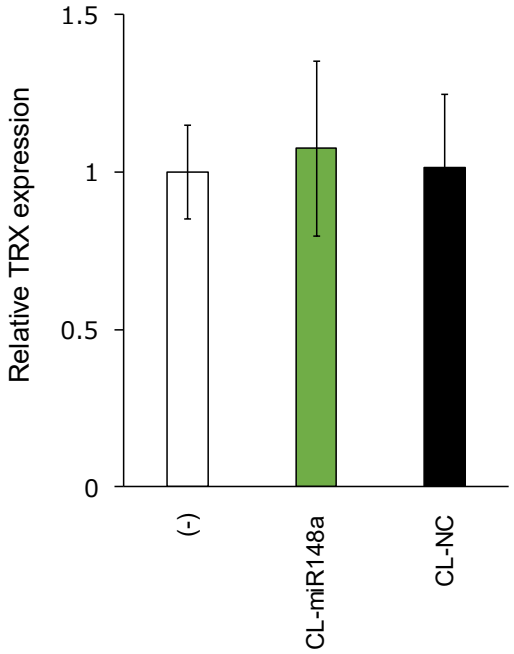

Figure 2.28
TRX mRNA expression level after AMO transfections. The mRNA expression values relative to the control without AMO were plotted against CL-AMOs. Error bars represent SD.

Chapter 3: Development of the system for evaluating drug response of cardiomyocytes

3.1 Abstract

Scanning electrochemical microscopy (SECM) can analyze the topography of sample surfaces non-invasively. In this chapter, I developed a cell assay device and system based on a SECM to analyze the activity of cardiomyocytes. For stable measurement of cardiomyocyte beating, I assembled a stage-top incubator and a capillary micropipette (MP) for delivering drugs with the SECM, and the responses of rat cardiomyocytes were analyzed under cultural environment after drug stimulation. Cardiomyocytes cultured on a pattern of islands and local addition of drugs by MP enabled us to evaluate drug effects multiple times in a single culture dish. I examined the effect of the cardiotoxic agent astemizole on cardiomyocytes. I detected extended relaxation duration of beating that is consistent with the known pharmacological properties of astemizole. Therefore, the SECM-MP system could evaluate the function of cardiomyocytes through analysis of time-course beating motion fluctuations.

3.2 Background

3.2.1 miRNAs in cardiac diseases

Functions of cardiomyocytes such as beating, homeostasis, and stress responses are controlled by various genes and signaling pathways and thus, altered expression of these genes cause cardiac diseases[128]. Recently, many miRNAs have been reported to involved in cardiac diseases[129]. Like its function in cancer cells, up-regulation and down-regulation of miRNAs contribute cardiac development, disease progression and regeneration through regulation target gene expressions[130]. It was reported that overexpression of miR-99a or down-regulation of miR-433 improved myocardial infarction in mouse model[131,132]. Therefore, miRNAs are possible therapeutic strategy of cardiac diseases, and it is necessary to study the roles of miRNAs on cardiomyocyte functions.

3.2.2 Evaluating cardiotoxicity is required in development of new drugs

Many drugs have been withdrawn from commercial markets because of potential risks to patients[133,134]. Most of the risks are cardiotoxic without regard to specific diseases[133,135]. Therefore, in the developmental phase of drug development, analyses of cardiomyocyte responses to candidate agents are important to evaluate the drug's pharmacological and toxicological properties[136]. In many cases, the measurement of action potentials by a microelectrode array has been used to analyze cardiotoxicity[137]. However, electrophysiological methods cannot eliminate non-beating cells and non-cardiomyocytes, which may cause errors in the data. By using a fluorescent calcium indicator, the imaging of calcium signaling is also used to examine cardiomyocyte contraction[138,139]. However,

fluorescent indicators may cause photodamage[140]. These studies were focused on the physiological processes of cardiomyocytes and did not reveal information on the beating properties of cardiomyocytes.

3.2.3 Analysis of cardiomyocyte beatings

Atomic force microscopy (AFM) is used to analyze the mechanical properties of cardiomyocytes[141]. AFM is not invasive, but a small cantilever probe makes direct contact with the cardiomyocytes. An impedance-based assay has also been used to analyze the beating properties of cardiomyocytes[142]. The impedance signal varies according to the movement of cardiomyocytes that are seeded on an electrode. These signals are a mixture of beating and non-beating cells. Recently, video-based analytical methods have been applied to evaluate the beating kinetics of cardiomyocytes[143–146]. The non-invasive movies are analyzed by several different computational methods.

3.2.4 Analysis of beating of cardiomyocyte and SECM application

Scanning electrochemical microscopy (SECM) is a kind of scanning probe microscopy technique in which a microelectrode is scanned surface of sample recording the current response[147]. Recently, SECM is used for the analysis of various biomaterials such as enzyme activity[148,149], cellular metabolism[150–152], and cellular status[153,154]. Hirano *et al*. have also reported a SECM-based system that could analyze the contraction kinetics and oxygen consumption of cultured cardiomyocytes[155]. Because SECM is a non-invasive and high-resolution method using a microelectrode, it can measure both the shape and motion of a single living cell[156–159] and is therefore well suited for the analysis of cardiac beatings.

The activity of cardiomyocytes is significantly sensitive to temperature or pH changes[160,161]. Thus, a stage-top incubator that consists of a sealed chamber is essential for the accurate analysis of cardiomyocyte activities[140,162,163]. However, because SECM requires strict control of the microelectrode position at a resolution in the order of nanometer, it is difficult to perform SECM measurements in a sealed chamber. Therefore, at present only a temperature controlled-plate has been used for SECM experiments on living cells[151,155,156].

Because the drug response of cardiomyocytes appears immediately after drug stimulation[164], motion measurement and drug stimulation should be performed simultaneously in the analysis of initial drug responses. However, it is difficult to perform SECM measurements during drug stimulation because the SECM measurement is easily perturbed by conventional drug stimulation methods that add the drug solution to the entire culture medium. Hirano *et al*. previously reported a SECM-based micropipette (MP) system for localized drug delivery that targets a single cell[165]. In this system, the SECM measurement was performed with drug delivery and the microelectrode current signals were

used to control the amount of drug administered. It is expected that this system might be applicable to the analysis of cardiac beating.

In this chapter, I developed a new system for the evaluation of the drug response of cardiomyocytes. I constructed a sealed chamber on an SECM to maintain a stable culture environment. I also fit a local drug delivery system to the chamber. I confirmed that the SECM-MP system could stimulate cardiomyocytes, then analyzed beating fluctuations using ATP solution. Furthermore, I evaluated the effect of astemizole, a cardiotoxic agent, by analyzing the cell contraction and relaxation behaviors.

3.3 Result and Discussion

3.3.1 Introduction of stage-top incubator to SECM

The beating rate of cardiomyocytes is significantly affected by environmental factors such as temperature or pH[160,161]. To accurately analyze the beating of cardiomyocytes by SECM, a stage-top incubator with a chamber was necessary. However, there have not been any reports on a SECM with a chamber[155,159,166,167] because it is very difficult to control the microelectrode position in a sealed space. Therefore, I constructed a sealed chamber that enabled free movement of the microelectrode, it was set on a metal base to avoid prevention of stage movement (Fig. 3.1A). In addition, sensors for

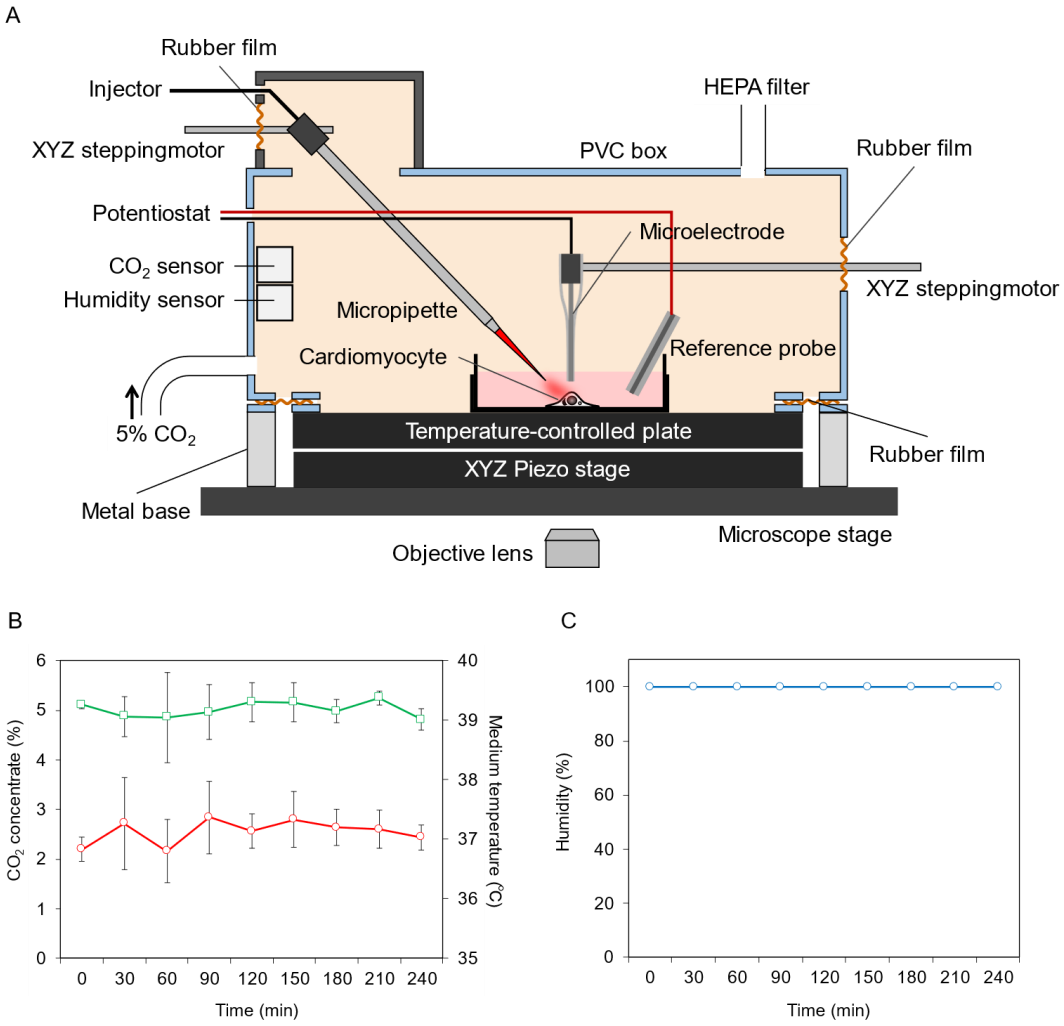

Figure 3.1
Maintaining the SECM system environment. (**A**) Schematic diagram of SECM and the MP system. (**B**) Time course of CO_2 concentration and medium temperature. Green line indicates CO_2 concentration and red line indicates medium temperature. Medium temperature was measured using a probe thermometer that was inserted into the medium directly. (**C**) Time course of humidity inside of the chamber.

carbon dioxide (CO_2) and humidity were set in the chamber. The temperature of the culture medium and the CO_2 concentration in the sealed chamber were maintained within a margin of error of ±0.5°C and ±0.3% for 4 hours, respectively (Fig. 3.1B). Humidity was maintained at 99.9% (Fig. 3.1C). I monitored the beating motion of rat cardiomyocytes incubated in this chamber by measuring microelectrode current with a time resolution of 10 ms to detect beating motions in the range from 200 to 500 ms[168,169]. The spatial resolution of this SECM was previously described[155] and could detect motions smaller than 1 μm. Because the microelectrode current value primarily depends on the distance between the microelectrode and the cell surface[155], when the microelectrode was set above a beating cardiomyocyte, the current waveform corresponding to the beating motion was continuously measured (Fig. 3.2). These results demonstrated that the microelectrode position could be controlled in the sealed chamber and confirmed that the beating rate was constant for at least 2 hours (Fig. 3.2).

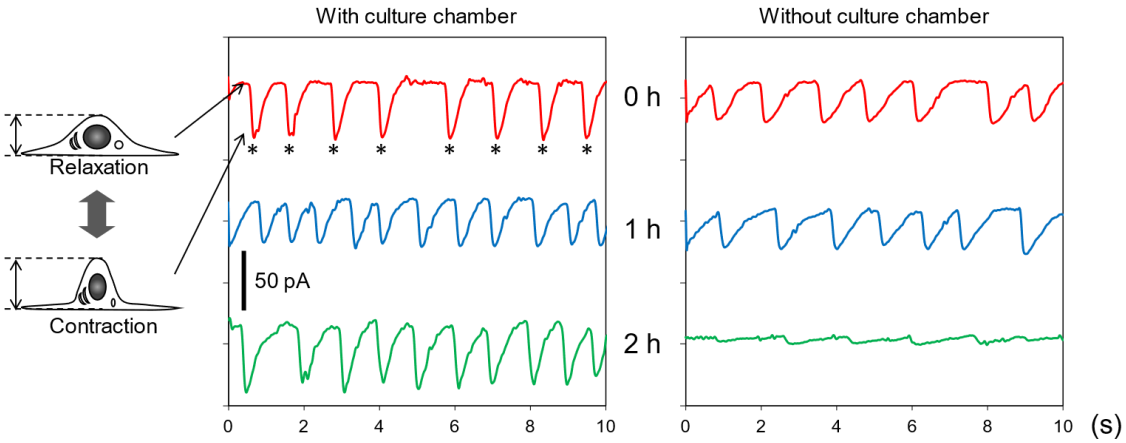

Figure 3.2
Measurements of cardiac beating motion for 2 hours. The waveforms are plots of the current data corresponding to the cardiomyocytes motion. The scale bar, shown in the panel, indicates the reference value for current changes. Asterisks indicate peaks of waveforms that pinpoint the most contracted state of the cell. Left panel shows beating motion with culture chamber while right panel shows without culture chamber.

3.3.2 Introduction of capillary micropipette to SECM

Opening the sealed chamber causes vibrations and electrical noise that prevent the SECM from measuring cardiomyocytes beating. Thus, drug stimulation should be performed in a sealed chamber without contact. Hirano *et al*. have developed a capillary micropipette (MP) connected to SECM[165]. I constructed the MP in a sealed chamber (Fig. 3.1A) to perform beating measurements and drug stimulation simultaneously. The MP was positioned obliquely upward of the microelectrode. The drug amount delivered from the MP was controlled by feedback control system using microelectrode current signals. To examine drug delivery performance and electrical noise in the sealed chamber, I monitored the diffusion of the delivered solution. When the delivery volume was set much larger than

what was to be delivered to cells, the delivered solution spread by up to about 250 μm radii (Fig. 3.3). Furthermore, because no noise current was detected during drug delivery, this SECM-MP system has the potential for the measurement of contraction kinetics during drug stimulation under cell culture conditions.

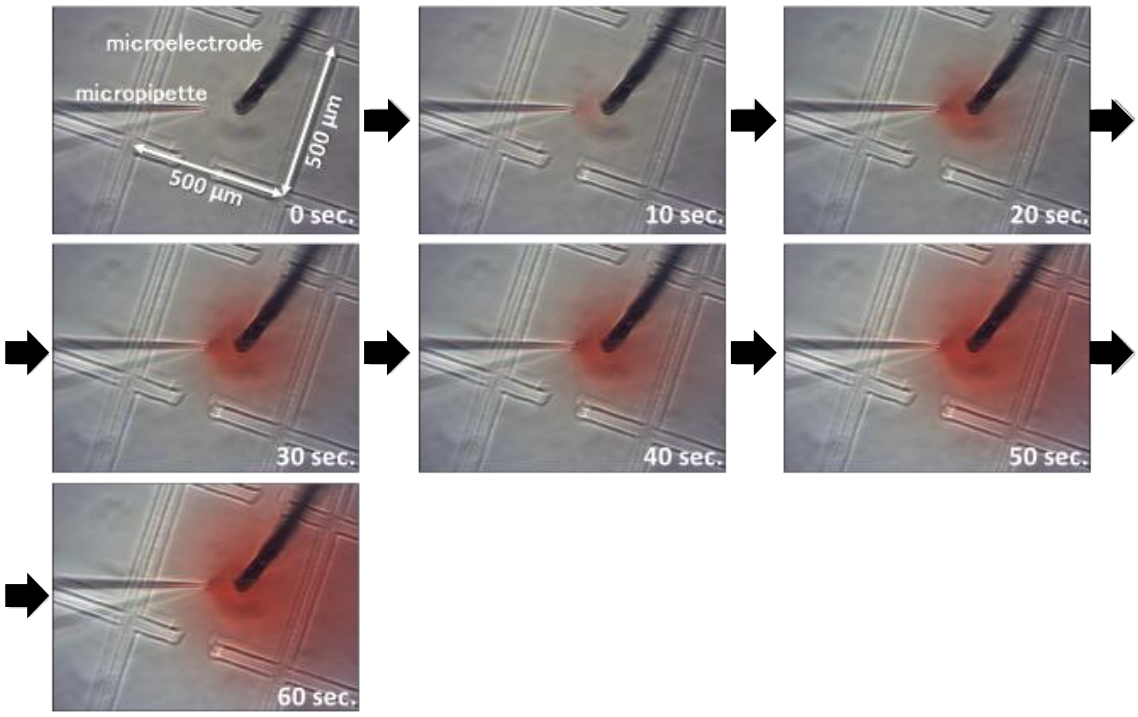

Figure 3.3
Diffusing images of drug solution that was locally delivered. To visualize movement of the drug solution, colored water was delivered and observed using a microscope.

3.3.3 Analysis of beating fluctuations cardiomyocytes in response to ATP delivered by the MP

As previously reported[170,171], since adenosine triphosphate (ATP) enhances the contractility of cardiomyocytes, beating rate was increased by ATP added to the entire medium at 50 μM ("ATP" in Fig. 3.4A). However, when ATP was delivered from the MP, targeting a single cardiomyocyte that was cultured in the 35-mm culture dish, no beating fluctuations were induced ("ATP-MP" in Fig. 3.4A), even though the ATP concentration around the target cell was approximately 500 μM. It was unclear why locally added ATP did not affect the rhythm of the cardiomyocytes in the culture dish. When I focused on the synchronization of the beating rhythm of the cardiomyocytes in the culture dish[172,173], I hypothesized that synchronous signals from neighboring cells of the target cell might counteract the effects of the added ATP (Fig. 3.4B upper-panel).

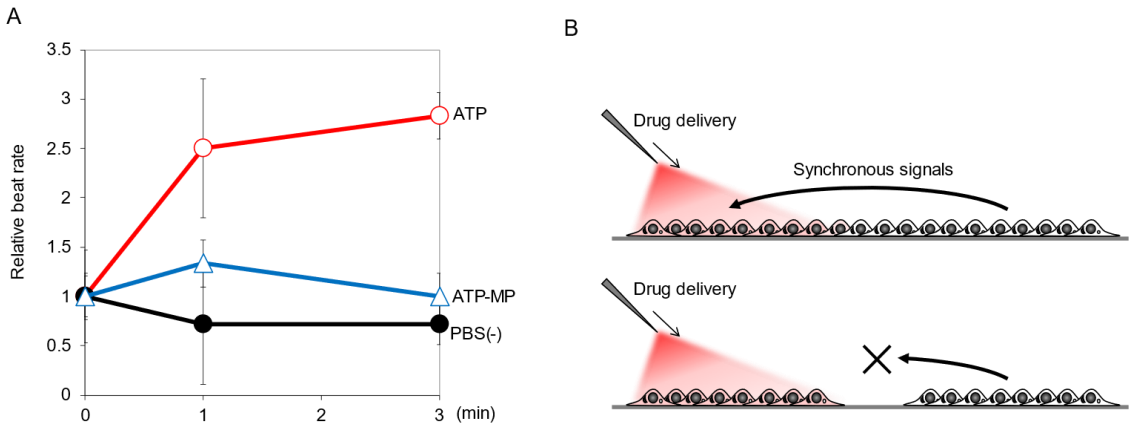

Figure 3.4
Beating difference between direct or MP stimulations. (**A**) Time-course of beat rates after stimulation with ATP or PBS(-). ATP or PBS(-) solutions were added to the entire medium (indicated with ATP or PBS(-)) or locally delivered using the MP (ATP-MP). The beat rates after ATP/PBS(-) stimulation (1 and 3 min) are indicated as relative values to the beat rates before ATP/PBS(-) stimulation (0 min). (**B**) Schematic views of desynchronization of cardiomyocytes.

To isolate a target cardiomyocyte from the synchronous rhythm in the culture dish, I introduced a micropatterning tool[174] that enabled me to make various sizes (80-1000 µm in diameter) of disc-shaped cell islands in the 35-mm culture dish (Fig. 3.4B lower-panel and Fig. 3.5A). Four days after seeding the cardiomyocytes, it was observed that cardiomyocytes in the same island were synchronized whereas each island was mutually independent. When ATP was delivered using the MP to a cellular island, the beating rate was significantly increased by approximately 2.5 times compared to the initial

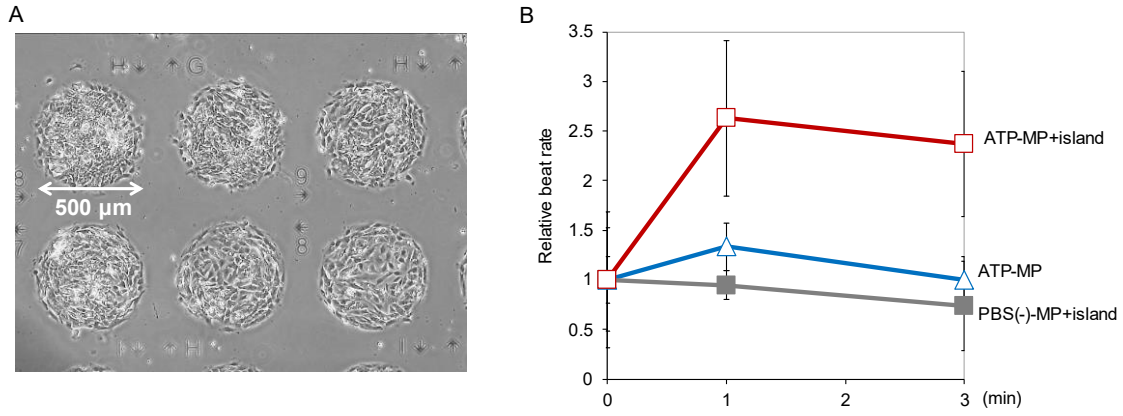

Figure 3.5
Motion fluctuations of cardiomyocyte cultured on islands. (**A**) Phase-contrast image of cardiomyocytes cultured on a micropatterned surface. The cellular islands that are 500 µm in diameter are indicated. (**B**) Time-course of beat rates with stimulation by ATP or PBS(-) that was locally delivered. The beat rates after ATP/PBS(-) stimulation (1 and 3 min) are indicated as relative values to the beat rates before ATP/PBS(-) stimulation (0 min).

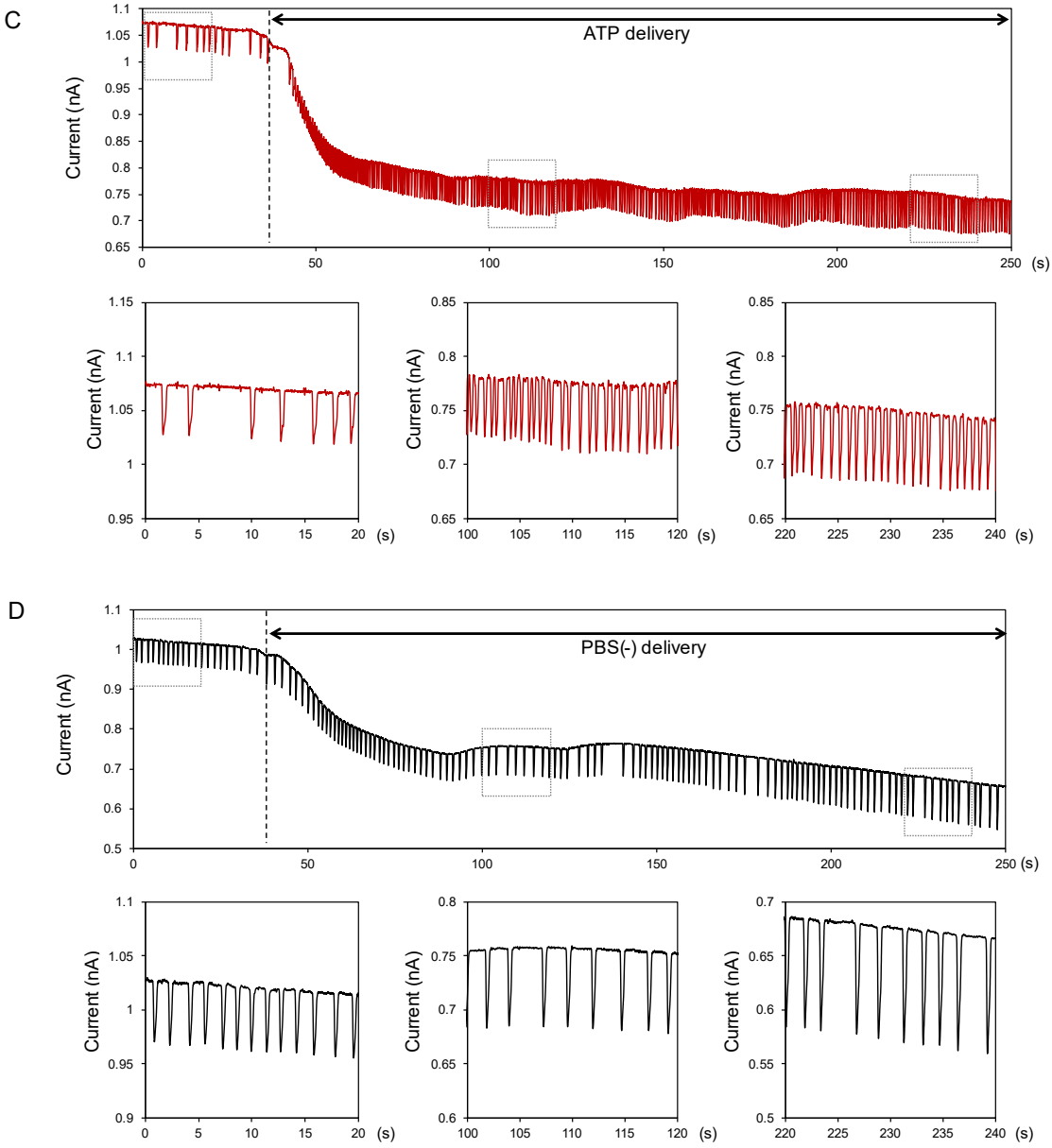

Figure 3.5 (Continued)
Time-course measurement of the cardiomyocyte beating after stimulation with ATP (**C**) or PBS(-) (**D**). Upper panel shows whole relative current data from 0 s to 250 s. Lower panels show extracted current data for 20 seconds from 0 s to 20 s, from 100 s to 120 s and from 220 s to 240 s respectively.

beating rate ("ATP-MP+island" in Fig. 3.5B and C). The calculated ATP concentration around the island was only 20 μM at most. The beating rate did not change when only buffer solution was delivered ("PBS(-)-MP+island" in Fig. 3.5B and D). These results indicated that the SECM-MP system could reproduce the same result as that of conventional addition of ATP to the entire medium (Fig. 3.4A). Furthermore, the beating of cardiomyocytes in an island 225-500 μm in diameter increased in response to ATP solution delivery, whereas no response was seen in 1000 μm islands.

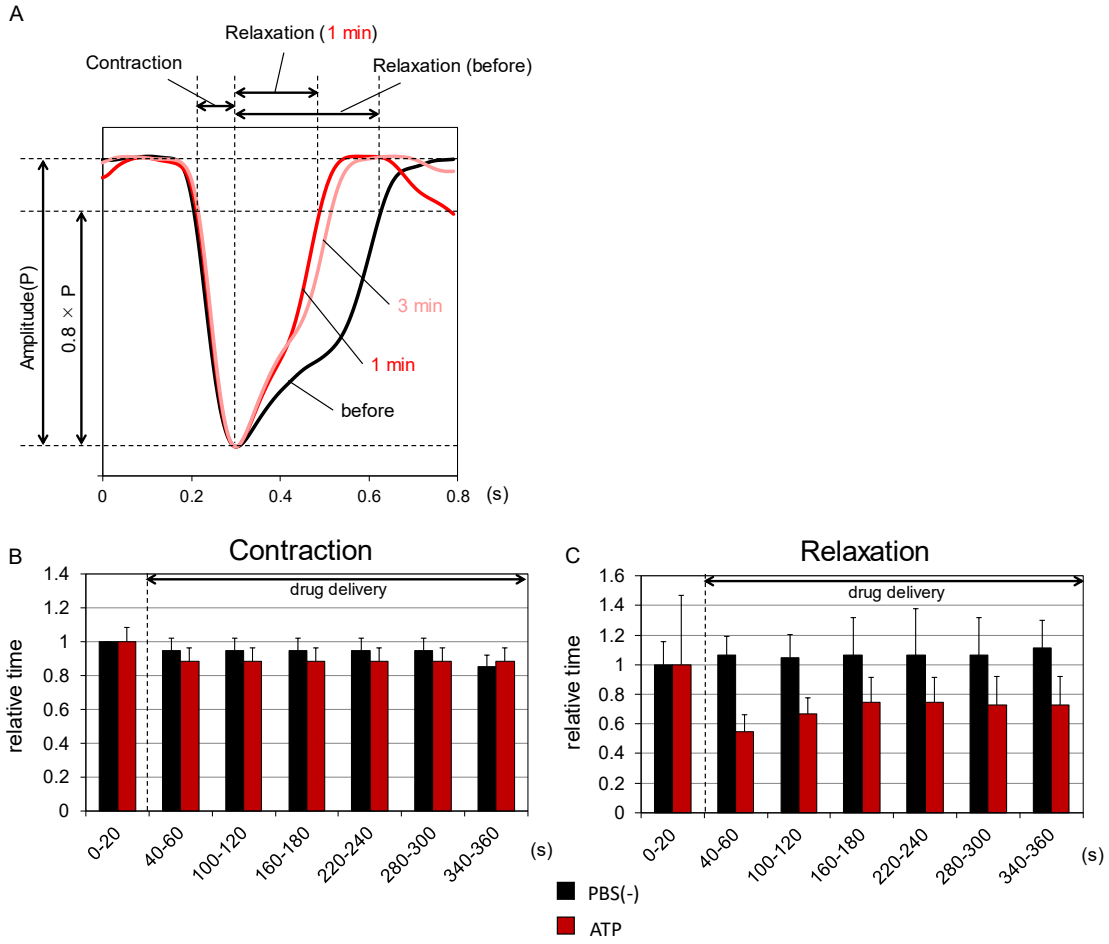

Figure 3.6

Analysis of beating changes of cardiomyocytes induced by ATP. (**A**) Comparison of the averaged beating waveforms before, 1 and 3 min after delivery of ATP. The duration of the contraction and relaxation were calculated based on the waveforms. (**B**) Contraction and (**C**) relaxation time of cardiomyocytes delivered with ATP or PBS(-). 0-20, 100-120, 220-240 s correspond to before (0 min), 1 min, 3 min respectively, as shown in (**B**) and (**C**). The relative times after ATP/PBS(-) stimulation are calculated on the basis of the time before ATP/PBS(-) stimulation.

Cardiomyocytes in islands smaller than 140 μm did not beat before ATP delivery. These sizes of cellular island were approximately consistent with the spread area of the locally delivered drugs (Fig. 3.3). Thus, it was revealed that to obtain the effect of drug stimulation using the MP, the drug solution should spread over the target cellular island that contains one group of synchronized cardiomyocytes.

The contraction and relaxation fluctuations were analyzed by the software program that Hirano *et al.* previously developed[155] with slight modification. Briefly, a plot of current was extracted for 20 seconds each for 1 minute and averaged to a single waveform, and analyzed for the duration of motion (Fig. 3.6A). The calculated data showed that the relaxation duration was shortened after delivery of

ATP (Fig. 3.6A-C). Therefore, it was shown that the SECM-MP system could induce a beating in response to drugs and analyze the time-course beating fluctuations before and during drug stimulation.

Drugs were locally delivered to target cells, but it was unclear whether cells in separate islands were affected by drugs diffusing through the culture medium. ATP was added from the MP targeting a cellular island ("drug target island" in Fig. 3.7A). The beating motion of the cardiomyocytes was measured at a drug target island or at another island located downstream ("downstream island" in Fig. 3.7A). At the drug target island, the beating rate was increased, whereas no changes were detected at the downstream island (Fig. 3.7B). The same result was obtained when the beating fluctuation was measured at a side island ("side island" in Fig. 3.7A and B). These results show that the area affected by the drug could be limited around the target cells to quite a small distance. The total delivered amount of ATP in each measurement was only about 1 nmol and it was diffused and diluted to around 0.5 pM in the culture medium. Thus, serial treatments with multiple drugs would be possible in one culture dish by replacing the drug target island, and the SECM-MP system shows promise for application to multiple drug screening.

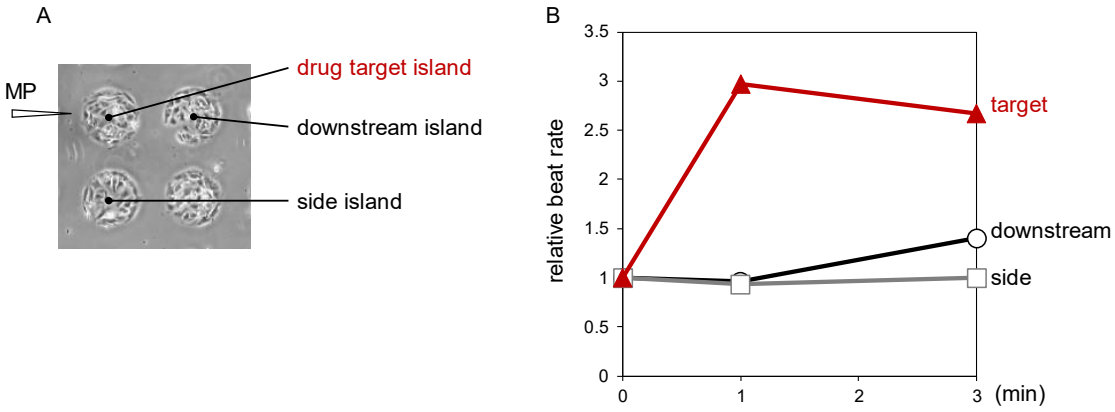

Figure 3.7
Effect of ATP on neighboring islands. (**A**) Layout of the drug target island and the beating measurement island. Because ATP was delivered from the left, obliquely upward of the target island, the right island positioned downstream in this image. (**B**) Beating changes of cardiomyocytes in each island. The beat rates after ATP stimulation (1 and 3 min) are indicated as relative values with the beat rates before ATP stimulation (0 min).

3.3.4 Application of SECM system for analyzing the effect of the cardiotoxic agent astemizole

Astemizole has been developed as a second-generation antihistamine drug, but was withdrawn from the market due to its cardiac toxic effect[175]. When I added astemizole to the entire medium using the previous SECM system[155], beating fluctuations could not be measured because the cardiomyocytes stopped beating. I then investigated whether the SECM-MP system could evaluate the toxicity of astemizole through motion fluctuations. When astemizole was added to one of the cardiomyocyte

islands from the MP at 24 nM, the beating motion of the cardiomyocytes changed as the stimulation time increased (Fig. 3.8A). As shown in the average waveforms (Fig. 3.8B), calculated as for ATP previously, the duration of the contractions did not change before and after stimulation with astemizole (Fig. 3.8B and C), but the relaxation duration was specifically prolonged, showing a five-fold increase after 5 minutes stimulation (Fig. 3.8B and D). No motion fluctuations were observed when delivering a control solution that did not contain astemizole (Fig. 3.8C-E). These motion fluctuations are consistent with the known pharmacological properties of astemizole. Astemizole is known to block cardiac potassium channels and causes prolongation of depolarization of the cardiac action

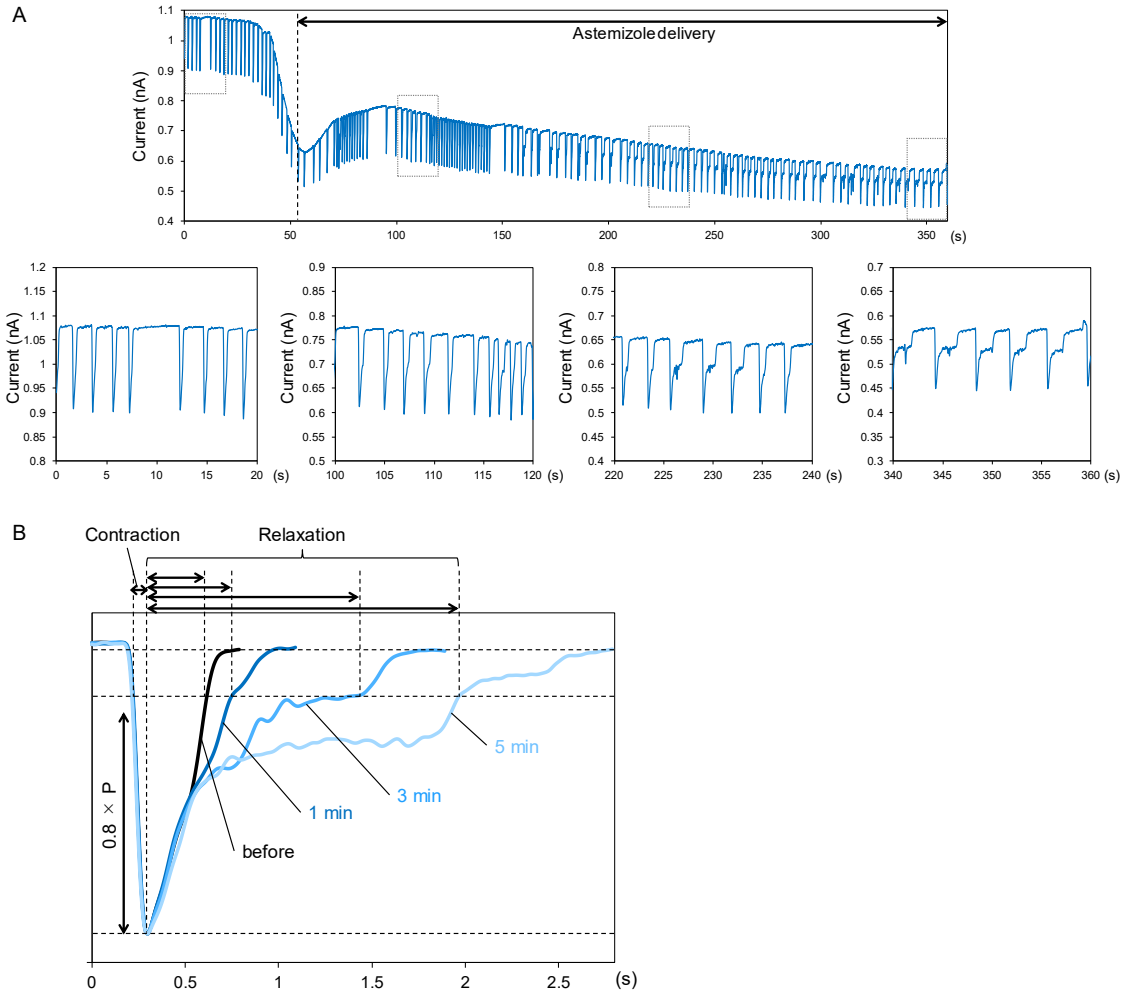

Figure 3.8
Beating of cardiomyocytes with astemizole or control solution stimulations. (**A**) Time-course measurement of cardiomyocyte beating with stimulation by astemizole. Upper panel shows the whole relative current data. Lower panels show extracted current data for 20 seconds from 0 s to 20 s, from 100 s to 120 s, from 220 s to 240 s and from 340 s to 360 s respectively. (**B**) Comparison of averaged waveforms before, 1 min, 3 min and 5 min after delivery of astemizole.

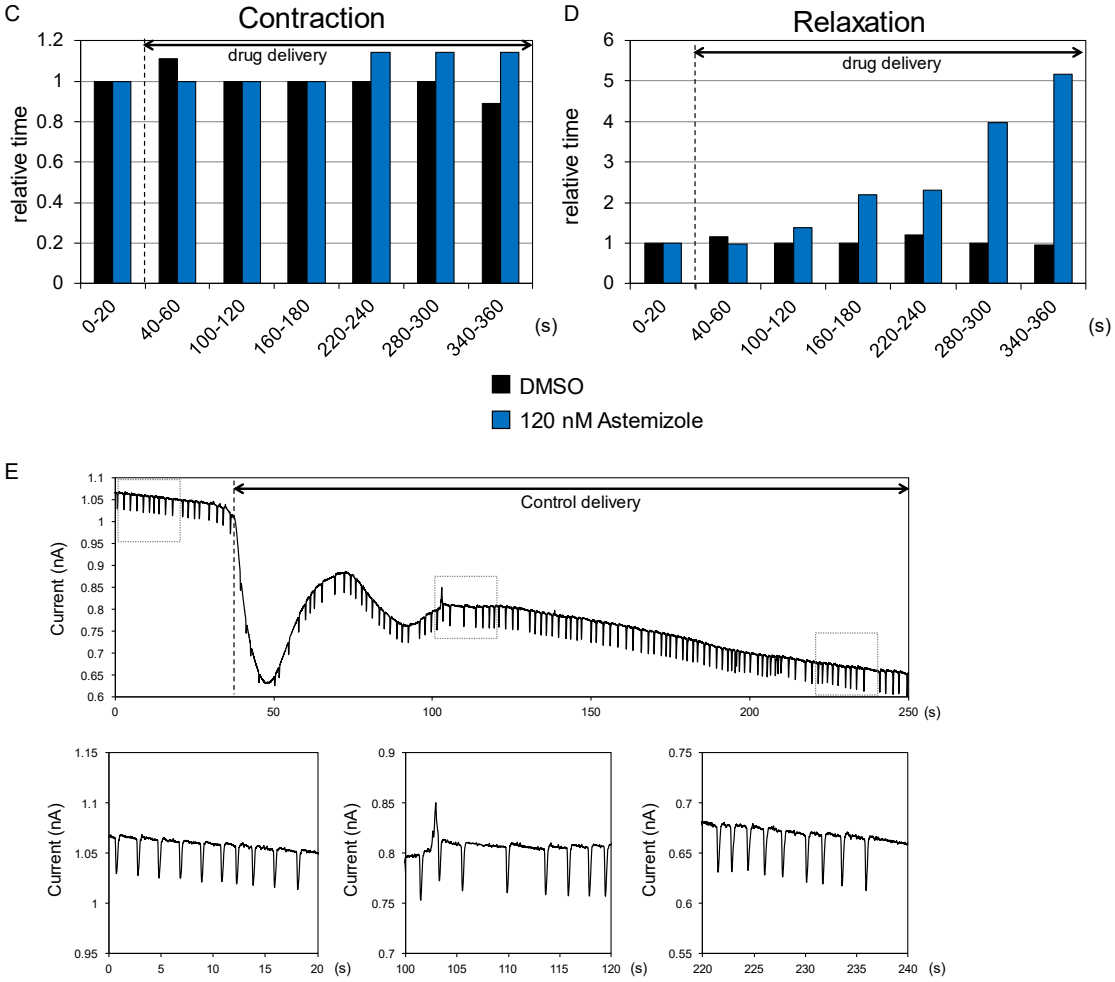

Figure 3.8 (Continued)

(**C**) Contraction and (**D**) relaxation times of cardiomyocytes delivered astemizole or control solutions. Control solution contains only dimethyl sulfoxide (DMSO), the solvent of astemizole. 0-20, 100-120, 220-240, 340-360 s correspond to before, 1 min, 3 min, 5 min respectively, as shown in (**B**). The relative times after astemizole/control stimulation are calculated on the basis of the time before astemizole/control stimulation. (**E**) Time-course measurement of cardiomyocyte beating with stimulation by a control solution. The extracted current data for 20 seconds from 0 s to 20 s, from 100 s to 120 s, and from 220 s to 240 s are shown in lower panels.

potentials[176]. It is called QT prolongation and may lead to sudden death[177]. Because depolarization leads to contraction of the cardiomyocytes[178], QT prolongation might appear as a continuation of contraction and a delay of relaxation. Thus, I can analyze the effect of astemizole by using motion fluctuations as a replacement for the conventional electrophysiological method. Therefore, it was suggested that the SECM-MP system could evaluate the cardiotoxicity of a drug by applying beating fluctuations as an index and reveal new pharmacological properties of drugs that might be missed with conventional electrophysiological methods.

Chapter 4: Conclusion

In this dissertation, I analyzed the cell functions of breast cancer and cardiac disease, which are important not only in Japan but also in the world. In both cases, I have developed methods and tools to clarify cell functions that had not be clarified by conventional methods.

In **Chapter 2**, I first investigated whether CL-AMO could prevent endogenous miRNA function and induce cell proliferation suppression targeting a typical oncogenic miRNA, miR-21. As a result, CL-AMO showed stronger cell proliferation inhibitory activity than other AMOs, which is consistent with the results previously shown by the luciferase reporter assay. Since CL-AMO indicated high target specificity and long-term stable activity even at low concentrations, it proved to be a high-performance AMO that should be used by many miRNA researchers. This result also suggests that CL-AMO can be applied to new nucleic acid drugs for the treatment of BC.

Next, I focused on miR-148a, which has a low expression level in BC and will be difficult to suppress. Since miR-148a has been reported as a tumor suppressor, inhibition by AMO may increase cell proliferation. Surprisingly, however, inhibition of miR-148a by CL-AMO inhibited the growth of BC cells, and the effect was stronger than that of miR-21. In addition, the proliferation inhibitory effect was consistent with changes in *TXNIP* expression, suggesting that miR-148a may function to promote cell proliferation targeting *TXNIP*. Because other AMOs did not indicate changes in the cell proliferation and *TXNIP* expression, oncogenic function of miR-148a was first revealed by complete suppression by CL-AMO. These different results depending on the inhibitory activity of AMO showed that the importance of choosing the AMO to be used for miRNA research correctly.

In **Chapter 3**, I developed SECM-MP system that can monitor changes in cardiomyocyte beating caused by drug stimulations in real time for a long time. Furthermore, cardiomyocytes cultured on a pattern of islands and local addition of drugs by MP enabled us to evaluate drug effects multiple times in a single culture dish. These results can also save valuable cells and drugs.

After performance evaluation of SECM-MP using ATP, I examined whether the cardiotoxic effect of astemizole could be analyzed. The SECM-MP system detected prolongation of relaxation duration of beating, and this result was only induced by the addition of astemizole by MP. Therefore, it is suggested that only this SECM-MP system could analyze beating fluctuations caused by astemizole. From these results, it is considered that the SECM-MP system has the potential to discover cardiomyocyte functions that could not be found by conventional analysis methods and will greatly contribute to cardiomyocyte research. Furthermore, it is suggested that this SECM-MP system also contributes to drug discovery where safety evaluation using cardiomyocytes is essential.

Finally, I hope that these tools developed in this dissertation will provide new insights in both miRNA in cancers and cardiomyocyte research in the future.

Chapter 5: Materials and methods

5.1 Methods for Chapter 2

5.1.1 Preparation of AMOs

Locked nucleic acid (LNA) miR-21 inhibitor (miRCURY LNA miRNA inhibitor) was purchased from QIAGEN (Hilden, Germany). Anti-miR-21-5p tough decoy (TuD-miR21) RNA was purchased from Sigma-Aldrich (MISSION Synthetic microRNA Inhibitor; Saint Louis, MO, USA). Anti-miR-148a-3p tough decoy RNA was purchased from GeneDesign Inc. (Osaka, Japan). 22-mer single stranded anti-hsa-miR-148a-3p was chemically synthesized from 2'-*O*-methyl RNA (MeRNA) (GeneDesign Inc.). All CL-AMOs (CL-miR21, CL-NC, CL-miR148a, CL-miR148aM and CL-miR148b) were chemically synthesized from MeRNA. CL-AMOs were prepared according to previous reports with slight modification and the detail scheme is described in the **Chapter 2** (Fig. 2.13). The uracil DNA glycosylase (UDG) was purchased from New England Biolabs (Ipswich, MA, USA). The molecular weight of CL-NC, CL-miR148a, CL-miR148b and CL-miR148aM were confirmed by liquid chromatography–mass spectrometry (LC-MS). The electrospray ionization (ESI)-MS data of all CL-AMOs are shown below.

CL-NC, calculated 23392.25, found 23398.29;

CL-miR148a, calculated 23392.25, found 23396.57;

CL-miR148b, calculated 23392.25, found 23399.72;

CL-miR148aM, calculated 23456.03, found 23459.85.

5.1.2 Cell culture

The human BC cell lines MCF-7 and ZR-75-1 were obtained from the American Type Culture Collection (ATCC, Manassas, VA, USA). MCF-7 cells were cultured in Dulbecco's modified Eagle medium (DMEM; Cosmo Bio, Tokyo, Japan) supplemented with 10% fetal bovine serum (FBS; Biological Industries, Beit Haemek, Israel). ZR-75-1 cells were cultured in Roswell Park Memorial Institute (RPMI)-1640 medium (Thermo Fisher Scientific, Waltham, MA, USA) supplemented with 10% FBS. The cells were incubated in a humidified 5% CO_2 atmosphere at 37°C. These BC cell lines of passage number 1-10 were used for the following experiments.

5.1.3 Cell proliferation assay

MCF-7 cells were seeded onto a 96-well plate at a density of 2×10^3 cells/well and allowed to adhere overnight. ZR-75-1 cells were also seeded onto a 96-well plate at a density of 2×10^3 cells/well (inhibition of miR-21) or 1×10^3 cells/well (inhibition of miR-148a). Then, AMOs were transfected into the cells at final concentrations of 5, 10, and 20 nM using Lipofectamine 3000 (Thermo Fisher Scientific). When three wells were used for each AMOs, mixtures of A and B were prepared as shown in Figure 5.1. Then equal volume (50 μl) of mixture B was mixed with each mixture A and incubate

15 min at room temperature (LP mixture). After incubation, 90 µl of LP mixtures were added into 10-fold volume (900 µl) of culture media and mixed well by inversion. The media of pre-cultured BC cells were removed and add 100 µl/well of the LP mixture containing medium and incubate 3 days. After 3 and 6 days of transfection, I replaced the cell culture medium with fresh medium. The number of cells was assessed on day 0 (day of transfection) and on days 3, 6, and 9 post-transfection using the Cell Counting Kit-8 assay (CCK-8; Dojindo, Kumamoto, Japan) as follows. 1/10 volume (10 µl) of CCK-8 solution containing WST-8 dye was added to the cell culture medium, and the absorbance at 450 nm was measured 90 min post-incubation in a humidified 5% CO_2 atmosphere at 37°C using a microplate reader (TECAN, Mannëdorf, Switzerland). The cell number was expressed relatively to the value for no AMO control (single-point analysis at 6 days post-transfection) or for the day of transfection (day0) (time-course analysis for 9 days).

	Final Conc. (nM)	P3000	10 µM AMO stock	Opti-MEM	Total	
A-1	0	2.0	0.0	48.0	50.0	
A-2	5	2.0	0.5	47.5	50.0	
A-3	10	2.0	1.0	47.0	50.0	
A-4	20	2.0	2.0	46.0	50.0	(µl)

	LP3000	Opti-MEM	Total	
B	13.2	206.8	220.0	(µl)

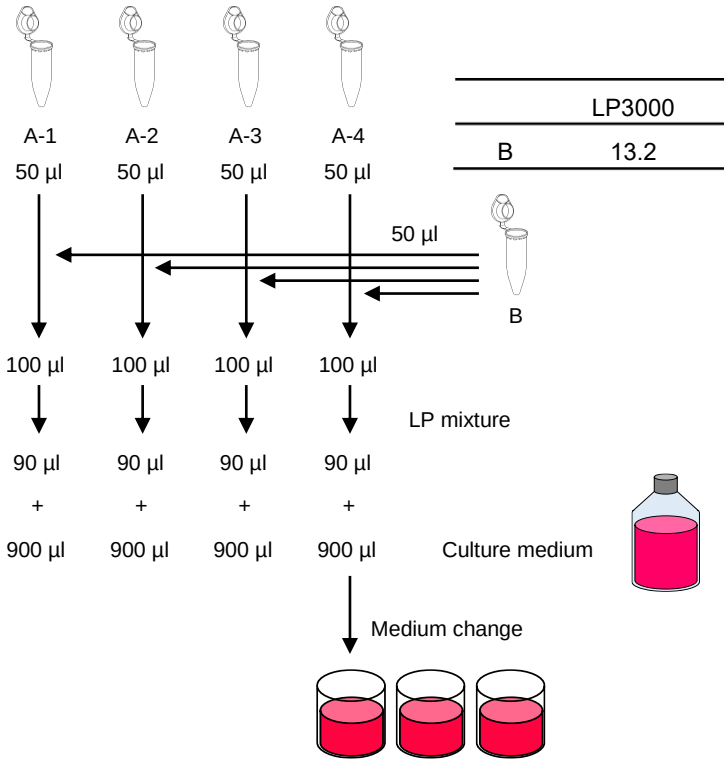

Figure 5.1
Preparation of transfection mixture. This schematic image shows the case of an experiment with a 96-well plate.

5.1.4 Quantitative analysis of miRNA expression

Untreated MCF-7 and ZR-75-1 cells were harvested using TRI Reagent (Molecular Research Center, Cincinnati, OH, USA). miRNAs were isolated using the miRNeasy Mini Kit (QIAGEN) as described below. 40 µl of chloroform was added into 200 µl of TRI Reagent containing BC cell lysate in a microtube, and the tube was shaken. The microtubes were placed at room temperature for 3 min and centrifuged for 15 min at 12,000 ×*g* at 4°C. The upper aqueous phase was transferred to a new microtube followed by addition of 210 µl of 100% ethanol and mixed by pipetting. The sample mixture was pipetted into miRNeasy mini spin column and centrifuged for 15 s at 8,000 ×*g*. The flow-through was discarded. 700 µl of Buffer RWT was added into the column and centrifuged for 15 s at 8,000 ×*g*. The flow-through was discarded. 500 µl of Buffer RPE was added into the column and centrifuged for 15 s at 8,000 ×*g*. The flow-through was discarded. 500 µl of Buffer RPE was added again into the column and centrifuged for 2 min at 8,000 ×*g*. The flow-through was discarded. The column was placed into a new 2 ml microtube and centrifuged for 1 min at 12,000 ×*g*. The column was transferred to a new 1.5 ml microtube. 50 µl of RNase-free water was pipetted onto the column membrane and the column was centrifuged for 1 min at 8,000 ×*g*. The concentration of eluted sample containing miRNAs was measured using a microvolume spectrophotometer (DeNovix, Wilmington, DE, USA).

Complementary DNA (cDNA) was synthesized from 10 ng of miRNAs using the TaqMan MicroRNA Reverse Transcription Kit and TaqMan MicroRNA Assay (Thermo Fisher Scientific). The reaction mixture was prepared as described in Table 5.1 and incubated as follows, 30 min at 16°C, 30 min at 42°C, and 5 min at 85°C.

Table 5.1
Composition of reaction mixture for cDNA synthesis from miRNA. Unit: µl.

dNTP mixture (100 mM each)	0.15
Multiscribe RT enzyme (50 unit/µl)	1.00
10× RT buffer	1.50
RNase inhibitor (20 unit/µl)	0.19
5× primer	3.00
2 ng/µl RNA sample	5.00
Nuclease-free water	4.16
total	15.00

Quantitative polymerase chain reaction (qPCR) was performed using the TaqMan Universal Master Mix II with LightCycler 96 system (Roche, Mannheim, Germany). The reaction mixture was prepared as described in Table 5.2 and the PCR condition was 95°C for 600 s, and 48 cycles of 95°C for 15 s and 60°C for 60 s. U6 RNA was used as an endogenous control to normalize the relative quantitation of target miRNAs.

Table 5.2
Composition of reaction mixture for qPCR of miRNA. Unit: µl.

20× primer	1
RT reaction mixture	5
TaqMan 2× Universal PCR master mix, no UNG	10
Nuclease-free water	4
total	10

5.1.5 Quantitative analysis of mRNA expression

For *PTEN* analysis, MCF-7 cells were seeded in a 96-well plate at a density of 2×10^3 cells per well and transfected with the CL-AMOs, as described above, at a final concentration of 10 nM. After 6 days post-transfection, the cells were harvested, merging six wells into one sample using 200 µl of the Buffer RLT Plus of the RNeasy Plus Mini Kit (QIAGEN). Total RNAs were extracted using the RNeasy Plus Mini Kit as follows. The MCF-7 cell lysate in the Buffer RLT Plus was transferred to gDNA Eliminator column and centrifuged for 30 s at 8,000 ×*g*. The flow-through was saved. Equal volume of 70% ethanol was added to the flow-through and mixed by pipetting. The sample mixture was pipetted into RNeasy mini spin column and centrifuged for 30 s at 8,000 ×*g*. The flow-through was discarded. 700 µl of Buffer RW1 was added into the column and centrifuged for 30 s at 8,000 ×*g*. The flow-through was discarded. 500 µl of Buffer RPE was added into the column and centrifuged for 30 s at 8,000 ×*g*. The flow-through was discarded. 500 µl of Buffer RPE was added again into the column and centrifuged for 2 min at 8,000 ×*g*. The flow-through was discarded. The column was placed into a new 2 ml microtube and centrifuged for 1 min at 12,000 ×*g*. The column was transferred to a new 1.5 ml microtube. 30 µl of RNase-free water was pipetted onto the column membrane and the column was centrifuged for 1 min at 8,000 ×*g*. The concentration of eluted sample containing mRNAs was measured using a microvolume spectrophotometer (Thermo Fisher Scientific).

cDNA was synthesized from 200 ng of total RNAs using the Superscript VILO cDNA Synthesis Kit (Thermo Fisher Scientific). The reaction mixture was prepared as described in Table 5.3 and incubated as follows, 10 min at 25°C, 60 min at 42°C, and 5 min at 85°C.

Table 5.3
Composition of reaction mixture for cDNA synthesis from mRNA. Unit: µl.

5× VILO Reaction Mix	4
10× SuperScript Enzyme Mix	2
RNA sample (200 ng)	X
Nuclease-free water	to 20
total	20

qPCR was performed using the PowerUP SYBR Green Master Mix (Thermo Fisher Scientific) with the QuantStudio Real-Time PCR system (Thermo Fisher Scientific). The PCR mixture was prepared as described in Table 5.4 and the PCR condition was 50°C for 2 min, 95°C for 10 min, 40 cycles of 95°C for 15 s and 60°C for 60 s.

Table 5.4
Composition of reaction mixture for qPCR of mRNA. Unit: µl.

2× PowerUp SYBR Green Master Mix	5.0
10 µM each primer	0.5
cDNA	1.0
Nuclease-free water	3.5
total	10.0

For other genes, MCF-7 cells were seeded onto a 48-well plate at a density of 4×10^3 cells per well and transfected with AMOs, as described above, at a final concentration of 20 nM or 50 nM. After 3 days post-transfection, the cells were harvested, merging three wells into one sample using 150 µl of Buffer RLT Plus. Total RNA extraction, cDNA synthesis and qPCR were performed as described above. Glyceraldehyde 3-phosphate dehydrogenase (*GAPDH*) expression to normalize target gene expressions and calculated the expression level of target genes as $2^{-\Delta Ct}$, where ΔCt = Ct(target)–Ct(*GAPDH*).

The following primers were used for PCR:

GAPDH (for PTEN) forward 5'- ACATCAAGAAGGTGGTGAAGCA-3'

GAPDH (for PTEN) reverse 5'- TCTTACTCCTTGGAGGCCATGT-3'

PTEN forward 5’-AAGACAAAGCCAACCGATAC-3’
PTEN reverse 5’-GAAGTTGAACTGCTAGCCTC-3’
GAPDH (for other genes) forward: 5’-TTGCCCTCAACGACCACTTT-3’
GAPDH (for other genes) reverse: 5’-TGGTCCAGGGGTCTTACTCC-3’
SLC7A11 forward: 5’-GGTTATTCTATGTTGCGTCTC-3’
SLC7A11 reverse: 5’-AATAACAGCTGGTAGAGGAG-3’
TXNIP forward: 5’-CTGATCTATGTTAGCGTTCC-3’
TXNIP reverse: 5’-TATCAGGGATGTTCAGATCTAC-3’
CPEB4 forward: 5’-GAGTTGCGTTCTCTAATCAAC-3’
CPEB4 reverse: 5’-ACCCGTTTATCTATCTCTCC-3’
SLC7A5 forward: 5’-TCCAGATCGGGAAGGGTGAT-3’
SLC7A5 reverse: 5’-CAGGGGCAGGTTTCTGTAGG-3’
LAMA4 forward: 5’-GAAATTGCATTTGAAGTCCG-3’
LAMA4 reverse: 5’-ACCTGTCCATTTTTCATGTG-3’
TRX forward: 5′ -TGGTGAAGCAGATCGAGAGC-3′
TRX reverse: 5′ -CATTTTGCAAGGCCCACACC-3′ .

5.1.6 Immunoprecipitation of Ago2 complex and detection of CL-miR148a

2.8 × 10^6 MCF-7 cells were seeded separately in three 75 cm^2 flasks and transfected with CL-miR148a at a final concentration of 2 nM. Next, 24 h post-transfection, the cells were harvested using cell scraper and performed IP of the Ago2 complex using the microRNA Isolation Kit, Human Ago2 (Wako, Osaka, Japan) as follows.

For preparation of anti-Ago2 antibody beads, 50 μl of Anti-Human Ago2 Antibody Beads Solution was pipetted to a microtube and centrifuged for 30 s at 3,000 ×*g* at 4°C. The supernatant was discarded. 850 μl of Cell Lysis Solution was added to the beads pellet followed by suspension and the microtube was centrifuged for 30 s at 3,000 ×*g* at 4°C. The supernatant was discarded.

For IP reaction, 850 μl of Cell Lysis Solution was added to the cell pellet and suspended by pipetting. After 10 min incubation on ice, the cell suspension was centrifuged for 20 min at 20,000 ×*g* at 4°C. Then, the supernatant was mixed with the beads prepared above and incubated for 3 h with rotation at 4°C. The cell lysate-beads mixture was centrifuged for 30 s at 3,000 ×*g* at 4°C and the supernatant was discarded. 850 μl of Cell Lysis Solution was added to the beads pellet followed by suspension and the microtube was centrifuged for 30 s at 3,000 ×*g* at 4°C. The supernatant was discarded. The above step was repeated a total of 3 times. 50 μl of Elution Solution was added to the beads and mixed by vortex mixer. The beads suspension was centrifuged for 30 s at 3,000 ×*g* at 4°C. The supernatant was transferred to a new microtube, and 350 μl of sterile water was added. 400 μl of phenol/chloroform was added to the microtube and mixed by vortex mixer. The microtube was centrifuged for 10 min at

20,000 ×*g*. The upper aqueous phase was transferred to a new microtube followed by addition of 400 µl of chloroform and mixed by vortex mixer. The microtube was centrifuged for 10 min at 20,000 ×*g*. The upper aqueous phase was transferred to a new microtube followed by addition of 3 µl of Ethachinmate, 40 ul of 3 M sodium acetate and 1 ml of 99.5% ethanol. The microtube was centrifuged for 15 min at 20,000 ×*g* at 4°C. 1 ml of 70% ethanol was added to the pellet and the microtube was centrifuged for 10 min at 20,000 ×*g* at 4°C. The pellet was dissolved in 20 µl of sterile water and the samples were merged from the three flasks into one sample.

The obtained sample and 2, 5, and 10 fmol of CL-miR148a were mixed with 2 × Gel Loading Buffer and electrophoresed for 1 h at 17-18 mA using 15% polyacrylamide gel containing 8 M urea. Oligonucleotides were transferred to positively charged nylon membrane (Roche) for 35 min at 5 V and UV cross-linked for 1 min. The membrane was put in a Hybri-Bag (Cosmo bio) and incubated for 2 h at 4°C.

For CL-miR148a detection, a digoxigenin (DIG)-tailed deoxyoligonucleotide probe for the miR-148a sequence was prepared using the DIG Oligonucleotide Tailing Kit, 2nd Generation (Roche) as follows. The reaction mixture was prepared as shown in Table 5.5 and incubated for 15 min at 37°C followed by addition of 2 µl of 0.2 M EDTA. 12 ml of DIG Easy Hyb (Roche) was added into the Hybri-Bag and the membrane was incubated for 20 min. 12 ml of DIG Easy Hyb containing 3 µl of DIG-tailed d-miR148a prepared above was added into the Hybri-Bag and subjected to hybridization with CL-miR148a on the membrane overnight.

Table 5.5
Composition of reaction mixture for DIG-tailing of deoxyoligonucleotide probe. The d-miR148a is a deoxyoligonucleotide contains the same sequence of miR-148a. Unit: µl.

d-miR148a	6.4
Sterile water	2.6
5× Reaction Buffer	4.0
$CoCl_2$ solution	4.0
DIG-dUTP solution	1.0
dATP solution	1.0
Terminal Transferase	1.0
total	20.0

The membrane was then washed twice with 25 ml of 2 × saline-sodium citrate (SSC) with 0.1% sodium dodecyl sulfate (SDS) for 5 min and 0.5 × SSC with 0.1% SDS for 15 min. After washing with 50 ml of wash buffer (DIG Wash and Block Buffer Set, Roche) for 5 min, the membrane was incubated for 30 min in 40 ml of blocking buffer (1% Blocking reagent (Roche) in 100 mM Maleic acid, 150

mM NaCl (pH 7.5)). The membrane was incubated for 30 min in 20 ml of 1:10000 diluted anti-DIG antibody in blocking buffer. Then the membrane was washed twice with 100 ml of wash buffer for 15 min followed by incubation for 5 min in 40 ml of detection buffer (0.1 M Tris-HCl (pH 9.5), 0.1 M NaCl). The membrane was incubated for 5 min in 4 ml of detection buffer containing 40 µl of 2.5 mM [3-(1-chloro-3'-methoxyspiro[adamantane-4,4'-dioxetane]-3'-yl)phenyl] dihydrogen phosphate (CSPD, Roche). The excess buffer was removed, and the membrane was incubated for 10 min at 37°C. Detection was performed with Lumino Graph (ATTO, Tokyo, Japan).

5.1.7 mRNA microarray

MCF-7 cells were seeded onto a 96-well plate at a density of 2×10^3 cells/well and mock-transfected or transfected with CL-miR148a at a final concentration of 20 nM. The cells were harvested merging thirty wells into one sample using 200 µl of TRI Reagent 3 days post-transfection. Purification of mRNA and mRNA microarray analysis were performed at Macrogen Japan (Tokyo, Japan) using the human Clariom S Assay (Thermo Fisher Scientific). The data were analyzed using Affymetrix GeneChip Command Console software (Thermo Fisher Scientific), and I compared differences in gene expression between mock-transfected and CL-miR148a-transfected samples.

5.1.8 TargetScan Analysis

I accessed the TargetScan (http://www.targetscan.org/vert_72/). The search condition was as follows, Select species: Human, Enter a human gene symbol: blank, and Select a broadly conserved microRNA family: miR-148-3p/152-3p. Genes whose expression was increased more than 1.5-fold in the mRNA array analysis were searched on Excel to see if they were included in the Targetscan results.

5.2 Methods for Chapter 3

5.2.1 Chemicals

Adenosine triphosphate (ATP) and astemizole were purchased from Sigma-Aldrich. ATP was dissolved in phosphate buffered saline (PBS(-)). Astemizole was dissolved in dimethyl sulfoxide (DMSO) to procedure a stock solution, and diluted with PBS(-) before loading into the MP system.

5.2.2 Cell culture

All animal procedures were performed in accordance with the "Fundamental Guidelines for Proper Conduct of Animal Experiment and Related Activities in Academic Research Institutions" stipulated by the Ministry of Education, Culture, Sports, Science and Technology and approved by the animal experiment committee of Cosmo Bio Co., Ltd.

Primary rat cardiomyocytes (#CMC03, Cosmo Bio) were cultured as previously described[155]. Briefly, cardiomyocytes prepared from neonatal rat ventricles were seeded on 35-mm dishes that were coated with collagen at a concentration of 2×10^5 cells/dish. These cells were then incubated in cardiomyocyte culture medium (Cosmo Bio) at 37℃ in a humidified atmosphere containing 5% CO_2. The medium was changed 2 days after seeding. For SECM experiments, I used spontaneously beating cells within 25 days in a culture. Before making a beating measurement, the culture medium was replaced with 2 ml/dish of serum-free medium that contained 1 mM potassium ferrocyanide ($K_4[Fe(CN)_6]$) that is an electron mediator of SECM measurement and 2% Knockout TM serum replacement (Thermo Fisher Scientific, Waltham, MA, USA) in DMEM/F-12 medium (Thermo Fisher Scientific).

5.2.3 Cell patterning

CYTOOchips^{TM} Arena FN (CYTOO, Cambridge, MA, USA) was placed on the bottom of a 35-mm dish and fixed at four corners of the glass chip using vacuum grease. Then cardiomyocytes were seeded in the same way as normal culture methods. For drug delivery experiments, I used relatively short-term cultured cardiomyocytes because the cell pattern was lost in long-term cultures. Serum-free medium, as described above, was used for the beating measurement.

5.2.4 SECM instrumentation

The basic part of the SECM instrument was built in my laboratory according to previous studies[155] with some of modifications. In brief, the central part of this SECM setup comprised an inverted phase-contrast microscope (NIKON, Tokyo, Japan), a piezomotor positioning system (Nano control, Tokyo, Japan), and a potentiostat (Hokuto Denko, Tokyo, Japan). The XYZ-axis stepping-motors (Suruga Seiki, Shizuoka, Japan) were introduced for electrode positioning. The software of the SECM system was constructed using LabView (National Instruments, Austin, TX, USA). I used a Pt microdisk

electrode (5-μm radius) as the electrochemical probe for SECM measurements and an Ag/AgCl electrode (Hokuto Denko) as the reference and auxiliary electrode.

The MP system was set up on the SECM system as previously described[165]. Briefly, the microinjector (Narishige, Tokyo, Japan) pressure was controlled by a stepping-motor. The MP position was also controlled by XYZ-axis stepping-motors. The MPs were fabricated from borosilicate capillaries (o.d./i.d.=1.0/0.6 mm with an inner filament) using a micropipette puller.

5.2.5 Environment maintenance system

A temperature controlled-plate (Tokai Hit, Shizuoka, Japan) was set on the piezomotor system. The piezomotor system was surrounded by a metal base. The chamber was made from polyvinyl chloride (PVC) with dimensions of 200 mm × 260 mm × 90 mm (length × width × height). The chamber had a small window sealed by a rubber film for the microelectrode shaft. A small box, that also had a sealed small window, was set on top of the PVC chamber for the MP. The chamber was put on the metal base and the bottom of the chamber was connected to the temperature controlled-plate via a rubber film (Fig. 3.1A). A CO_2 sensor (Kenis, Osaka, Japan), and a temperature and humidity sensor (T&D Corporation, Nagano, Japan) were placed in the PVC chamber. CO_2 gas was mixed with air to 5% using a gas mixer (Okolab, Pozzuoli, NA, Italy) and humidified through a bubbling humidifier (Tokken, Chiba, Japan), then drawn into the chamber. The PVC chamber was also connected to a HEPA filter unit to clean the inside then the door was opened.

5.2.6 Measurement of cardiomyocyte beating by SECM

The measurement procedures of beating cardiomyocytes by SECM were previously described[155]. Briefly, I positioned the microelectrode tip 9 μm away from a cell using an approach curve measurement, and subsequently measured the oxidation current of the ferrocyanide with a time resolution of 10 ms. To analyze the beating of the cardiomyocytes, a plot of the current response was studied using software developed in LabView. In addition to a previous version of the software that could calculate a peak-to-peak interval time, a beating rate and an average waveform, a new program in this study could also extract the current data within an optional time scale and correct for changes in background current due to the reduced sensitivity of microelectrode induced by metabolites within the cells. The time of contraction and relaxation were calculated as shown in Figure 3.6(A) according to previously described[155].

5.2.7 Control of drug delivery with MP

The MP positioning and delivery were controlled as previously described[165]. Briefly, the MP delivered a drug solution which did not contain any electron mediators upstream from the microelectrode into a medium containing 1 mM $K_4[Fe(CN)_6]$. The $K_4[Fe(CN)_6]$ oxidation currents

decreased depending on the delivery rate. The MP delivery was controlled with a feedback control system between the current signals and the microinjector pressure. The MP was positioned diagonally above the microelectrode to target cells (Fig. 3.1A). Before and after delivery, the MP tip was kept away from a target cell to prevent unexpected delivery caused by leakage from the MP tip. These operations were controlled using software developed with LabView. The program for controlling the MP system and the program for measuring the cardiomyocyte beating were operated cooperatively.

References

1. Ministry of Health, Labour and Welfare Japan. Summary Report of Annual Vital Statistics of Japan (2019). (2020). Available at: https://www.mhlw.go.jp/toukei/saikin/hw/jinkou/geppo/nengai19/index.html.
2. Bray, F., McCarron, P. & Parkin, D. M. The changing global patterns of female breast cancer incidence and mortality. *Breast Cancer Res.* **6**, 229–239 (2004).
3. J, F. *et al.* Global Cancer Observatory: Cancer Today. *International Agency for Research on Cancer* (2020). Available at: http://gco.iarc.fr/today.
4. Bray, F. *et al.* Global cancer statistics 2018: GLOBOCAN estimates of incidence and mortality worldwide for 36 cancers in 185 countries. *CA. Cancer J. Clin.* **68**, 394–424 (2018).
5. Cancer Information Service, National Cancer Center, Japan. Cancer Statistics. Available at: https://ganjoho.jp/reg_stat/statistics/data/dl/index.html.
6. Saika, K. & Sobue, T. Epidemiology of breast cancer in Japan and the US. *Japan Med. Assoc. J.* **52**, 39–44 (2009).
7. Machii, R. & Saika, K. Incidence rate for breast cancer in Japanese in Japan and in the United States from the Cancer Incidence in Five Continents. *Jpn. J. Clin. Oncol.* **47**, 471–472 (2017).
8. Minami, Y. *et al.* The increase of female breast cancer incidence in Japan: Emergence of birth cohort effect. *Int. J. Cancer* **108**, 901–906 (2004).
9. Katanoda, K. *et al.* An updated report on the trends in cancer incidence and mortality in Japan, 1958-2013. *Jpn. J. Clin. Oncol.* **45**, 390–401 (2015).
10. Kim, Y., Yoo, K. Y. & Goodman, M. T. Differences in incidence, mortality and survival of breast cancer by regions and countries in Asia and contributing factors. *Asian Pac. J. Cancer Prev.* **16**, 2857–2870 (2015).
11. Tang, Y., Wang, Y., Kiani, M. F. & Wang, B. Classification, Treatment Strategy, and Associated Drug Resistance in Breast Cancer. *Clin. Breast Cancer* **16**, 335–343 (2016).
12. Eroles, P., Bosch, A., Alejandro Pérez-Fidalgo, J. & Lluch, A. Molecular biology in breast cancer: Intrinsic subtypes and signaling pathways. *Cancer Treat. Rev.* **38**, 698–707 (2012).
13. Howlader, N., Cronin, K. A., Kurian, A. W. & Andridge, R. Differences in breast cancer survival by molecular subtypes in the United States. *Cancer Epidemiol. Biomarkers Prev.* **27**, 619–626 (2018).
14. Fallahpour, S., Navaneelan, T., De, P. & Borgo, A. Breast cancer survival by molecular subtype: a population-based analysis of cancer registry data. *CMAJ Open* **5**, E734–E739 (2017).
15. Waks, A. G. & Winer, E. P. Breast Cancer Treatment: A Review. *JAMA - J. Am. Med. Assoc.* **321**, 288–300 (2019).
16. Jacquet, E. *et al.* Endocrine therapy or chemotherapy as first-line therapy in hormone receptor–positive HER2-negative metastatic breast cancer patients. *Eur. J. Cancer* **95**, 93–101 (2018).

17. Osborne, C. K. Tamoxifen in the Treatment of Breast Cancer. *N. Engl. J. Med.* **339**, 1609–1618 (1998).
18. Smith, I. E. & Dowsett, M. Aromatase Inhibitors in Breast Cancer. *N. Engl. J. Med.* **348**, 2431–2442 (2003).
19. Rubin, I. & Yarden, Y. The basic biology of HER2. *Ann. Oncol.* **12**, S3–S8 (2001).
20. Harries, M. & Smith, I. The development and clinical use of trastuzumab (Herceptin). *Endocr. Relat. Cancer* **9**, 75–85 (2002).
21. Nahta, R. & Esteva, F. J. Herceptin: Mechanisms of action and resistance. *Cancer Lett.* **232**, 123–138 (2006).
22. Xuhong, J.-C., Qi, X.-W., Zhang, Y. & Jiang, J. Mechanism, safety and efficacy of three tyrosine kinase inhibitors lapatinib, neratinib and pyrotinib in HER2-positive breast cancer. *Am. J. Cancer Res.* **9**, 2103–2119 (2019).
23. Modi, S. *et al.* Trastuzumab Deruxtecan in Previously Treated HER2-Positive Breast Cancer. *N. Engl. J. Med.* **382**, 610–621 (2020).
24. Lambert, J. M. & Chari, R. V. J. Ado-trastuzumab emtansine (T-DM1): An antibody-drug conjugate (ADC) for HER2-positive breast cancer. *J. Med. Chem.* **57**, 6949–6964 (2014).
25. Presti, D. & Quaquarini, E. The PI3K/AKT/mTOR and CDK4/6 Pathways in Endocrine Resistant HR+/HER2− Metastatic Breast Cancer: Biological Mechanisms and New Treatments Daniele. *Cancers (Basel).* **11**, 1242 (2019).
26. Drooger, J. C., Van Der Padt, A., Sleijfer, S. & Jager, A. Denosumab in breast cancer treatment. *Eur. J. Pharmacol.* **717**, 12–19 (2013).
27. Moody, S. E. *et al.* The transcriptional repressor Snail promotes mammary tumor recurrence. *Cancer Cell* **8**, 197–209 (2005).
28. Turashvili, G. & Brogi, E. Tumor heterogeneity in breast cancer. *Front Med (Lausanne)* **4**, 121–132 (2017).
29. Nowell, P. C. The Clonal Evolution of Tumor Cell Populations. *Science (80-.).* **194**, 23–28 (1976).
30. Navin, N. *et al.* Tumour evolution inferred by single-cell sequencing. *Nature* **472**, 90–95 (2011).
31. Li, G. *et al.* Mechanisms of acquired resistance to trastuzumab emtansine in breast cancer cells. *Mol. Cancer Ther.* **17**, 1441–1453 (2018).
32. Fabian, M. R., Sonenberg, N. & Filipowicz, W. Regulation of mRNA Translation and Stability by microRNAs. *Annu. Rev. Biochem.* **79**, 351–379 (2010).
33. Ha, M. & Kim, V. N. Regulation of microRNA biogenesis. *Nat. Rev. Mol. Cell Biol.* **15**, 509–524 (2014).
34. Fabian, M. R. & Sonenberg, N. The mechanics of miRNA-mediated gene silencing: A look under the hood of miRISC. *Nat. Struct. Mol. Biol.* **19**, 586–593 (2012).

35. Bartel, D. P. MicroRNAs: Target Recognition and Regulatory Functions. *Cell* **136**, 215–233 (2009).
36. Wee, L. M., Flores-Jasso, C. F., Salomon, W. E. & Zamore, P. D. Argonaute divides Its RNA guide into domains with distinct functions and RNA-binding properties. *Cell* **151**, 1055–1067 (2012).
37. Plotnikova, O., Baranova, A. & Skoblov, M. Comprehensive Analysis of Human microRNA–mRNA Interactome. *Front. Genet.* **10**, 1–11 (2019).
38. Iwakawa, H. oki & Tomari, Y. The Functions of MicroRNAs: mRNA Decay and Translational Repression. *Trends Cell Biol.* **25**, 651–665 (2015).
39. Stevens, K. When microRNAs activate translation. *Nat. Methods* **5**, 122–123 (2008).
40. Hwang, H. W. & Mendell, J. T. MicroRNAs in cell proliferation, cell death, and tumorigenesis. *Br. J. Cancer* **94**, 776–780 (2006).
41. Bueno, M. J., De Castro, I. P. & Malumbres, M. Control of cell proliferation pathways by microRNAs. *Cell Cycle* **7**, 3143–3148 (2008).
42. Jovanovic, M. & Hengartner, M. O. miRNAs and apoptosis: RNAs to die for. *Oncogene* **25**, 6176–6187 (2006).
43. Gantier, M. P., Sadler, A. J. & Williams, B. R. G. Fine-tuning of the innate immune response by microRNAs. *Immunol. Cell Biol.* **85**, 458–462 (2007).
44. Poy, M. N. *et al.* A pancreatic islet-specific microRNA regulates insulin secretion. *Nature* **432**, 226–230 (2004).
45. Cheng, H. Y. M. *et al.* microRNA Modulation of Circadian-Clock Period and Entrainment. *Neuron* **54**, 813–829 (2007).
46. Mortoglou, M. *et al.* MicroRNA-Regulated Signaling Pathways: Potential Biomarkers for Pancreatic Ductal Adenocarcinoma. *Stresses* **1**, 30–47 (2021).
47. Dwivedi, S., Purohit, P. & Sharma, P. MicroRNAs and Diseases: Promising Biomarkers for Diagnosis and Therapeutics. *Indian J. Clin. Biochem.* **34**, 243–245 (2019).
48. Li, Y. & Kowdley, K. V. MicroRNAs in Common Human Diseases. *Genomics, Proteomics Bioinforma.* **10**, 246–253 (2012).
49. Ardekani, A. M. & Naeini, M. M. The role of microRNAs in human diseases. *Avicenna J. Med. Biotechnol.* **2**, 161–179 (2010).
50. Hwang, H. W. & Mendell, J. T. MicroRNAs in cell proliferation, cell death, and tumorigenesis. *Br. J. Cancer* **94**, 776–780 (2006).
51. Rodrigues, D. V. S. *et al.* MicroRNAs in cell cycle progression and proliferation: molecular mechanisms and pathways. *Non-coding RNA Investig.* **2**, 28–28 (2018).
52. Loh, H. Y. *et al.* The regulatory role of microRNAs in breast cancer. *Int. J. Mol. Sci.* **20**, 4940 (2019).

53. Hemmatzadeh, M., Mohammadi, H., Jadidi-Niaragh, F., Asghari, F. & Yousefi, M. The role of oncomirs in the pathogenesis and treatment of breast cancer. *Biomedicine and Pharmacotherapy* **78**, 129–139 (2016).
54. Wang, Z. X., Lu, B. Bin, Wang, H., Cheng, Z. X. & Yin, Y. M. MicroRNA-21 Modulates Chemosensitivity of Breast Cancer Cells to Doxorubicin by Targeting PTEN. *Arch. Med. Res.* **42**, 281–290 (2011).
55. Wang, H. *et al.* MicroRNA-21 promotes breast cancer proliferation and metastasis by targeting LZTFL1. *BMC Cancer* **19**, (2019).
56. Yan, L. X. *et al.* Knockdown of miR-21 in human breast cancer cell lines inhibits proliferation, in vitro migration and in vivo tumor growth. *Breast Cancer Res.* **13**, R2 (2011).
57. Zhu, S. *et al.* MicroRNA-21 targets tumor suppressor genes in invasion and metastasis. *Cell Res.* **18**, 350–359 (2008).
58. Wang, Y., Liu, Z. & Shen, J. MicroRNA-421-targeted PDCD4 regulates breast cancer cell proliferation. *Int. J. Mol. Med.* **43**, 267–275 (2019).
59. Wang, F., Lv, P., Liu, X., Zhu, M. & Qiu, X. microRNA-214 enhances the invasion ability of breast cancer cells by targeting p53. *Int. J. Mol. Med.* **35**, 1395–1402 (2015).
60. Wang, F., Li, L., Chen, Z., Zhu, M. & Gu, Y. MicroRNA-214 acts as a potential oncogene in breast cancer by targeting the PTEN-PI3K/Akt signaling pathway. *Int. J. Mol. Med.* **37**, 1421–1428 (2016).
61. Zhang, G., Zhong, L., Luo, H. & Wang, S. MicroRNA-155-3p promotes breast cancer progression through down-regulating CADM1. *Onco. Targets. Ther.* **12**, 7993–8002 (2019).
62. Lu, K. *et al.* miRNA-24-3p promotes cell proliferation and inhibits apoptosis in human breast cancer by targeting p27Kip1. *Oncol. Rep.* **34**, 995–1002 (2015).
63. Liu, C., Chen, Z., Fang, M. & Qiao, Y. MicroRNA let-7a inhibits proliferation of breast cancer cell by downregulating USP32 expression. *Transl. Cancer Res.* **8**, 1763–1771 (2019).
64. Wei, Y., Liu, G., Wu, B., Yuan, Y. & Pan, Y. Let-7d inhibits growth and metastasis in breast cancer by targeting Jab1/Cops5. *Cell. Physiol. Biochem.* **47**, 2126–2135 (2018).
65. Liu, K. *et al.* Let-7a inhibits growth and migration of breast cancer cells by targeting HMGA1. *Int. J. Oncol.* **46**, 2526–2534 (2015).
66. Spizzo, R. *et al.* MiR-145 participates with TP53 in a death-promoting regulatory loop and targets estrogen receptor-α in human breast cancer cells. *Cell Death Differ.* **17**, 246–254 (2010).
67. Bajan, S. & Hutvagner, G. RNA-Based Therapeutics: From Antisense Oligonucleotides to miRNAs. *Cells* **9**, 137 (2020).
68. Titze-de-Almeida, R., David, C. & Titze-de-Almeida, S. S. The Race of 10 Synthetic RNAi-Based Drugs to the Pharmaceutical Market. *Pharm. Res.* **34**, 1339–1363 (2017).
69. Ramanujam, D. *et al.* MicroRNA-21–Dependent Macrophage-to-Fibroblast Signaling Determines

the Cardiac Response to Pressure Overload. *Circulation* **143**, 1513–1525 (2021).

70. Lima, J. F., Cerqueira, L., Figueiredo, C., Oliveira, C. & Azevedo, N. F. Anti-miRNA oligonucleotides: A comprehensive guide for design. *RNA Biol.* **15**, 338–352 (2018).
71. Lennox, K. A. & Behlke, M. A. Chemical modification and design of anti-miRNA oligonucleotides. *Gene Ther.* **18**, 1111–1120 (2011).
72. Elayadi, A. N., Braasch, D. A. & Corey, D. R. Implications of high-affinity hybridization by locked nucleic acid oligomers for inhibition of human telomerase. *Biochemistry* **41**, 9973–9981 (2002).
73. Langkjær, N., Pasternak, A. & Wengel, J. UNA (unlocked nucleic acid): A flexible RNA mimic that allows engineering of nucleic acid duplex stability. *Bioorganic Med. Chem.* **17**, 5420–5425 (2009).
74. Sheehan, D. *et al.* Biochemical properties of phosphonoacetate and thiophosphonoacetate oligodeoxyribonucleotides. *Nucleic Acids Res.* **31**, 4109–4118 (2003).
75. Summerton, J. & Weller, D. Morpholino Antisense Oligomers: Design, Preparation, and Properties. *Antisense Nucleic Acid Drug Dev.* **7**, 187–195 (1997).
76. Nielsen, P. E., Egholm, M., Berg, R. H. & Buchardt, O. Sequence-selective recognition of DNA by strand displacement with a thymine-substituted polyamide. *Science (80-.).* **254**, 1497–1500 (1991).
77. Vermeulen, A. *et al.* Double-stranded regions are essential design components of potent inhibitors of RISC function. *RNA* **13**, 723–730 (2007).
78. Haraguchi, T. *et al.* A potent 2′-O-methylated RNA-based microRNA inhibitor with unique secondary structures. *Nucleic Acids Res.* **40**, e58 (2012).
79. Ichikawa, K. *et al.* Interstrand cross-link of DNA by covalently linking a pair of abasic sites. *Chem. Commun.* **48**, 2143–2145 (2012).
80. Hirano, Y., Ikegami, M., Kowata, K. & Komatsu, Y. Bienzyme reactions on cross-linked DNA scaffolds for electrochemical analysis. *Bioelectrochemistry* **113**, 15–19 (2017).
81. Mie, Y. *et al.* Function Control of Anti-microRNA Oligonucleotides Using Interstrand Cross-Linked Duplexes. *Mol. Ther. - Nucleic Acids* **10**, 64–74 (2018).
82. Osaki, M., Takeshita, F. & Ochiya, T. MicroRNAs as biomarkers and therapeutic drugs in human cancer. *Biomarkers* **13**, 658–670 (2008).
83. Krichevsky, A. M. & Gabriely, G. miR-21: A small multi-faceted RNA. *J. Cell. Mol. Med.* **13**, 39–53 (2009).
84. Meier, J. *et al.* Genome-wide identification of translationally inhibited and degraded miR-155 targets using RNA-interacting protein-IP. *RNA Biol.* **10**, 1017–1029 (2013).
85. Zhang, H. *et al.* MiR-148a promotes apoptosis by targeting Bcl-2 in colorectal cancer. *Cell Death Differ.* **18**, 1702–1710 (2011).

86. Yu, B. *et al.* miR-148a functions as a tumor suppressor by targeting CCK-BR via inactivating STAT3 and Akt in human gastric cancer. *PLoS One* **11**, e0158961 (2016).
87. Xu, X. *et al.* Hepatitis B virus X protein represses miRNA-148a to enhance tumorigenesis. *J. Clin. Invest.* **123**, 630–645 (2013).
88. Li, F., Liu, W., Song, Z. & Chang, D. miR-148a overexpression inhibits cell proliferation and induces cell apoptosis by suppressing the Wnt/β-catenin signal pathway in breast cancer MCF-7 cells. *Int. J. Clin. Exp. Pathol.* **9**, 3349–3356 (2016).
89. Jiang, Q. *et al.* MicroRNA-148a inhibits breast cancer migration and invasion by directly targeting WNT-1. *Oncol. Rep.* **35**, 1425–1432 (2016).
90. Xue, J., Chen, Z., Gu, X., Zhang, Y. & Zhang, W. MicroRNA-148a inhibits migration of breast cancer cells by targeting MMP-13. *Tumor Biol.* **37**, 1581–1590 (2016).
91. Xu, X. *et al.* MiR-148a functions to suppress metastasis and serves as a prognostic indicator in triple-negative breast cancer. *Oncotarget* **7**, 20381–20394 (2016).
92. Zhang, L., Xing, M., Wang, X., Cao, W. & Wang, H. MiR-148a suppresses invasion and induces apoptosis of breast cancer cells by regulating USP4 and BIM expression. *Int. J. Clin. Exp. Pathol.* **10**, 8361–8368 (2017).
93. Chen, Y., Song, Y.-X. & Wang, Z.-N. The MicroRNA-148 / 152 Family : Multi-faceted Players MicroRNA biogenesis. *Mol. Cancer* **12**, (2013).
94. Cuk, K. *et al.* Circulating microRNAs in plasma as early detection markers for breast cancer. *Int. J. Cancer* **132**, 1602–1612 (2013).
95. Cimino, D. *et al.* miR148b is a major coordinator of breast cancer progression in a relapse-associated microRNA signature by targeting ITGA5, ROCK1, PIK3CA, NRAS, and CSF1. *FASEB J.* **27**, 1223–1235 (2013).
96. Luo, H. & Liang, C. MicroRNA-148b inhibits proliferation and the epithelial-mesenchymal transition and increases radiosensitivity in non-small cell lung carcinomas by regulating ROCK1. *Exp. Ther. Med.* **15**, 3609–3616 (2018).
97. Jiang, Z., Zhang, J. W., Chen, F. H. & Sun, Y. MiR-148b suppressed non-small cell lung cancer progression via inhibiting ALCAM through the NF-κB signaling pathway. *Thorac. Cancer* **11**, 415–425 (2020).
98. Shen, J. *et al.* Circulating miR-148b and miR-133a as biomarkers for breast cancer detection. *Oncotarget* **5**, 5284–5294 (2014).
99. Dai, W. *et al.* miR-148b-3p, miR-190b, and miR-429 regulate cell progression and act as potential biomarkers for breast cancer. *J. Breast Cancer* **22**, 219–236 (2019).
100. Lennox, K. A., Owczarzy, R., Thomas, D. M., Walder, J. A. & Behlke, M. A. Improved performance of anti-miRNA oligonucleotides using a novel non-nucleotide modifier. *Mol. Ther. - Nucleic Acids* **2**, e117 (2013).

101. Dai, X., Cheng, H., Bai, Z. & Li, J. Breast cancer cell line classification and Its relevance with breast tumor subtyping. *J. Cancer* **8**, 3131–3141 (2017).
102. Xu, J. *et al.* Gene 33 inhibits apoptosis of breast cancer cells and increases poly(ADP-ribose) polymerase expression. *Breast Cancer Res. Treat.* **91**, 207–215 (2005).
103. Chen, C. Y., Chen, J., He, L. & Stiles, B. L. PTEN: Tumor suppressor and metabolic regulator. *Front. Endocrinol. (Lausanne).* **9**, (2018).
104. Wu, Y. *et al.* MicroRNA-21 (Mir-21) Promotes Cell Growth and Invasion by Repressing Tumor Suppressor PTEN in Colorectal Cancer. *Cell. Physiol. Biochem.* **43**, 945–958 (2017).
105. Cui, M. *et al.* Over-expression of miR-21 and lower PTEN levels in wilms' tumor with aggressive behavior. *Tohoku J. Exp. Med.* **242**, 43–52 (2017).
106. Yang, Y., Guo, J. X. & Shao, Z. Q. miR-21 targets and inhibits tumor suppressor gene PTEN to promote prostate cancer cell proliferation and invasion: An experimental study. *Asian Pac. J. Trop. Med.* **10**, 87–91 (2017).
107. Zhang, J. guang *et al.* MicroRNA-21 (miR-21) represses tumor suppressor PTEN and promotes growth and invasion in non-small cell lung cancer (NSCLC). *Clin. Chim. Acta* **411**, 846–852 (2010).
108. Davis, S. *et al.* Potent inhibition of microRNA in vivo without degradation. *Nucleic Acids Res.* **37**, 70–77 (2009).
109. Thomson, D. W., Bracken, C. P., Szubert, J. M. & Goodall, G. J. On Measuring miRNAs after Transient Transfection of Mimics or Antisense Inhibitors. *PLoS One* **8**, e55214 (2013).
110. Cadenas, C. *et al.* Role of thioredoxin reductase 1 and thioredoxin interacting protein in prognosis of breast cancer. *Breast Cancer Res.* **12**, R44 (2010).
111. Park, J. W., Lee, S. H., Woo, G. H., Kwon, H. J. & Kim, D. Y. Downregulation of TXNIP leads to high proliferative activity and estrogen-dependent cell growth in breast cancer. *Biochem. Biophys. Res. Commun.* **498**, 566–572 (2018).
112. Heo, M. J. *et al.* Alcohol dysregulates miR-148a in hepatocytes through FoxO1, facilitating pyroptosis via TXNIP overexpression. *Gut* **68**, 708–720 (2019).
113. Dai, Y. *et al.* M2 macrophage-derived exosomes carry microRNA-148a to alleviate myocardial ischemia/reperfusion injury via inhibiting TXNIP and the TLR4/NF-κB/NLRP3 inflammasome signaling pathway. *J. Mol. Cell. Cardiol.* **142**, 65–79 (2020).
114. Hayes, J., Peruzzi, P. P. & Lawler, S. MicroRNAs in cancer: Biomarkers, functions and therapy. *Trends Mol. Med.* **20**, 460–469 (2014).
115. Matsuzaki, J. & Ochiya, T. Circulating microRNAs: Next-generation Cancer Detection. *Keio J. Med.* **69**, 88–96 (2020).
116. Zhang, C. *et al.* MiR-21: A gene of dual regulation in breast cancer. *Int. J. Oncol.* **48**, 161–172 (2016).

117. Si, M. L. *et al.* miR-21-mediated tumor growth. *Oncogene* **26**, 2799–2803 (2007).
118. Fix, L. N., Shah, M., Efferth, T., Farwell, M. A. & Zhang, B. MicroRNA expression profile of MCF-7 human breast cancer cells and the effect of green tea polyphenon-60. *Cancer Genomics Proteomics* **7**, 261–278 (2010).
119. Chen, K. S. & DeLuca, H. F. Isolation and characterization of a novel cDNA from HL-60 cells treated with 1,25-dihydroxyvitamin D-3. *Biochim. Biophys. Acta, Gene Struct. Expr.* **1219**, 26–32 (1994).
120. Patwari, P., Higgins, L. J., Chutkow, W. A., Yoshioka, J. & Lee, R. T. The interaction of thioredoxin with Txnip: Evidence for formation of a mixed disulfide by disulfide exchange. *J. Biol. Chem.* **281**, 21884–21891 (2006).
121. Zhang, J., Li, X., Han, X., Liu, R. & Fang, J. Targeting the Thioredoxin System for Cancer Therapy. *Trends Pharmacol. Sci.* **38**, 794–808 (2017).
122. Jia, J. J., Geng, W. S., Wang, Z. Q., Chen, L. & Zeng, X. S. The role of thioredoxin system in cancer: strategy for cancer therapy. *Cancer Chemother. Pharmacol.* **84**, 453–470 (2019).
123. Cha, M. K., Suh, K. H. & Kim, I. H. Overexpression of peroxiredoxin i and thioredoxin1 in human breast carcinoma. *J. Exp. Clin. Cancer Res.* **28**, 93 (2009).
124. Bhatia, M. *et al.* The thioredoxin system in breast cancer cell invasion and migration. *Redox Biol.* **8**, 68–78 (2016).
125. Gallegos, A. *et al.* Transfection with human thioredoxin increases cell proliferation and a dominant-negative mutant thioredoxin reverses the transformed phenotype of human breast cancer cells. *Cancer Res.* **56**, 5765–5770 (1996).
126. Lu, J., Chew, E. H. & Holmgren, A. Targeting thioredoxin reductase is a basis for cancer therapy by arsenic trioxide. *Proc. Natl. Acad. Sci. USA* **104**, 12288–12293 (2007).
127. Turturro, F., Friday, E. & Welbourne, T. Hyperglycemia regulates thioredoxin-ROS activity through induction of thioredoxin-interacting protein (TXNIP) in metastatic breast cancer-derived cells MDA-MB-231. *BMC Cancer* **7**, (2007).
128. Clerk, A. *et al.* Signaling Pathways Mediating Cardiac Myocyte Gene Expression in Physiological and Stress Responses. *J. Cell. Physiol.* **212**, 311–322 (2007).
129. Pang, J. K. S., Phua, Q. H. & Soh, B. S. Applications of miRNAs in cardiac development, disease progression and regeneration. *Stem Cell Res. Ther.* **10**, 336 (2019).
130. Colpaert, R. M. W. & Calore, M. MicroRNAs in Cardiac Diseases. *Cells* **8**, 737 (2019).
131. Tao, L. *et al.* Crucial role of miR-433 in regulating cardiac fibrosis. *Theranostics* **6**, 2068–2083 (2016).
132. Li, Q. *et al.* Overexpression of microRNA-99a attenuates heart remodelling and improves cardiac performance after myocardial infarction. *J. Cell. Mol. Med.* **18**, 919–928 (2014).
133. La Rochelle, P., Lexchin, J. & Simonyan, D. Analysis of the Drugs Withdrawn from the US

Market from 1976 to 2010 for Safety Reasons. *Pharmaceut. Med.* **30**, 277–289 (2016).

134. Onakpoya, I. J., Heneghan, C. J. & Aronson, J. K. Post-marketing withdrawal of 462 medicinal products because of adverse drug reactions: A systematic review of the world literature. *BMC Med.* **14**, (2016).
135. Siramshetty, V. B. *et al.* WITHDRAWN - A resource for withdrawn and discontinued drugs. *Nucleic Acids Res.* **44**, D1080–D1086 (2016).
136. Navarrete, E. G. *et al.* Screening drug-induced arrhythmia events using human induced pluripotent stem cell-derived cardiomyocytes and low-impedance microelectrode arrays. *Circulation* **128**, 3–13 (2013).
137. Qu, Y. & Vargas, H. M. Proarrhythmia risk assessment in human induced pluripotent stem cell-derived cardiomyocytes using the Maestro MEA platform. *Toxicol. Sci.* **147**, 286–295 (2015).
138. Lu, F. H. *et al.* Calcium-sensing receptors regulate cardiomyocyte Ca2+ signaling via the sarcoplasmic reticulum-mitochondrion interface during hypoxia/reoxygenation. *J. Biomed. Sci.* **17**, 50 (2010).
139. Dittami, G. M., Rajguru, S. M., Lasher, R. A., Hitchcock, R. W. & Rabbitt, R. D. Intracellular calcium transients evoked by pulsed infrared radiation in neonatal cardiomyocytes. *J. Physiol.* **589**, 1295–1306 (2011).
140. Wang, Z. *et al.* Pulse splitter-based nonlinear microscopy for live-cardiomyocyte imaging. *Multiphot. Microsc. Biomed. Sci. XIV* **8948**, 89482X (2014).
141. Liu, J., Sun, N., Bruce, M. A., Wu, J. C. & Butte, M. J. Atomic force mechanobiology of pluripotent stem cell-derived cardiomyocytes. *PLoS One* **7**, e37559 (2012).
142. Peters, M. F., Lamore, S. D., Guo, L., Scott, C. W. & Kolaja, K. L. Human Stem Cell-Derived Cardiomyocytes in Cellular Impedance Assays: Bringing Cardiotoxicity Screening to the Front Line. *Cardiovasc. Toxicol.* **15**, 127–139 (2015).
143. Hossain, M. M. *et al.* Non-invasive characterization of mouse embryonic stem cell derived cardiomyocytes based on the intensity variation in digital beating video. *Analyst* **135**, 1624–1630 (2010).
144. Ahola, A. *et al.* Video image-based analysis of single human induced pluripotent stem cell derived cardiomyocyte beating dynamics using digital image correlation. *Biomed. Eng. Online* **13**, (2014).
145. Hayakawa, T. *et al.* Image-based evaluation of contraction-relaxation kinetics of human-induced pluripotent stem cell-derived cardiomyocytes: Correlation and complementarity with extracellular electrophysiology. *J. Mol. Cell. Cardiol.* **77**, 178–191 (2014).
146. Maddah, M. *et al.* A non-invasive platform for functional characterization of stem-cell-derived cardiomyocytes with applications in cardiotoxicity testing. *Stem Cell Reports* **4**, 621–631 (2015).
147. Bard, A. J., Fan, F. R. F., Kwak, J. & Lev, O. Scanning Electrochemical Microscopy.

Introduction and Principles. *Anal. Chem.* **61**, 132–138 (1989).

148. Zhao, C., Sinha, J. K., Wijayawardhana, C. A. & Wittstock, G. Monitoring β-galactosidase activity by means of scanning electrochemical microscopy. *J. Electroanal. Chem.* **561**, 83–91 (2004).
149. Hirano, Y. *et al.* Improvement of detectable sensitivity for enzyme reaction by scanning electrochemical microscopy with distance control system for immunosensing. *Electrochemistry* **80**, 30–32 (2012).
150. Liu, B., Rotenberg, S. A. & Mirkin, M. V. Scanning electrochemical microscopy of living cells: Different redox activities of nonmetastatic and metastatic human breast cells. *Proc. Natl. Acad. Sci. USA* **97**, 9855–9860 (2000).
151. Zhang, M. M. N., Long, Y. T. & Ding, Z. Cisplatin effects on evolution of reactive oxygen species from single human bladder cancer cells investigated by scanning electrochemical microscopy. *J. Inorg. Biochem.* **108**, 115–122 (2012).
152. Nebel, M., Grützke, S., Diab, N., Schulte, A. & Schuhmann, W. Microelectrochemical visualization of oxygen consumption of single living cells. *Faraday Discuss.* **164**, 19–32 (2013).
153. Koley, D. & Bard, A. J. Triton X-100 concentration effects on membrane permeability of a single HeLa cell by scanning electrochemical microscopy (SECM). *Proc. Natl. Acad. Sci. USA* **107**, 16783–16787 (2010).
154. Matsumae, Y. *et al.* Evaluation of the differentiation status of single embryonic stem cells using scanning electrochemical microscopy. *Chem. Commun.* **49**, 6498–6500 (2013).
155. Hirano, Y., Kodama, M., Shibuya, M., Maki, Y. & Komatsu, Y. Analysis of beat fluctuations and oxygen consumption in cardiomyocytes by scanning electrochemical microscopy. *Anal. Biochem.* **447**, 39–42 (2014).
156. Hirano, Y. *et al.* Construction of time-lapse scanning electrochemical microscopy with temperature control and its application to evaluate the preservation effects of antifreeze proteins on living cells. *Anal. Chem.* **80**, 9349–9354 (2008).
157. Zhang, M. M. N., Long, Y. T. & Ding, Z. Filming a live cell by scanning electrochemical microscopy: Label-free imaging of the dynamic morphology in real time. *Chem. Cent. J.* **6**, 20 (2012).
158. Takahashi, Y. *et al.* Topographical and electrochemical nanoscale imaging of living cells using voltage-switching mode scanning electrochemical microscopy. *Proc. Natl. Acad. Sci. USA* **109**, 11540–11545 (2012).
159. Ummadi, J. G., Joshi, V. S., Gupta, P. R., Indra, A. K. & Koley, D. Single-cell migration as studied by scanning electrochemical microscopy. *Anal. Methods* **7**, 8826–8831 (2015).
160. Van Der Velden, J. *et al.* Effects of calcium, inorganic phosphate, and pH on isometric force in single skinned cardiomyocytes from donor and failing human hearts. *Circulation* **104**, 1140–1146

(2001).

161. Fu, Y. *et al.* Temperature dependence and thermodynamic properties of Ca2+ sparks in rat cardiomyocytes. *Biophys. J.* **89**, 2533–2541 (2005).

162. Liu, H. Myofibrillogenesis in live neonatal cardiomyocytes observed with hybrid two-photon excitation fluorescence-second harmonic generation microscopy. *J. Biomed. Opt.* **16**, 126012 (2011).

163. Liu, H. *et al.* Myosin filament assembly onto myofibrils in live neonatal cardiomyocytes observed by TPEF-SHG microscopy. *Cardiovasc. Res.* **97**, 262–270 (2013).

164. De Arcangelis, V., Liu, S., Zhang, D., Soto, D. & Xiang, Y. K. Equilibrium between adenylyl cyclase and phosphodiesterase patterns adrenergic agonist dose-dependent spatiotemporal cAMP/protein kinase a activities in cardiomyocytes. *Mol. Pharmacol.* **78**, 340–349 (2010).

165. Hirano, Y., Kowata, K., Kodama, M. & Komatsu, Y. Development of a scanning electrochemical microscopy-based micropipette and its application to analysis of topographic change of single-cell. *Bioelectrochemistry* **92**, 1–5 (2013).

166. Koley, D. & Bard, A. J. Inhibition of the MRP1-mediated transport of the menadione-glutathione conjugate (thiodione) in HeLa cells as studied by SECM. *Proc. Natl. Acad. Sci. USA* **109**, 11522–11527 (2012).

167. Salamifar, S. E. & Lai, R. Y. Use of combined scanning electrochemical and fluorescence microscopy for detection of reactive oxygen species in prostate cancer cells. *Anal. Chem.* **85**, 9417–9421 (2013).

168. Nattel, S. & Carlsson, L. Innovative approaches to anti-arrhythmic drug therapy. *Nat. Rev. Drug Discov.* **5**, 1034–1049 (2006).

169. Tsukamoto, S. *et al.* Simultaneous imaging of local calcium and single sarcomere length in rat neonatal cardiomyocytes using yellow Cameleon-Nano140. *J. Gen. Physiol.* **148**, 341–355 (2016).

170. Danziger, R. S. *et al.* Extracellular ATP has a potent effect to enhance cystolic calcium and contractility in single ventricular myocytes. *Cell Calcium* **9**, 193–199 (1988).

171. Scamps, F. & Vassort, G. Mechanism of extracellular ATP-induced depolarization in rat isolated ventricular cardiomyocytes. *Pflügers Arch. Eur. J. Physiol.* **417**, 309–316 (1990).

172. Cedergren, B. & Harary, I. In Vitro studies on single beating rat heart cells. VII. Ultrastructure of the beating cell layer. *J. Ultrasructure Res.* **11**, 443–454 (1964).

173. Mark, G. E. & Strasser, F. F. Pacemaker activity and mitosis in cultures of newborn rat heart ventricle cells. *Exp. Cell Res.* **44**, 217–233 (1966).

174. Deglincerti, A. *et al.* Self-organization of human embryonic stem cells on micropatterns. *Nat. Protoc.* **11**, 2223–2232 (2016).

175. Yap, Y. G. & Camm, A. J. Drug induced QT prolongation and torsades de pointes. *Heart* **89**,

1363–1372 (2003).

176. Zhou, Z., Vorperian, V. R., Gong, Q., Zhang, S. & January, C. T. Block of HERG potassium channels by the antihistamine astemizole and its metabolites desmethylastemizole and norastemizole. *J. Cardiovasc. Electrophysiol.* **10**, 836–843 (1999).

177. Nachimuthu, S., Assar, M. D. & Schussler, J. M. Drug-induced QT interval prolongation: Mechanisms and clinical management. *Ther. Adv. Drug Saf.* **3**, 241–253 (2012).

178. Kuo, I. Y. & Ehrlich, B. E. Signaling in muscle contraction. *Cold Spring Harb. Perspect. Biol.* **7**, 1–14 (2015).

Acknowledgements

First, I would like to express my sincere gratitude to Professor Yasuo Komatsu for inviting me, working adult, to his laboratory and for giving me guidance and encouragement in carrying out this doctoral research. His guidance that I should work on research without compromise and strive for others to understand my achievements will be of great use in my future research and work.

I would like to express my sincere gratitude to Associate Professor Yu Hirano for his careful guidance and advice in advancing this doctoral research. This doctoral study could not be accomplished without daily discussions with him and his advice. The discussion with him made my student life meaningful.

I would like to express my deep gratitude to Dr. Yasuhiro Mie, Dr. Yoshiyuki Nishimiya, Dr. Mashiki Ikegami, and Dr. Akiyoshi Nakamura for their daily useful advice. I would also like to express my deep gratitude to Ms. Sachiko Chidaka and Ms. Keiko Kowata for their technical support.

I would also like to thank everyone in Laboratory of Biomolecular Adaptation Science for their help in my student life in the laboratory.

I would also like to express my sincere gratitude to late Mr. Yoshiyuki Maki, who gave me the opportunity to learn at Hokkaido University and everyone at Cosmo Bio for their great cooperation and helpful discussions to balance my work and student life.

Finally, I would like to express my special thanks to my family for understanding my student life and always supporting me.

Sho Okumura

September 2021